universität wien

DISSERTATION / DOCTORAL THESIS

Titel der Dissertation / Title of the Doctoral Thesis

„Microstructure and Magnetic Response of Colloidal Magnetic Platelets“

verfasst von / submitted by

Margaret Rosenberg MSc

angestrebter akademischer Grad / in partial fulfillment of the requirements for the degree of

Doktor der Naturwissenschaften (Dr. rer. Nat.)

Wien, 2023 / Vienna, 2023

Studienkennzahl lt. Studienblatt / degree programme code as it appears on the student record sheet:	A 796 605 411
Dissertationsgebiet lt. Studienblatt / field of study as it appears on the student record sheet:	Physik
Betreut von / Supervisor:	Univ.-Prof. Dr. Sofia S. Kantorovich, Privatdoz

Abstract

The field of Soft Matter is driven by the self-reinforcing diversity of both the substances under its purview, and the desired applications thereof. The subfield of Magnetic Soft Matter, for instance, has grown from simple colloidal suspensions of spherical magnetic iron oxide micron-scale particles to incorporate varying materials, sizes, shapes and carrier media. This progress was spurred on by compelling theoretical predictions, experimental advancements in synthesis, and new ideas for applications in biomedicine and industrial devices. However, certain canonical constraints were, until very recently, maintained - such as that ferrofluids, despite their name, are merely para- or superparamagnetic. To break this barrier, theoretical models indicated that incorporating ideas from another subfield, that of Liquid Crystals, would be necessary. By combining the asymmetry of particle shape and the anisotropy of magnetic interactions, a new regime of tunable suspension behavior would be unlocked.

This conjecture was recently validated in experiment, by the use of discotic magnetic nanoparticles with an out-of-plane dipole moment to create a spontaneous room temperature stable macroscopic ferromagnetic phase. While this property alone would be cause for interest, it has already been shown for other anisometric or anisotropic particles that the self-assembly, magnetic response, thermodynamic and phase behavior of suspensions can be tuned by altering the particle shape.

To understand the underlying mechanisms behind these observations and to guide future experimental developments, we use Molecular Dynamics simulations to explore the microscopic properties and ensuing macroscopic behavior of such suspensions. Whenever possible, we collaborate closely with experimental groups to ensure applicability. In cases where the outcome defies explanation using standard approaches, we use analytical theory to further understand the effects at play. Starting from a detailed, experiment-based model, we clarify the role of magnetic platelet polydispersity in the isotropic phase, and its contribution to the suspension's increased response to low magnetic fields. We then show that even in simplified systems of low anisometry, monodisperse, magnetic nanoplatelets, the shape drastically alters the microstructure, in particular the self-assembly, of the particles. This microstructure, in turn, elicits an altered static magnetic susceptibility, which we describe using a combination of new and adapted theory. To fully characterize the field response, we explain the mechanisms behind an experimentally observed gap in the peaks of the dynamic magnetic susceptibility, and show the response to an additional bias field. Inspired by similar experimental studies, we also investigate the demixing behavior of binary platelet mixtures and the effects of anisometric depletants. To facilitate future studies, we conclude the project by briefly exploring more advanced options in the dipolar, electrostatic, and domain-related modelling choices.

In summary, this thesis presents the effects of the combined ansiotropy and anisometry of colloidal magnetic nanoplatelet suspensions on the overall magnetic fluid properties, primarily through the lens of self-assembly and magnetic response. This fundamental understanding of the system opens up new perspectives in the use of shape anisotropy as a key parameter to tailor properties of Magnetic Soft Matter.

Zusammenfassung

Das Fachgebiet der magnetischen weichen Materie wird sowohl durch die selbst-verstärkende Vielfalt an Substanzen, als auch durch die Vielzahl an gewünschten Anwendungsbereichen vorangetrieben. Das Teilgebiet der magnetischen weichen Materie, zum Beispiel, ist von einfachen kolloidalen Suspensionen von sphärischen, magnetischen Eisenoxid-Teilchen in der Größenordnung von Mikrometeren bis hin zum Beinhalten von mannigfaltigen Materialien, Größen, Formen und Trägermedien herangewachsen. Dieser Fortschritt wurde sowohl durch anregende theoretische Vorhersagen, experimentelle Fortschritte in der Synthese, und neue Ideen für Anwendungen in der Biomedizin und industriellen Maschinen gefördert. Dennoch wurden gewisse kanonische Einschränkungen bis vor Kurzem eingehalten- beispielsweise, dass Ferrofluide trotz ihres Namens nicht ferromagnetisch, sondern para- oder superparamagnetisch sind. Aus theoretischen Modellen ging hervor, dass um diese Schranke zu durchbrechen, Ideen aus einem anderen Teilgebiet der weichen Materie, den Flüssigkristallen, notwendig seien. Durch die Kombination der Asymmetrie der Teilchenform und der Anisotropie der magnetischen Interaktionen könnte so ein neuer Bereich der regelbaren kolloidalen Suspensionseigenschaften erschlossen werden.

Diese Hypothese wurde neulich experimentell bestätigt, durch die Verwendung von diskotischen magnetischen Nanoteilchen mit einem im rechten Winkel zur Oberfläche orientiertem Dipolmoment, womit eine spontane, bei Zimmertemperatur stabile makroskopische ferromagnetische Phase entstand. Abgesehen davon, dass diese Eigenschaft an sich bereits Interesse erweckt, wurde bereits für andere anisometrische oder anisotropische Teilchen nachgewiesen, dass die Selbstorganization, die magnetische Feldreaktion, und das thermodynamische und Phasenverhalten der kolloidalen Suspension durch Änderung der Teilchenform angepasst werden kann.

Um die zugrundeliegenden Mechanismen hinter diesen Beobachtungen zu Verstehen, und um zukünftige experimentelle Entwicklungen zu lenken, verwenden wir Molekulardynamik Simulationen, um die mikroskopischen Eigenschaften und das daraus entstehende makroskopische Verhalten solcher Suspensionen zu Beschreiben. Wo möglich, arbeiteten wir mit experimentellen Forschungsgruppen zusammen, um die Anwendbarkeit zu sichern. In den Fällen wo die Ergebnisse sich nicht durch die üblichen Ansätze erklären ließen, nutzten wir analytische Theorie, um die Effekte besser zu verstehen. Begonnen mit einem detaillieren, auf dem Experiment basierten Modell, klären wir die Rolle der Polydispersität der magnetischen Plättchen in der isotropischen Phase und erläutern ihren Beitrag zu der verstärkten Reaktion der Suspension auf schwache Magnetfelder. Darauf zeigen wir, dass sogar in vereinfachten Systemen von wenig anisometrischen, monodispersen magnetischen Nanoteilchen die Form die Mikrostruktur, vor allem die Selbstorganization der Teilchen, stark beeinflusst. Diese Mikrostruktur führt dann zu einer Veränderung der statischen magnetischen Susceptibilität, welche wir sowohl durch neue als auch durch Modifikationen bestehender Theorie beschreiben. Um die Reaktion auf das magnetische Feld vollständig zu Beschreiben, erklären wir den Mechanismus hinter der experimentell beobachteten Abstand in den Maxima der

dynamischen magnetischen Susceptibilität, und zeigen die Reaktion auf ein zusätzliches Biasfeld. Inspiriert von ähnlichen experimentellen Studien, untersuchen wir auch das "demixing" Verhalten von binären magnetischen Plättchen-Mischungen und die Effekte von anisometrischen neutralen Teilchen (depletants). Um zukünftige Forschung zu erleichtern, beenden wir das Projekt durch eine kurze Untersuchung von fortgeschrittenen Optionen in den dipolaren, elektrostatischen und Domänen ähnlichen Modellierungsoptionen.

Zusammenfassend präsentiert diese Dissertation die Effekte von kombinierter Anisotropie und Anisometrie von kolloidalen magnetischen Nanoplättchen- Suspensionen auf die Eigenschaften des magnetischen Fluides, vor allem aus der Perspektive von Selbstorganization und magnetischer Feldreaktion. Dieses fundamentale Verständnis von dem System eröffnet neue Perspektiven auf die Nutzung von Form-Anisotropy als Schlüsselparameter um die Eigenschaften magnetischer weicher Materie anzupassen.

Acknowledgements

Despite the hermit-like experience of the lone programmer in a dark room during a global pandemic that I was initially promised, this thesis endeavor owes a lot to the people who have accompanied me throughout the years. To avoid an overly saccharine reading experience, I have decided to follow the one true passion discovered in this writing process - outlines - and order the thanks on a scale from science to social silliness to sentiment; caveat lector.

Firstly I would like to thank my supervisor, Sofia, for her support and mentorship. I'd also like to thank the Dipolar Soft Matter Group - to steal a phrase from another alumnus - past and present, as well as the broader Computational and Soft Matter Physics group at the University of Vienna. A lot of these results are inspired by the the experimental work taking place at Josef Stephan Institute, the University of Magdeburg and the Technical University of Braunschweig: I'd like to thank the people behind that work for their insights, helpful scientific discussions and encouragement. One of the highlights of this journey has been my secondment at the University of Edinburgh, which merits this accolade due to the efforts and impressive patience of Philip Camp. I would also like to thank the ESPResSo Gods, in particular Rudolf Weeber, for answering all my simulation-related questions over the years.

On a less serious note, I appreciate the years of camaraderie in Vienna, especially the long discussions of ghost theory and various alternate universes. Thanks to both the Camp group and the larger Phys Chem Chem Phys group for making me feel at home in Edinburgh. It goes without saying that the PhD is an intense experience: thanks to my friends for keeping me sane throughout this process, and thanks to my family for supporting me. I'm not really sure I believe in thesis dedications, but if that were the case, I'd dedicate this to my grandmother, Dr. Stefanie Rosenberg.

Contents

1 - Introduction

1.1 Introduction

Describing the field of Soft Matter in a comprehensive, yet precise way is challenging due to the broad range of topics it spans. The difficulty of phrasing this explanation also depends strongly on the desired target audience: schoolchildren, with their intuitive grasp of the tactile joys of "squishy" matter and inherent motivation for the study of ice cream, are perhaps the most easily addressed demographic. At the level of undergraduates, Soft Matter can be presented as an exciting motivation to explore methods from fields such as thermodynamics. But veering outside of these groups, Soft Matter is an extensive, interdisciplinary field that seems limited only by the creativity (and funding agencies) of the researchers working in it. The term "Soft Matter" (matière molle) was coined by the French physicist Madeleine Veyssié, who meant it as a humorous catch-all for the study of materials which can exhibit a strong response to external stimuli[1,2]. The more broadly used contemporary definition, originating from the perspective of Soft Matter as a study of complex fluids, defines the field as the study of physical systems which are more structured than simple fluids, yet less structured than crystalline solids[3].

Soft Matter is further characterized by its key length and energy scales. The processes of interest take place at the nano- or microscale, where the energy scale is such that Brownian motion and thermal fluctuations play an important role. This does not mean that Soft Matter methods and results cannot be applied more broadly. For instance, research into liquid crystalline defects in the nematic phase is also used in cosmology[4]. As alluded to previously, Soft Matter often combines aspects of Physics, Chemistry and Biology. It is difficult to imagine Soft Matter without the study of polymers[5], or to understand the current interest in liquid-liquid phase transitions without insight into the biological systems to which they seem crucial[6,7]. Some examples of Soft Matter are colloidal suspensions, liquid crystals, polymer solutions, or indeed the cells and tissues that comprise most living matter[8]. The flexibility of this definition means that a wide range of materials with an even wider range of applications can be studied with approaches developed for Soft Matter research.

In addition to the more abstract research directions mentioned, Soft Matter underlies many materials in daily use[9]. Food is a complex Soft Matter system[10–12], as well as medical, beauty and hygiene products such as creams and gels. Certain natural phenomena, such as clouds, or industrial products, such as foams, fall under the umbrella of Soft Matter as well, both being colloidal systems. At this point, it may seem impractical to group these disparate materials together. Nevertheless, they are united by their responsiveness to external stimuli and their capacity to self-organize their internal structure. It is this self-assembly that is considered by some to be a defining feature of Soft Matter[3]. Moreover, combined with the structure and energy scales, these traits mean Soft Matter systems are promising for the development of new materials with tailored responses and tuneable properties.

To illustrate these concepts, we will focus on two specific subfields of Soft Matter. Firstly, colloidal suspensions, which encompass most of the systems described above and are often cited as archetypal representations of Soft Matter. Colloidal suspensions are physical systems consisting of two disparate phases; the carrier medium and suspended colloidal particles, of which at least one dimension needs to be in the microscopic regime[13]. Colloidal dispersions of a solid phase in a liquid phase, such as the titular platelet suspensions discussed in this thesis, are referred to as colloidal sols. A key characteristic of colloidal suspensions is their stability, which can be difficult to ensure in synthesis. As the dispersed particles can self-assemble for entropic reasons alone[14], additional stabilization via electrostatic or steric repulsion is often necessary. Nevertheless, some degree of aggregation can be desirable, as the resulting material might have more useful properties. For instance, hierarchical or bottom-up assembly is a popular approach to create intricate nanostructures[15,16].

A second, equally ubiquitous example of Soft Matter are Liquid Crystals. To paraphrase De Gennes' introduction[17], liquid crystals are materials that exhibit phases with mechanical and symmetry properties which lie between those of liquid and crystals. One simple example would be a nematic phase, where the components of the liquid crystal have one-dimensional orientational order, but do not have any positional order. While liquid crystals have been spotted in nature, creating the iridescent shimmer of blue Morpho butterfly wings[18] and jewel beetle exoskeletons[19], they were introduced to the scientific community by the Austrian botanist Friedrich Reinitzer and German chemist Otto Lehmann in the late 19th century[20]. In modern contexts, liquid crystals are most known for their optical-electric response properties, which enabled the development of the liquid crystal display (LCD). They are also well-suited to photonic[21] and biomedical[22] applications. For the context of this introduction, it's important to note that the prototypical liquid crystal does not consist of separate phases: the ordered components can simply be the constituent molecules of the substance. Although colloidal liquid crystals exist, this term is most commonly understood as referring to colloidal particles suspended in an anisotropic fluid matrix, with colloidal suspensions of anisotropic particles in an isotropic phase being referred to as molecular liquid crystals[23].

Armed with these broad examples, we can now delve into the field at the core of this thesis, Magnetic Soft Matter. The prototypical examples of Magnetic Soft Matter are ferrofluids, a term which originally referred to colloidal suspensions of nanoscale or microscale spherical single-domain magnetic nanoparticles suspended in a carrier fluid[24]. One such fluid is shown in Figure 1.1. The spikes at the center of the fluid are caused by the response of the fluid to a magnet placed underneath the dish. This effect is called the Rosensweig instability, which arises from the competition of the ferrofluid surface tension with the alignment with the field of the dispersed particles. While ferrofluids were conceptualized as part of a NASA project to manipulate rocket fuel at zero gravity[25], their applications have since expanded to a range of industrial and medical pursuits[26]. Despite the name ferrofluid, which comes from the Latin word for iron, conventional

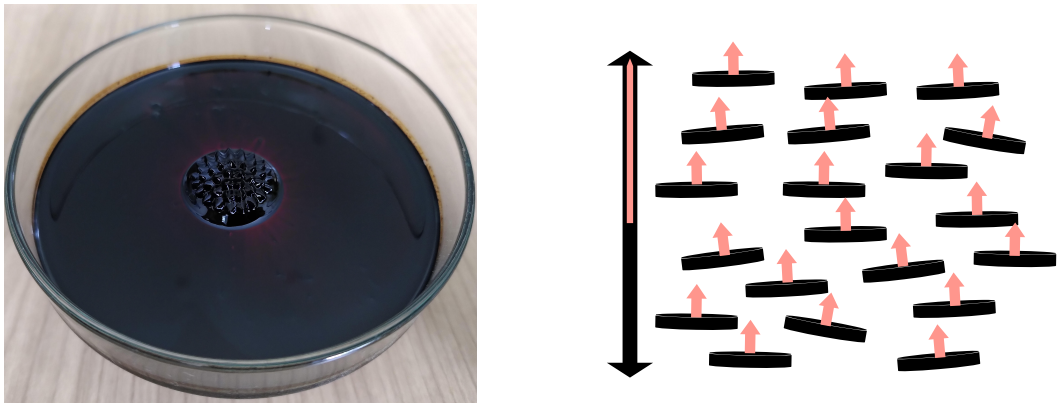

Figure 1.1: Left: A ferrofluid (black) in a petri-dish, with a bar magnet placed below the center. We can observe the spikes of the Rosensweig instability at the center of the fluid. Right: A sketch of the interior of a ferromagnetic ferrofluid candidate, based de Gennes' hypothesis. The platelet particles are shown in black, their magnetic moments are depicted as pink arrows and the corresponding nematic director (black) and oriented nematic director (pink) are depicted on the left side of the image.

ferrofluids are superparamagnetic. In other words, although the individual colloidal particles are ferromagnetic, there is no overall zero-field magnetization of the suspension. From a microstructural perspective, this means that although some colloidal self-assembly can take place, there is no long-range orientational ordering of the particles.

Recent advances in colloidal particle synthesis have made it possible to create colloids with a wide variety of anisotropic shapes[27,28]. Although colloidal anisotropy occurs naturally, these advances allow for more control over the properties of the suspension - not just in the case of liquid crystalline phase formation, as noted previously, but also in contexts such as colloidal self-assembly[29]. In addition to shape anisotropy, a similar option would be anisometric or patchy particles, which have anisotropic interactions[30]. Both of these alterations are of particular interest in Magnetic Soft Matter, as it has been shown that the shape of magnetic anisometric particles influences self-assembly scenarios, magnetic response, thermodynamic, magnetorheological and phase behavior[26]. This means that the use of particle shape as a control parameter could allow us to create a wide variety of colloids with customizable properties. While positing asymmetric or anisotropic colloids as inherently novel is misleading, research using the deliberate combination of colloidal shape asymmetry with anisotropy of interactions is still in its infancy.

One opportunity provided by these new experimental developments is to tackle an old, simmering debate: why are there no ferromagnetic ferrofluids? More precisely, classic Magnetic Soft Matter does not form spontaneously magnetically ordered phases[31–44], despite there being no obvious physical interdict thereof. However, a conjecture by Brochard and deGennes states that a suspension of particles which exhibit a spontaneous nematic ordered phase with a dipole moment oriented along the nematic director, could form a macroscopic ferromagnetic phase[45]. In 2016, a team of experimentalists led by Alenka Mertelj found spontaneous ferromagnetic nematic ordering

in a system of platelet-shaped anisometric magnetic nanoplatelets[46]. Despite continued study since, only certain properties of the system are accessible in experiment, and these measurements are highly sensitive. Moreover, to the extent that its magnetic properties are known, these differ markedly from classical ferrofluids. The phase behavior also only partially matches the well-studied examples of colloidal platelets.

How can such systems be studied? Soft Matter and Complex Fluids as a whole rest upon results from Statistical Physics and Thermodynamics, which provide a mathematical framework for many such research questions[47,48]. Be that as it may, having a theory is not equivalent to having an analytically solveable theory, in particular since colloidal sols present - almost by definition - many-body problems. For liquids, this is where approximate models such as the electrostatic descriptions of DLVO theory[13] come into play. These models provide some description of material properties, but in cases where theory and experiment diverge, it is unclear if the theory is inaccurate or the approximations of system properties are insufficient. Using a computer simulation gives us a result that is exact to statistical accuracy for the given model[49]. While an output may just consist of numbers, its interpretation can replace infeasible experiments, and can yield new discoveries, such as the role of repulsive interactions in hard-sphere crystallization[48]. The access to otherwise inaccessible properties, validation of modelling and the potential for discovery are why computational approaches is so prevalent in colloidal Soft Matter physics, as they can precisely describe the microstructure that gives rise to the macrostructure observed in experiment.

The objective of this thesis was to conduct the first simulation study on the properties of a system which combined Magnetic Soft Matter and Liquid Crystals in search of a ferromagnetic nematic phase. It combines direct collaboration with experimental groups to match physical results, with "blue-skies" computational studies on the abstracted system. Overall, this thesis outlines the first footsteps on the path to a new category of magnetic soft, liquid crystalline materials.

1.2 Thesis Outline

This thesis draws from a combination of peer-reviewed papers, papers in preparation and unpublished results. It is structured as follows:

Theory and Techniques lays out the groundwork for the project, contextualises it within current Soft Matter research and briefly presents an overview of some of the results obtained by experimental partners, to understand the impetus behind certain directions of investigation.

Polydispersity in the Isotropic Phase presents results obtained using a straightforward modelling approach to provide proof of concept in matching the experimental system. It explores the effects of polydispersity, its influence on the microstructure and a field-induced istropic to nematic transition at low density.

Microstructure and Static Magnetic Properties is a more theoretical work on the shape effects of the dipolar magnetic nanoplatelets with varying aspect ratios on the self-assembly within the suspension and the static magnetic magnetic susceptibility of the suspension.

Dynamic Susceptibility is a study of the dynamic magnetic susceptibility of low aspect ratio platelet suspensions with varying microstructure, which posits an explanation of the origin of the split-peak effect seen in experiment.

Binary Mixes of Magnetic Spheroids explores systems where different proportions of depletants or less-magnetic particles are combined with magnetic platelets. These results are contrasted with similar mixtures of dipolar ellipsoids, showing the relationship between shape, magnetic interactions and demixing.

Phase and Particles consists of multiple shorter subsections, which may be of interest to the reader but did not reach the extent for standalone publication. It contains results on the electrostatic modelling of platelets, a suggested characterization bridging magnetic and liquid crystalline domains, and a proposed distributed dipole model.

This work is then concluded by a combined “Conclusion and Outlook”, Chapter 8. The publications and manuscripts resulting from this thesis are:

1. Rosenberg M., Gregorin Ž., Hribar Boštjančič P., Sebastián N., Lisjak D., Kantorovich S. S. and Sánchez P. A., *“The influence of polydispersity on the structural properties of the isotropic phase of magnetic nanoplatelets*", Journal of Molecular Liquids (2020), **312**, 113293,

2. Rosenberg M., S. Kantorovich, "*The influence of anisotropy on the microstructure and magnetic properties of dipolar nanoplatelet suspensions*", Physical Chemistry Chemical Physics (2023), **25**, 4, 2781-2792

3. H. Nadasi, M. Küster, A. Mertelj, N. Sebastián, P. Hribar Boštjančič, D. Lisjak, T. Viereck, M. Rosenberg, A. O. Ivanov, S. Kantorovich, A. Eremin, F. Ludwig, "*Role of ionic surfactant in magnetic dynamics of self-assembled dispersions of nanoplatelets*", Journal of Molecular Liquids (2023), **382**, 121900-,

4. Rosenberg M., S. Kantorovich, P. J. Camp "*Structure and dynamics in suspensions of magnetic platelets*", in preparation

5. Rosenberg M., E. Pyanzina, E. Novak, S. Kantorovich "*Binary Mixtures of Magnetic Spheroids*", in preparation

These works are explicitly listed at the start of the chapters which contain them.

2 - Theory and Techniques

2.1 Theoretical Framework

While this work is computational, it rests on the theoretical underpinnings of Statistical Mechanics and Thermodynamics. This means that some terminology and ideas from these fields are necessary for two key points. Firstly, to argue that the simulations performed capture meaningful physics, and secondly, to be able to derive statements about the macroscopic behavior of the system from simulations. This overview is not intended to be comprehensive, only to touch on some topics that will become relevant in this work. Detailed explanations and derivations can be found in the literature cited throughout this section, especially Refs[3,47,48].

2.1.1 Basic Concepts

The systems investigated in this work are "classical" fluids, liquids which we presume can be fully described by classical statistical mechanics[47]. This means that the microscopic states of our systems are fully described by specifying the positions $\mathbf{x}$ and momenta $\mathbf{p}$ of the particles centers of mass, and the Hamiltonian of our system can be written as the sum of the potential and kinetic energies, depending on those two respective properties. The interactions between our simulation particles will constitute the potential energy term $U(\mathbf{x})$ of the Hamiltonian. The kinetic energy is given by the standard term from classical mechanics. In combination, we have:

$$H(\mathbf{x},\mathbf{p}) = \sum_{i=1}^{N} \frac{\mathbf{p}^2}{2m} + U(\mathbf{x}) \tag{2.1}$$

for a system of N particles of mass m. While the practicality of obtaining dynamics from this equation will be dealt with in Section 2.2.1, some underlying questions remain. Firstly, based on the inherent quantum physics and thermal fluctuations present in reality, the equations of motion we will derive from (2.1) will not be deterministic. This means that the goal of our computations in not solving them per se: instead, we seek to generate valid configurations (microstates) and track their evolution in time. Key to this is the concept of thermodynamic equilibrium, which is the state of minimum free energy. Systems in this equilibrium state are effectively time-independent, which facilitates averaging over different configurations. At thermodynamic equilibrium, we also obtain a well-defined thermodynamic temperature $\beta = 1/k_B T$ to serve as the energy scale.

Another important concept from thermodynamics is the concept of ensembles. The thermodynamic state of a system is given by a set of three fixed thermodynamic variables. Common choices for simulations are the grand canonical ensemble μPT, where μ is the chemical potential, P is the pressure and T is the thermodynamic temperature, or the canonical ensemble NVT, where N is

the number of particles and V is the volume. In thermodynamic equilibrium, the remaining thermodynamic variables will fluctuate around their ensemble average. In this work, the ensemble of choice is NVT, which is well-suited to both Molecular Dynamics simulations and easily compared with experimental results. All ensembles agree in the thermodynamic limit of infinite system size, avoiding the neighborhood of phase transitions.

Thus far, we have only discussed averages over different microstates (ensemble averages). These make sense from a theoretical perspective, but both experimentally and in Molecular Dynamics simulations, properties are measured over a finite time evolution. It is plausible that these two procedures should be equivalent in the limit. Systems with this property are ergodic; this is called the ergodicity hypothesis. Additionally, an ergodic system at equilibrium is time-independent. For this to be true, the system propagated in time needs to visit enough of the phase space, which also implies chosing reasonable starting values, as otherwise technically ergodic systems can become stuck in a region of phase space.

One important result from statistical physics that will be used implicitly is the fluctuation-dissipation theorem[47]. While more detailed derivations are beyond the scope of this introduction, it links the thermal fluctuations in the system with the dissipation by establishing the relationship of the Fourier transform of a time-dependent autocorrelation of an observable and its generic susceptibility. This will be crucial for generating appropriate thermal fluctations, and is also used in deriving the results we will obtain from linear response theory (see Section 2.1.1.a).

Some systems and their properties are already interesting at the microscopic level, and can be directly compared to experimental measurements such as SANS (small-angle neutron scattering)[50]. Beyond this, the global properties of the system (macrostates) can be more straightforward to observe in experiment and are often of interest for practical applications. The link between microstates and macrostates is given by the thermodynamic partition function. The partition function owes its name to its partitioning of the probabilities of the different microstates, which in turn determines the macrostate. Therefore calculating the partition function will give information on the overall state of the system. One option to express the partition function is via the configurational integral. In the canonical ensemble, the partition function (up to normalization) is given by

$$Z_{NVT} \sim \int d\mathbf{p} dV \exp(-\beta \mathbf{H}(\mathbf{p}, \mathbf{x})) \tag{2.2}$$

Aside from the link mentioned above, partition functions can also be used in other theoretical results that connect microstructure with macroscopic results, such as the chain-corrected model of magnetic susceptibility of a ferrofluid[51].

2.1.1.a Time Correlations and Linear Response Theory

One particular genre of observable in computer simulations bears its own mention here: time-dependent correlation functions. These are defined as

$$C(t - t_0) = \langle A(t), B(t_0) \rangle \tag{2.3}$$

where the angular brackets denote ensemble averages over the dynamical variables A and B. At equilibrium, this distribution is invariant under time translation, so we can set $t_0 = 0$. Correlation functions are interesting simulation observables since their power spectra can be measured experimentally via spectroscopy (for certain choices of A, B)[47].

This can be combined with linear response theory, which links the response of a system to a weak perturbation to the time-correlation functions of a system at equilibrium. Onsager originally put forth the idea that the system's response to a weak peturbation would be the same as the decay of a spontaneous fluctuation[48]. This equivalence could then be used to calculate static or dynamic properties of the system based on measuring time correlation functions. For instance, the initial static magnetic susceptibility of a ferrofluid can be calculated based on the magnetic autocorrelation function. Taking the Fourier transform of this autocorrelation function then yields the dynamic susceptibility spectra, which can be measured experimentally. The fluctuation dissipation theorem allows us to link these spectra to the energy dissipation into the ferrofluid, which is relevant for magnetic hyperthermia[52].

2.1.2 Liquid Crystals

Liquid Crystals are ordered states of condensed matter systems. This means states that are more structured than an isotropic liquid, yet less ordered than a crystalline solid. Systems which exhibit liquid crystal phases are commonly referred to as mesogens. There are a wide variety of different phases characterized by varying degrees of orientational and (typically partial) positional order[53], which are driven by factors including temperature, concentration, particle anistropy, and chemical properties of the mesogens. Liquid crystalline phases are common in systems consisting of anisotropic particles, either at a molecular level or a collodial sol, but can also occur in various polymer systems.

The simplest liquid crystalline phase is the nematic phase, in which particles have orientational but no positional ordering. This orientational order is characterized by the alignment of the particles' axis with the nematic axis n. This alignment is invariant under change of sign. Other phases include smectic and columnar, which have orientational and one-dimension or two-dimensional positional order, respectively. The latter is often referred to as the discotic phase in the literature, since it is found in very dense suspensions of disc-shaped particles.

Since the study of liquid crystals is a vast field, I will focus on the subcategory of oblate spheroidal mesogens at constant temperature. An example of a phase diagram of a disk-like mesogen where the phase behavior depends on the concentration is shown in Figure 13 of Ref[54]. For platelets with a very pronounced aspect ratio (low thickness L to diameter D), the suspension is isotropic (*i.e.* disordered) at low concentrations. As the density increases, there is a phase transition into a state where the mesogens have long-range orientational ordering, but no positional ordering (nematic phase). As the density is increased even further, we see a phase with orientational ordering and partial positional ordering - specifically, the platelets have "stacked" into columns (columnar phase). Beyond the phase diagram mentioned here, suspensions of purely repulsive platelet-shaped particles have been studied in detail and shown to have, depending on the aspect ratio, isotropic, nematic, lamellar or columnar phases[54–56]. Such systems have also been studied in experiment, using charged platelet-shaped colloidal nanoparticles[57–63]. From the perspective of this thesis, the key finding is that nematic ordering can appear in suspensions of non-magnetic nanoplatelets above a threshold concentration, and that this threshold is strongly dependent on the shape anisotropy of the particles and the strength of the electrostatic interactions[56,57,61].

To characterize the degree of orientational order in a system, the order parameter

$$S = \frac{1}{2}\langle 3\cos^2\theta - 1\rangle \tag{2.4}$$

where θ represents the angle between the main director of the particles and the nematic director of the system, is commonly used. The main director lies along the main axis of the particle, while the nematic director is defined based on the overall system. Pursuing the evolution of S with increasing concentration (or density, or temperature) can serve to track the phase transition. For instance, a first-order isotropic to nematic phase transition would be signaled by a discontinuous change in S (see Ref.[3]). However, this does not mean that the order parameter would suddenly jump from 0 to 1. Instead, the liquid crystal will initially form small ordered regions, so-called tactoids, before the system reaches a longer-scale ordering. This behavior can be investigated via the pairwise order parameter, where θ is defined as the angle between particle directors at a certain distance.

While liquid crystals do display long-range ordering, this does not mean the entire fluid shares the same alignment. Liquid crystals form domains of sizes depending on system composition and underlying energy: inside a domain, the particles are all aligned, while their boundary illustrates a continuous intermediate order. Although magnetic materials also exhibit domains, these exhibit very specific rotations of the magnetization depending on the domain wall type. Liquid crystals are also very sensitive to their boundary conditions (physical or simulation) which can promote local ordering. In practice, the nematic director is not typically a straight line as drawn: if it changes discontinuously in some point or region, these deviations are called topological defects, or more specifically disinclinations. This terminology is mentioned due to its relevance in Chapter 7: a full

discussion of liquid crystal theory goes beyond the scope of this thesis.

2.1.2.a Ferromagnetic nematics

On a conceptual level, ferromagnetic nematic fluids were first proposed in 1970 by Brochard and de Gennes[45]. Their original concept was to suspend elongated magnetic nanoparticles in a liquid crystalline carrier medium. By the coupling of the elongated particles to the suspension, the particles would be oriented along a nematic axis, and the magnetic alignment would be induced by the magnetic interactions between the particles. In experiment, this initially did not work as intended: the system either remains nematic and paramagnetic, or, if the magnetic interactions are increased, the particles irreversibly aggregate. Insidiously, as the isotropic to nematic phase transition alters the elastic interactions between particles, suspensions which are strongly magnetic and stable in the isotropic phase can become destabilized by the transition and aggregate[64].

However, these experimental issues do not mean that the concept is fundamentally unsound. One alternative is to change the particle geometry, which changes the elastic liquid crystalline interaction, in hope of obtaining a stable suspension. The first particle shape to achieve this in experiment was initially synthesized in 2009[65,66]: barium hexaferrite (BaHF) nanoplatelets. Switching from elongated particles to platelets has the advantage that even if the particles assemble, they form stacks that contribute to the overall magnetization instead of cancelling out.

Although these may be ferromagnetic nematics, they are arguably not ferrofluids, as the carrier fluid is not isotropic. The first ferromagnetic ferrofluid was achieved in 2016[46], as a joint effort between the groups at the University of Colorado and Josef Stefan Institute. This was done by suspending using a more dense suspension of the aforementioned BaHF platelets in an isotropic solvent (n-butanol). These are stabilized electrostatically via a surfactant coating of dodecylbenzenesulfonic acid (DBSA). As opposed to the situation discussed in previous paragraphs, these platelets form a nematic phase due to the same mechanisms as anisotropic colloids. This is the system that lies at the core of this thesis.

2.1.3 Colloidal Sols

As presented in the introduction, this thesis concerns a specific type of colloidal suspension: solid particles suspended in a fluid phase, also known as colloidal sols. From a theoretical perspective, the microscale behavior of colloidal sols is governed by effective theories such as the ideal gas law or Debye-Hueckel theory of charged colloids[13]. These seek to mitigate the issue of many-body problems posed by the dispersed phase particles. A primary concern with these suspensions is their stability. A certain degree of aggregation (self-assembly) can be desirable, as it alters the overall properties of the fluid and, if controllable, can create a tunening parameter. However, too much aggregation can cause the colloidal particles to sediment. This means that the energy scale of

effects taking place near the thermal energy is a double-edged sword: one may be able to obtain strong effects, but one must also ensure that the colloids remain sufficiently dispersed.

How can colloidal stability be ensured? Two common methods for stabilizing ferrofluids are either sterically or electrostatically repulsive surface coatings. This choice depends on both the particles and carrier medium: in a polar solvent, like-charged surfaces can be sufficiently repulsive for stabilization, while otherwise repulsive polymer-based interaction may be necessary.

Some stabilization is crucial in colloidal sols due to the ever-present Van der Waals attraction. This so-called force is a summation of several forces, including the London dispersion force, which lead to strong attraction at very short ranges. For coarse-grained models, one common simplification is to assume that the colloidal stabilization will suffice to effectively cancel out the Van der Waals attraction.

Another effect that favors aggregation is the depletion interaction. This takes place when the suspension contains additional particles, such as non-absorbed polymers from previous stabilization attempts. This can be understood by taking an entropic perspective, as the aggregation can then increase the number of possible configurations, although an equally valid derivation in terms of osmotic pressure can be found in Ref[3]. This means that additional particles can lead to either increased self-assembly, or a phase separation.

Even in a model omitting the forces above, the colloidal particles should be in constant motion due to Brownian motion. Fortunately, Brownian-motion is well understood: its inclusion will be discussed in Section 2.2. The remainder of this section will discuss the more intricate cases: specifically, magnetic and electrostatic interactions which are relevant for the stability and phase behavior.

2.1.3.a Charged Platelets: A case study

In the liquid crystalline section, we stated that charged platelets were used to verify the simulation results described in works such as Ref[54]. In experiment, an ideal, purely steric hard platelet is not fully realistic and would typically require some stabilization against Van der Waals attraction. The distinction between the short-ranged steric repulsion and long-range electrostatic repulsion of colloids is partially in the eye of the theorist. In experiment, the effective particle shape can be altered by surfactant ions that are attracted to, and possibly condense onto, a repulsive coating. More specifically, a charged colloidal particle in a polar solvent will attract counterions, which screen the electrostatic interactions. These will in turn attract co-ions, and the result is called the electrostatic double layer. This is well-described by so-called Derjaguin-Landau-Verwey-Overbeek (DLVO) theory, which describes the counterion distributions near surfaces and the resulting field gradient[13]. From a modelling perspective, we have two options: we can either adapt the particle shape to include this region of effective exclusion, or include some form of explicit or mean-field

electrostatics.

The effective platelet size approach dates back to Onsager[67] and has been effective for relating the phase behavior of Gibbsite platelet suspensions[58,60] to the hard disc phase diagram mentioned above. However, this isotropic to nematic to columnar phase behavior is not solely determined by the shape. If we expand to other materials, such as clays, the particles can form arrested states and otherwise depart from expectations. From such experiments, it became increasingly obvious that the charge stabilization of the particles, and resulting interparticle interactions, are key to these differences. Additionally, there have since been theoretical calculations of the potential of a highly-charged platelet which suggest that the anistropy remains a strong influence at all scales[68]. An extensive Monte-Carlo study by Jabbari-Farouji[62] et al. found that in the phase diagram of Laponite-inspired platelets, depending on the screening, the density-dependent phase behavior varied from an isotropic to random stacks to nematic stacks to columnar phase transition, to the limit of a direct isotropic to BCC plastic crystal to BCC crystal. In brief, the presence of strong anisotropic electrostatic interactions affected the phase diagram in ways that for strong screening promoted stack formation, and for low screening promoted ordering, but not nematic ordering.

To be clear, it is not that we expect the DBSA coating of BaHF magnetic nanoplatelets to induce these same effects. Based on experimentalist results, they should be far more similar to steric platelets. However, these findings do indicate that the standard assumption of all electrostatics been effectively radially symmetric in the limit is perhaps too optimistic, and that a long-ranged anisotropic electrostatic contribution to the platelet interactions should not be ruled out completely.

2.1.4 Magnetic Soft Matter

The subfield of magnetic soft matter is fairly young, with the first experimental synthesis of ferrofluids taking place in the 1960s. A conventional ferrofluid is a colloidal suspension of single-domain, uniformly magnetized spherical ferromagnetic nanoparticles in a non-magnetic carrier liquid[24]. This makes the resulting suspension (super-)paramagnetic[26], as the name ferro- derives from the commonly used iron microparticles contained within. The particles in question typically have weak magnetic interactions, and are stabilized sterically or electrostatically. While ferrofluids were initially proposed with a very specific application in mind - controlling liquid rocket fuel in outer space for NASA missions - they are now used in many different settings. For example, magnetically responsive liquids are extensively used in magnetic dampers[69,70] and seals[71]; they are also appealing for biomedical applications[72], the development of new applications in vibratory energy harvesting[73–76], magneto-mechanical actuation and pumping in micro-magnetofluidics[77,78], magnetic control of light[79,80], targeted drug delivery[80,81] or magnetic field sensing and visualisation[82].

Returning to our specific modeling perspective, we can consider how to represent the magnetic interparticle interactions. Based on nanoscale particles made of materials where the domain size

is typically nanoscale, we assume the particle is single-domain and represent its magnetic moment with a single dipole moment. In principle, this dipole moment could relax through internal rotation (Néel relaxation) and rotation of the particle (Brownian relaxation). We assume cases where only the latter is relevant, eschewing Néel fluctuations and assuming a fixed magnetic axis.

A particular avenue of study has been the search for a ferromagnetic phase. In ferrofluids with spherical particles, this topic was intensely pursued from the 1980s to early 2000s[31–44]. The conclusion of these investigations is that a macroscopic ferromagnetic ordering is not observed under standard conditions, despite the strong anisotropy of the interparticle dipolar interactions. A plausible interpretation of theses findings is that the alignment of the nanoparticle dipole moments (*i.e.* the orientational ordering) necessary for a macroscopic zero-field magnetization of a fluid is too entropically unfavorable to come about without some additional effect to drive the ordering.

2.1.4.a Magnetic response

Applying an external magnetic field to a ferrofluid will lead the particles' magnetic moments $\vec{\mu}$ to align with the field. This property is quantified as the magnetization $\mathbf{M} = \sum_{i=0}^{N} \vec{\mu}_i$, the absolute value of which grows with the field until all the particles are aligned. This is called the saturation magnetization. In an ideal monodisperse superparamagnetic gas, where the particles are all merely interacting with the field and subject to thermal fluctuations, this magnetization obeys the Langevin law[83,84]:

$$M_L(H) = M_s L\left(\frac{\mu H}{k_B T}\right) = M_s L(\alpha) \tag{2.5}$$

where $L(\alpha)$ is the Langevin function:

$$L(\alpha) = \coth(\alpha) - \frac{1}{\alpha}. \tag{2.6}$$

The term $\alpha = \frac{\mu H}{k_B T}$ represents the ratio of magnetic interaction strength to thermal energy, and is typically referred to as the Langevin parameter. In case the system is polydisperse, Eq. 2.5 can be generalised by weighting the integral average with the particle size distribution[85]. However, in both cases, magnetic interparticle correlations have pronounced effects on the magnetic susceptibility. A well-validated model to take them into account for both mono- and poly-disperse moderately concentrated and non-cluster-forming magnetic systems results from second-order modified mean-field theory (MMFT2)[86]. In the framework of MMFT2, the magnetization of the system is obtained by replacing H in Eq. 2.5 by an effective field $H_e(H)$:

$$H_e(H) = H + \frac{4\pi}{3} M_L(H) + \frac{(4\pi)^2}{144} M_L(H) \frac{dM_L(H)}{dH}. \tag{2.7}$$

as derived for spherical particles in Ref[86]. The extent to which a suspension can be magnetized by an infinitely small field is known as the initial (static) magnetic susceptibility:

$$\chi = \left.\frac{\delta M}{\delta H}\right|_{H=0} \tag{2.8}$$

For the idealized Langevin scenario, it can be shown that for spherical particles, $\chi_L = 8\lambda\phi_s$ where λ is the magnetic coupling constant and ϕ_s is the magnetic sphere volume fraction. For discotic particles, the Langevin magnetization reads $\chi_L^p = 8\lambda\phi_p \cdot \left(\frac{2}{3}\left(\frac{h}{d}\right)^2\right)$, where h is the platelet height, d is the platelet diameter and ϕ_p is the platelet volume fraction. Using linear response theory[47], it can be shown that

$$\chi = \frac{4\pi\phi}{3Nk_BT}\left(\langle|\mathbf{M}|^2\rangle - |\langle\mathbf{M}\rangle|^2\right) \tag{2.9}$$

This result is of particular interest since it allows us to calculate a dynamic property simply from static fluctuations. It can be experimentally confirmed, especially for dilute suspensions of weakly magnetic particles, usually close to the Langevin scenario. However, as belabored by previous sections, most interesting systems will contain some form of colloidal interactions, in this case magnetic ones. If the dipolar particles are interacting, their orientations will correlate with those of their neighbors. This prompted Weis to propose the molecular field model[87], which would include the effects for interactions. While this idea was conceptually sound, it predicted a ferromagnetic phase transition for dipolar hard spheres which was never found in experiment. Based on empirical modifications that were found to fit experiment, Ivanov et al. later developed modified mean field theory[86], which was further generalized to account for particle polydispersity[85] (as mentioned above). However, polydispersity is not the only suspension property that could affect the response. If magnetic self-assembly takes place, this effectively creates an oddly-shaped particle aggregate which might have either a stronger magnetic moment for chains, or not contribute for flux-closed rings. The chain idea was explored by Mendelev and Ivanov[51], who introduced a modifying term based on density functional theory to determine the bonding probability. In this approach, the susceptibility can be obtained as:

$$\chi_c = \chi_M\left(\frac{1+p_0K}{1-p_0K}\right) \tag{2.10}$$

where p_0 is the partition function and K denotes the correlation coefficient between two particles in a dimer, which is found to be dependent on the λ. (Here χ_M can be chosen as modified mean-field theory of the first or second order). This partition function p_0 represents the probability of two spherical particles to form a dimer, and so depends on ϕ_s and λ. This probability can be determined by the minimization of the free energy. This approach has been further refined to work for cube-shaped magnetic particles[88], as the partition function is dependent on the particle shape.

2.1.4.b Combining Anisotropy and Anisometry of Magnetic Soft Matter

To be able to induce direction-dependent magnetic properties, one early and promising approach has been the use of anisotropic ferromagnetic nanoparticles to alter the interparticle interactions. The experimental availability of anisotropic dipolar nanoparticles resulted in a series of theoretical studies, which examined the presence of different liquid-crystalline phases in such suspensions[89–105]. The majority of these investigations focused on systems of ellipsoids or spherocylinders, modelled with a point-dipole moment aligned along the main axis of the particle. It was shown that these systems could undergo a vapor-liquid phase transition[106], something which has never been proven for dipolar hard-sphere systems. Furthermore, systems with higher order moments were also investigated[102].

Some studies of systems with anisometric particles with a dipole moment oriented perpendicular to the main axis have already been conducted[107–112]. These investigations predominantly focused on understanding the effects that the rotation of the dipole moment out of the particles' plane would have on the phases of the system. Moreover, at the time, the prevalent interest was in electric dipoles due to their relevance for liquid crystalline applications. While electric and magnetic dipoles have many commonalities, it would be excessively optimistic to assume a direct transposition of results, especially considering the difference in solvent interactions. More complex positioning of the dipoles has also been studied[113]. In the mid-2000s, there have also been some experimental investigations of haematite ellipsoids systems, which are known to have magnetic moments aligned along the short axis[114,115] of the particles.

For the specific magnetic platelets, one especially pertinent set of simulations has been performed by Papaioannou et al.[116]. The authors used Monte Carlo simulations of dipolar hard platelets of varying aspect ratios to explore the phase transitions. They found a weakly first-order polar nematic to non-polar nematic and strongly first-order nematic to columnar transition. This model used a distributed dipolar potential: however, the rotations of particles were constrained by the setup. This means that the models' applicability lay primarily in the densely-packed regime, for sufficiently high aspect ratios. This provides an interesting starting point, since while it secures the phase transition and highly dense behavior, the isotropic phase at lower densities is unexplored. Moreover, the effects of external fields, electrostatics, or dynamics could not be ascertained, and while the limitations in dipole orientation made this distribution feasible, it also took their simulations out of the regions of the phase diagram where magnetic soft matter theory is most applicable. These results were also revisited theoretically for by Petrov[117], who described the isotropic to antiferromagnetic nematic to ferromagnetic nematic transitions using mean-field theory.

2.2 Computer Simulation

In order to actually obtain the results in this work, some form of methodology is necessary. The essence of Computational Physics is to construct the simplest model that captures the system of interest, then rephrase it as a set of computationally tractable equations. This section will lay out that process, with a focus on the very specific questions that will be tackled in upcoming chapters.

While the definition of Soft Matter as based on length scales might appear uninspired, it is a helpful lens in terms of focusing our efforts on the level of description of the system. For many questions, especially those tackled by computational chemists, the exact composition of molecules and the detailed atomic interactions are crucial. However, this level of description grows computationally costly when bulk suspensions of nanoparticles are to be considered. Moreover, what such a model gains in precision, it loses in broader applicability. In contrast to such atomistic models, coarse-grained models are built on the assumption that all detail up to a certain length scale can be simplified and condensed into a series of effective or implicit interactions. As the Magnetic Soft Matter systems in this thesis consist of colloidal sols dispersed in a fluid phase, the canonical choice of scale is to treat the solvent implicitly with a continuum approach, with the colloidal particles now becoming simulation "particles". The effectiveness of this approach and the art of its modelling lies in choosing which properties and interactions to include, up to which level of precision.

2.2.1 Molecular Dynamics

Now that we have chosen our simulation particles, we seek to describe the aspects of their behavior that are interesting to us with a set of equations. The key principle of Molecular Dynamics is to draw up equations of motion governing the propagation of particles, then solve them numerically. A basic assumption underlying this is that classical mechanics will suffice to describe the motion of the particles. Given the particle positions $\mathbf{x}(t)$ of the particles with mass m, the momenta are given by $\mathbf{p}(t) = m\dot{\mathbf{x}}(t)$ and Newton's equations of motion read:

$$\mathbf{F}(\mathbf{x}(t)) - \gamma_T \dot{\mathbf{x}}(t) = m \cdot \ddot{\mathbf{x}}(t) \tag{2.11}$$

where we have included the Stokes friction term, with γ_T as the translational friction coefficient. In absence of external forces, the force $\mathbf{F}(\mathbf{x}(t))$ can be calculated exclusively from the sum of simulation potentials, $\mathbf{F}(t) = -\boldsymbol{\nabla} U(t)$, which will be discussed in the following section. To implement these equations in code, it is most convenient to write them as a set of $6N$ ordinary differential equations:

$$\dot{\mathbf{x}}(t) = \frac{\mathbf{p}(t)}{m} \tag{2.12}$$

$$\dot{\mathbf{p}}(t) = m \cdot \ddot{\mathbf{x}}(t) = \mathbf{F}(\mathbf{x}(t)) - \gamma_T \dot{\mathbf{x}}(t) \tag{2.13}$$

The current formulation lacks initial conditions: to start, a set of particle positions and momenta must be assigned. If the energy landscape of the system is sufficiently flat, the lack of appropriate initial conditions can be circumvented by a warm-up phase in which the system is propagated until thermodynamic equilibrium has been reached. This is often done by placing the particles randomly, then either using the gradient steepest-descent method, capping the forces and/or simply propagating the particles until the system is believed in an equilibrium configuration. This is quantified via an observable that depends on the ensemble chosen. Once equilibrium has been reached, the sampling of configurations can begin.

As a key focus of this work has been to collaborate with experimentalists, we chose the canonical (NVT) ensemble, where N particles in a volume V at a temperature T are kept fixed. This volume V refers to the volume of the central simulation box: in order to mimic a larger system, periodic boundary conditions were used[48]. While keeping N and V constant is fairly straightforward, our current scheme offers no possibility to control the temperature. This requires the addition of a thermostat algorithm. To maintain a near-constant thermodynamic temperature, these algorithms use the statistical physics concept of coupling to a heat bath. In practice, this idea can be achieved in several ways. One popular option is to include an additional coordinate representing the coupling to the Lagrangian when deriving the equations of motion, as done in the Nosé and Nosé-Hoover schemes[48]. However, for this work, one issue was the inclusion of the Brownian motion of the particles, which is important to take into consideration for properties such as self-assembly. Moreover, our current paradigm includes an implicit solvent. For these reasons, we chose a Langevin thermostat. The principle of this thermostat is to use stochastic equations of motion which describe a large, massive particle in a bath of small particles (the implicit solvent). This means that in addition to the basic Newtonian equations of motions (2.11), along with the Newtonian frictional force γ_T (γ_R) proportional to the velocity (angular velocity ω(t)) of the particles, we now add a random force $\mathbf{X}_T(t)$ (torque $\mathbf{X}_R(t)$) which represents the collisions of the particles with the surrounding fluid. The resulting Langevin equations of motion are given by:[118]

$$m\,\ddot{\mathbf{x}}(t) = \mathbf{F}(t) - \gamma_T\,\dot{\mathbf{x}}(t) + \mathbf{X}_T(t) \tag{2.14}$$

$$\mathbf{I} \cdot \dot{\boldsymbol{\omega}}(t) = \boldsymbol{\tau}(t) - \gamma_R\,\boldsymbol{\omega}(t) + \mathbf{X}_R(t) \tag{2.15}$$

where $\mathbf{I}$ is the inertia tensor, and $\boldsymbol{\tau}$ the torque. A more detailed explanation of generalized Langevin equations, including constraints on the random forces and torques, can be found in Ref[47].

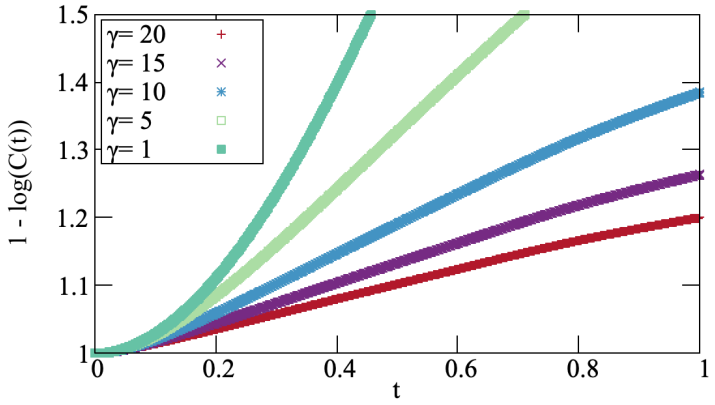

Figure 2.1: The decay of $1-\log C(t)$ for varying friction constants γ. We can see that at low values of γ, the process is superlinear for short timescales (top curve). At higher values of γ, the curves are linear, indicating the diffusive regime. In this plot, $\delta t = 0.001$.

2.2.1.a Brownian Dynamics

In the previous subsection, we introduced the friction coefficients γ_T and γ_R, but did not discuss their implications. In fact, the magnitude of these coefficients sets the dynamics of the simulation by determining the diffusion. Specifically, the translational and rotational diffusion constants are inversely proportional to their respective friction coefficients. For low values of γ_T, simulations take place in the inertial regime, where the acceleration of particles plays an important role. If we increase γ_T to a high-friction regime, its term in Eq. (2.14) grows until $m\,\ddot{\mathbf{x}}(t) << \gamma_T\,\dot{\mathbf{x}}(t)$. This is the diffusive or overdamped regime. This distinction is of interest if we wish to observe the Brownian relaxation of colloidal particles, such as for the dynamic susceptibility calculations in Chapter 5. Simulations of this regime are referred to as Brownian Dynamics simulations. In principle, one can directly simplify the equations of motions. Alternatively, if one has an efficient Langevin Dynamics scheme, the overdampening approach can be used. Both γ and the timestep δt must be chosen appropriately.

An example of the tuneing process is shown in Figure 2.1, where the curves represent $1-\log C(t)$, where $C(t)$ is the autocorrelation function. In the diffusive regime, we expect the autocorrelation to decay exponentially, which means that the curves should grow as $\approx 1+at$. For $\gamma = 20$ (red), we observe that the curve is linear and that $a = \gamma\tau_B/\delta t$. As γ decreases, we can see that the curve has an initial non-linear regime (green), which flattens out to linear. That represents the inertial regime.

2.2.2 Pair Potentials

Now that we have established particles and relevant interactions, these must somehow be included into the simulation framework. More specifically, we will need some form of steric

exclusion to prevent particles from overlapping, as well as some descriptions of the electrostatic and magnetic potential energies from which we can calculate the forces acting on various particles.

Perhaps the most commonly known potential to model steric repulsion is the Lennard-Jones potential. However, it includes an attraction part that accounts for the close-range Van der Waals interaction. We consider electrostatic repulsion between platelets to be strong enough to also prevent Van der Waals aggregation, as seen by the colloidal stability in experiment. As we will assume that, even without explicit electrostatics included, our simulation particles are stabilized by the electrostatic repulsion of their surfactant coating, we do not include this additional attraction. An alternative would be some form of hard-sphere potential: however, due to the discontinuity, these are less popular in Molecular Dynamics simulations. Instead, we will use the Weeks-Chandler-Anderson potential[119]:

$$U_{WCA}(r) = \begin{cases} 4\epsilon\left[\left(\frac{\sigma}{r}\right)^{12} - \left(\frac{\sigma}{r}\right)^{6} + \frac{1}{4}\right], & r \leqslant r_c \\ 0, & r \geqslant r_c \end{cases} \tag{2.16}$$

where $r = |\vec{r}|$ is the distance between the centers, with a cut-off distance $r_c = 2^{1/6}\sigma$, and ϵ is the repulsion energy scale. This is a shifted version of the Lennard-Jones potential. It is also referred to as a soft-sphere potential, since the particles are compressible.

The magnetic dipole-dipole interaction of two particles with dipole moments $\vec{\mu}_i$ and $\vec{\mu}_j$ is given by

$$U_{dd}(\vec{r}) = \frac{\mu_0}{4\pi}\left[\frac{\left(\vec{\mu}_i \cdot \vec{\mu}_j\right)}{r^3} - \frac{3\left(\vec{\mu}_i \cdot \vec{r}\right)\left(\vec{\mu}_j \cdot \vec{r}\right)}{r^5}\right] \tag{2.17}$$

where, $\vec{r}$ is the vector connecting platelet centers and μ_0 is the magnetic vacuum permeability. In cases where an external magnetic field $\vec{H}$ is applied, its interaction with the particles is given by the Zeeman interaction:

$$U_H = -\mu_0\left(\vec{\mu} \cdot \vec{H}\right) \tag{2.18}$$

Finally, in some cases, we will include electrostatic interactions between the particles. This will be modeled using the screened Coulomb/Debye-Hueckel potential to implicitly account for the electrostatic effects of the solvent. Due to its form, this is also an example of a Yukawa potential, but it is termed Debye-Hueckel in this work in order to use consistent terminology with the ESPResSo implementation. In addition to the Bjerrum length l_B, the Debye length κ^{-1} is a parameter in the interaction potential:

$$U_{dh} = l_B k_B T \frac{q_i q_j e^{-\kappa r}}{r}. \tag{2.19}$$

where q_i, q_j are the particles' charges. This means that both the distance at which the charges

become comparable to thermal energy, and the strength of the solvent screening are implicitly considered.

2.2.3 Simulation Units and Rescaling

To attain greater generality, and to avoid potential numerical issues related to very large or small numbers, simulations are commonly run in reduced units. Analogously to the definition of International System of Units (SI), we will define the unit system of this work based on specific cornerstone values. The SI base units comprise time (s), length (l), mass (m), electric current (A), thermodynamic temperature (K), amount of substance (mol) and luminous intensity (candela). The luminous intensity will not be relevant in the context of this thesis. Similarly, the amount of substance will be abstracted out due to the coarse-grained nature of the model, and, since the aim of this is work is not to create an identical reproduction of the experimental system, all the masses treated in this work will simply be fictional simulation coefficients that serve to tune the timescale. This leaves the length, time (and mass), the thermodynamic temperature and the electric current (if electrostatics are considered explicitly) to be decided. All the works in this thesis will fix the length scale of $\sigma = 1$, where sigma is the thickness of one simulation particle. When matching the magnetic platelet cores in experiment, $\sigma = 1SU \approx 5\text{nm}$. The thermodynamic temperature is defined via fixing the energy scale such that $k_B T = 1$, where $T \approx 300K$.

The remaining mass/time scale of particles is not explicitly defined to match experiment, since the coarse-grained nature of the setup would not yield a realistic outcome and explicit timescales are not the focus of this work. Due to the anisotropic shape of the particles, it is necessary to set a mass and a tensor of inertia (see Section 2.2.4): these, as well as the timescale, are often tuned for sampling efficiency. In the case of the dynamic susceptibilities, where the relaxation times are relevant, the simulation values were calibrated to reproduce analytical results. The sole remaining timescale, electric current, is only partially made explicit in this work, and so will be discussed where relevant.

In coarse-grained simulations, the salient point of magnetics or electrostatics is often their interaction strength in reference to the overall energy scale. Moreover, the effective magnetization of and electrostatic repulsion between nanoparticles is nontrivial to measure precisely. This means that it can often be advantageous to define the magnetic properties in reference to the thermal fluctuation scale. In such cases, the dipolar coupling constant

$$\lambda = \frac{\mu^2}{k_B T \sigma^3} \tag{2.20}$$

will be used. In the notation used here, we intentionally fold the missing $\mu_0/4\pi$ prefactor into the

unit system. In simulations with both electrostatic and magnetic characterizations, we will convert explicitly from experimental values.

2.2.4 Particle Model

In order to create the platelet shape studied in this thesis, the simulation particles are composed of a rigid assembly of spheres. This is called the raspberry model, and is shown in Figure 2.2:

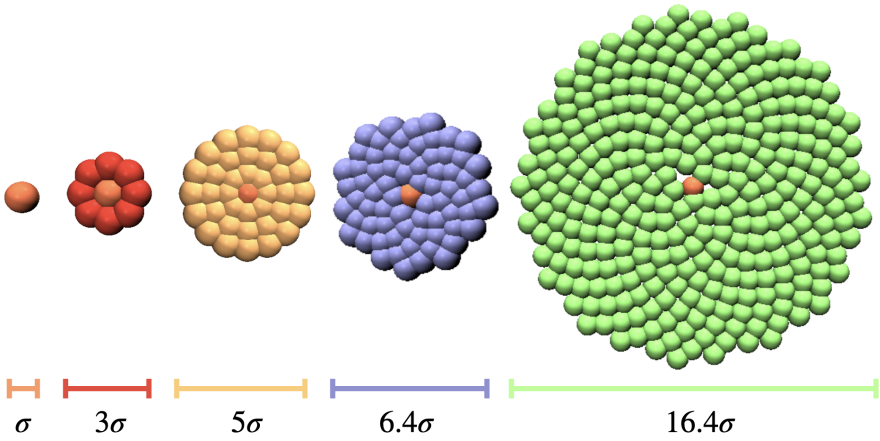

Figure 2.2: An overview of platelet models, with a sphere for reference (far left). The first two platelets (red, yellow) are constructed by equidistantly placing raspberry beads at a given radius. This method is more efficient for smaller aspect ratios. The next largest platelet was constructed using the Fibonacci spiral method, illustrating the boundary where this method still requires more spheres and shows some irregularity at the edges. At the far right, a very large platelet illustrates the aspect ratios where this method is advantageous, although there is still a characteristic central gap. For more convenient illustration, these renders are not fully to scale- the larger platelets have been slightly shrunk, and the sphere slightly expanded.

Several different variations in sphere placement were explored. Most simply, shown as the second from the left, a ring of spheres was placed around the central sphere. Depending on the aspect ratio, it can be necessary to use multiple concentric circles, and overlap the raspberry particles. As the aspect ratio increases, this method becomes computationally inefficient due to the increasing amount of particles. Since the thickness of the platelets was set to the reduced unit of $\sigma = 1$, the sphere placement problem reduces to the optimal distribution of points (particle centers) on a 2-dimensional disc, which can be solved by Vogel's disc method[120]. This consists of placing the centers of the particles on a Fibonacci spiral moving outward from the center of the platelet. The one caveat is that, since the diameter of the component spheres is $\sigma = 1$, the centers should have a distance of at least 0.5 from the edge of the disc. While this method is more efficient for large platelets, it can lead to inhomogeneous edges for small aspect ratio particles (unless many component spheres are used). However, it is easily adaptable for different aspect ratios, and the number of component spheres can be tuned.

Another advantage of the raspberry model is that we can choose to assign interactions to any

selection of the component particles. While these all require some form of steric interaction to maintain the shape, electric charges or magnetic dipoles can be placed arbitrarily. In the context of the raspberry model as implemented in ESPResSo[121], the equations of motion are be integrated for the central sphere, meaning that the raspberry component spheres are far computationally cheaper than a typical simulation particle. The overall platelet still requires an inertia tensor that is consistent with the anisotropic shape. For a platelet in the xy-plane with mass m and radius $r = d/2$, the diagonal elements of the inertia tensor are given by:

$$I_x = I_y = m(3r^2 + \sigma^2)/12 \tag{2.21}$$

$$I_z = mr^2/2 \tag{2.22}$$

These are the values calculated for a cylinder: as the platelets both in experiment and the current model do not have the additional curvature of an oblate spheroid. When calculating volume fractions, we will also consistently chose to use the volume of a cylinder, as this differs from oblate spheroids and as the component raspberry beads can overlap.

For the phase behavior of discotic nematogens, the exact choice of shape - oblate spheroid, cut-sphere, platelet - and surface has been shown to affect the phase behavior[122]. While this approach to modelling proved this most effective in the context of this work, it is by far not the only option. One popular approach for discotic nematogens is the use of the Gay-Berne potential[123], which was originally developed to emulate short rods. This potential has several drawbacks in the context of this work. Firstly, would require a certain amount of raspberry particles in any case, due to the lack of additional interaction sites at which electrostatic or magnetic interactions can be calculated. Second, and more crucially, the simplified model is not true to shape; it penalizes certain orientations over others. More specifically, the central thickness is reduced and the T-configuration is rendered less favorable. This effect is not very pronounced for aspect ratios below 1:5, but grows as the aspect ratio becomes greater. While the T-like configuration is not expected to be favored in simulation regardless, this bias is concerning. Moreover, the distortion in shape is so pronounced that it caused instability in some simulation tests.

2.2.5 Implementation

The simulations in this thesis were carried out using the Molecular Dynamics Simulation package ESPResSo[121]. The first paper and some of the first results were obtained using version 3.3.1, in the scripting language tcl, while subsequent results were obtained with versions 4.1.2 through 4.2, with scripting language python3. An advantage of using this package is that it already provided fast and efficient implementations of the relevant Molecular Dynamics integrator, thermostats, and pair potentials, including the use of p3m for dipolar interactions[124]. Data analysis was mainly

carried out in python3 and Mathematica, with gnuplot and vmd for additional visualizations. In latter sections, bond-order parameters were also calculated with freud-analysis. The software ColorBrewer v2.0 was used to assist in putting together palettes.

3 - Polydispersity in the Isotropic Phase

Much of the motivation to study magnetic nanoplatelet suspensions can be derived from their broad range of applications. In order to yield useful results, simulations must therefore be calibrated to match experiment. Furthermore, these first investigations should be able to narrow down the key properties of interest for future work. This chapter presents a study of low-concentration suspensions of magnetic nanoplatelets in the isotropic phase, as well as a field-induced nematic phase. Exploiting the precise control of platelet size and shape in simulation, we are able to contrast monodisperse suspensions with equivalent density monodisperse suspensions. We show how the polydispersity may lead to the reduction of the orientational and spatial correlations in the absence of an applied field, while simultaneously facilitating the field-induced transition into a nematic-like phase. Along with structural properties, we investigate the magnetic response. This allows us to confirm that, within the current model, the inter-platelet magnetic correlations have a negligible influence on the structure of low-density suspensions.

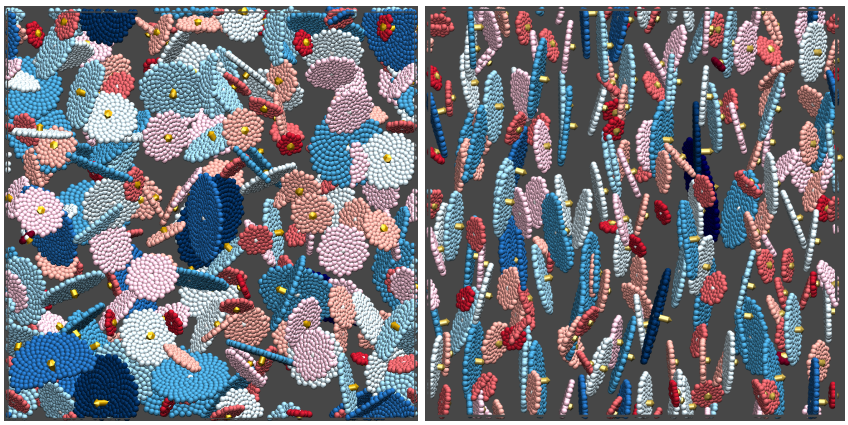

Figure 3.1: Simulation snapshots of a low concentration suspension of polydisperse colloidal magnetic nanoplatelets (around 15-115nm). Their color ranges from dark red to dark blue following their size, and the dipole moment is indicated by the golden arrow pointing out of the platelet's plane. Left: In the absence of an external magnetic field, the suspension is in an isotropic phase. Right: Applying an external magnetic field induces ordering, which causes the platelets to form a ferromagnetic nematic phase.

The material in this chapter has been published in:

[1] Rosenberg M., Gregorin Ž., Hribar Boštjančič P., Sebastián N., Lisjak D., Kantorovich S. S. and Sánchez P. A., *"The influence of polydispersity on the structural properties of the isotropic phase of magnetic nanoplatelets*", Journal of Molecular Liquids (2020), **312**, 113293,

3.1 Introduction

Magnetically responsive liquids are very appealing for a wide range of applications, as demonstrated by their extensive use in magnetic dampers and seals, biomedicine[26] vibratory energy harvesting[73–76], magneto-mechanical actuation and pumping in micro-magnetofluidics[77,78], magnetic control of light[79,80], targeted drug delivery[80,81] or magnetic field sensing and visualisation[82]. The unique properties of magnetically responsive liquids give rise to such an astonishing versatility of applications, yet make the fundamental understanding of such systems rather challenging.

As explored in Section 2.1, the anisotropy of interparticle dipolar interactions has not been found to give rise to spontaneous macroscopic polar ordering. It has been experimentally proven that discotic nematic ordering can appear in suspensions of non-magnetic nanoplatelets above a threshold concentration, mainly determined by the shape anisotropy and the electrostatic interaction[56,57,61].

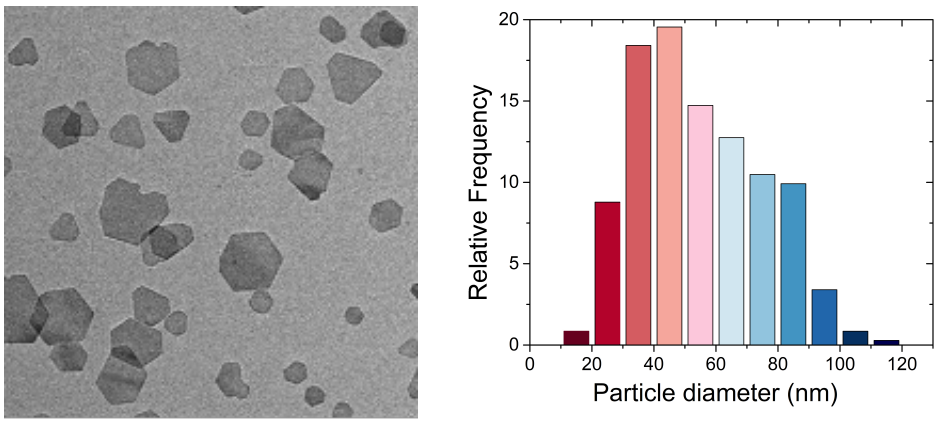

Figure 3.2: Left: TEM image of scandium-substituted barium hexaferite (Sc-BaHF) magnetic nanoplatelet suspension, as studied in this section. Right: A typical magnetic platelet particle main diameter distribution obtained in the experiment; this figure additionally serves as color key for all simulation snapshots in this chapter.

The work in this chapter is tailored to suspensions of scandium-substituted barium hexaferite (Sc-BaHF) magnetic platelets in butanol, with the same fundamental properties as those described in the first experimental realisation of spontaneous ferromagnetic order in liquid[46]. In that experimental system, while for low volume fractions only strong magnetic-field induced ordering is observed, above a certain threshold concentration, nematic ordering of the platelets takes place, resulting in a macroscopic magnetization. In contrast to ferrofluids made of spherical particles, the combination of shape anisotropy, screened electrostatic and magnetic interactions between the platelets, leads to positional and orientational correlations between the nanoparticles and creates ferromagnetic ordering. This is a simplified picture and for a full description, long-range magnetic many-body interactions need to be considered[125]. One of the remarkable observations of these systems is the formation of closed magnetic domain structures in thin rectangular capillaries and

under zero-field conditions, which are textbook examples for soft ferromagnets[126]. The theory of such platelets was barely investigated; partially due to their recent synthesis, and partially due to the complexity of interactions and parameters involved. Moreover, these platelets are polydisperse, which additionally makes the effects observed in these system dependent on the granulometry.

To close this knowledge gap, this chapter puts forward a minimal simulation model of magnetic nanoplatelets as shown in Figure 3.2. On its basis, we investigate the impact of platelets' polydispersity on the structural properties of the suspension below the isotropic-nematic transition, in which the reorientation of particles can be caused by an applied magnetic field. This allows us to control the transition point. Another advantage of the simulation approach is that one can study a purely monodisperse system not accessible in experiment, to understand the role of polydispersity.

3.2 Results and Discussion

3.2.1 Intrinsic Anisotropy

We begin the analysis of the influence of polydispersity on structural properties in the field-free case by computing center to center radial distribution functions $g(r)$[48]. These functions can only be computed for zero-field, low-density suspensions for the platelets, as only these conditions permit the system to remain disordered.

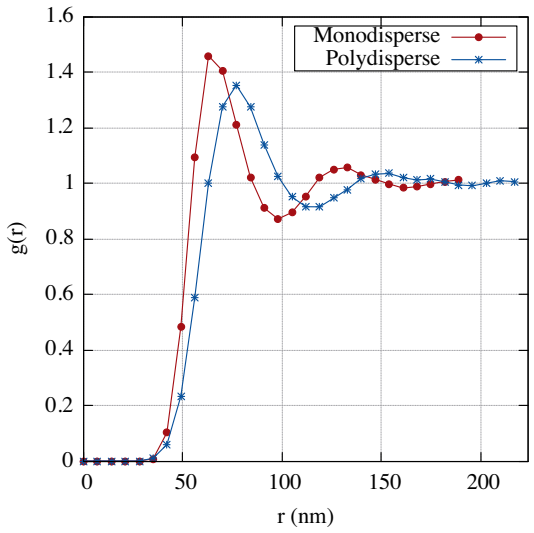

Figure 3.3: Zero field isotropic radial distribution functions, $g(r)$, of monodisperse and polydisperse systems. Red circles denote the monodisperse system, blue crosses refer to the polydisperse system. We see that the polydispersity causes a shift of the nearest-neighbor peak to greater distances, as well as a broadening of the peak.

In Figure 3.3, one can see that up to roughly 35 nm, $g(r)$ is zero, reflecting the weakness of magnetic inter-platelet correlations and the absence of stack formation. We observe that there is a clear preferred spacing between the platelets, at approximately $r = 63$ nm for the monodisperse case. This corresponds to approximately 1.5 platelet diameters. In the polydisperse case, this peak is shifted to a slightly larger separation due to the lognormal size distribution of the platelets, as the

average platelet is larger than the median used in the monodisperse case. The first peak of $g(r)$ of the polydisperse system is lower and broader than its monodisperse counterpart due to the variety of different platelet sizes. The comparison of the second peak, indicating the separation of the next nearest neighbours, shows that for the polydisperse systems this distance is barely pronounced, while it remains prominent for the monodisperse suspensions. This does not, however, imply that the monodisperse system is more correlated. Instead, the height differences can be attributed to the combinatoric spread in the distances, which results in the increased spatial disorder in the polydisperse case.

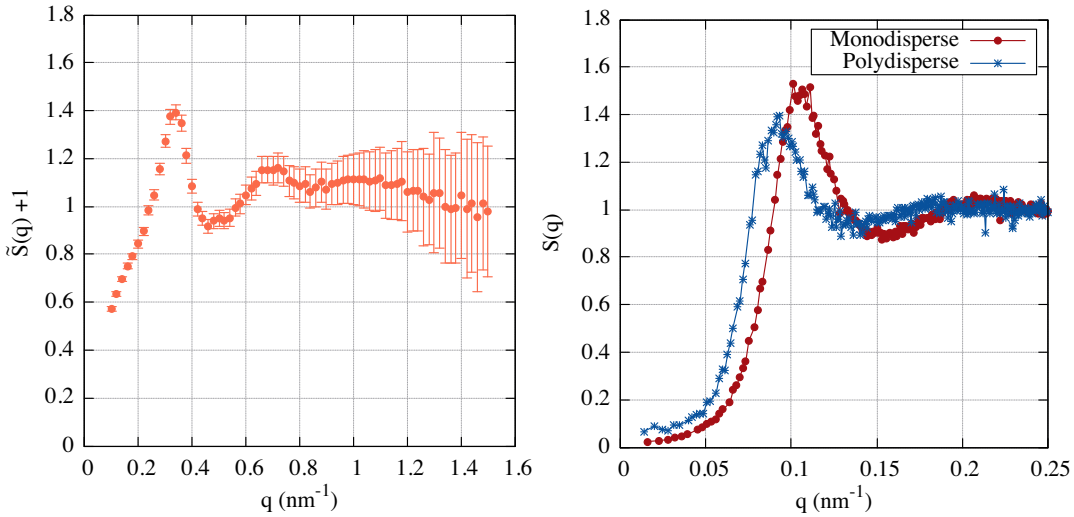

Figure 3.4: (a) Experimental data for $\tilde{S}(q)+1$. (b) Simulation results for the zero-field isotropic structure factors, $S(q)$, of monodisperse and polydisperse systems: red circles denote the monodisperse system; blue crosses refer to the polydisperse system.

As the radial distribution function cannot be measured in experiment, a different quantity must be chosen for comparison. Our experimental partners in Ljubljana performed small-angle X-Ray scattering (SAXS) measurements on the experimentally available polydisperse suspension in order to obtain the structure factor $\tilde{S}(q)+1$. This is depicted in Figure 3.4, including error-bars derived from the experimental measurements. In these experimental results, one can clearly see that the first peak is very pronounced and its position corresponds to the $q \sim 0.35$. The second peak is found at twice larger value of q. It must be noted that due to the particles' anisotropicity and polydispersity, and because the platelets' orientation and relative position are correlated, second term in the experimental structure factor cannot be decomposed into a product of the center to center structure factor and the square average of the form factor as it is usually done for spherical particles. This is a common issue in interpretation of SAXS or SANS data[127–129]. However, when the correlation peaks are distinctive as shown in Fig 3.4, qualitative comparison of the position of the correlation peaks with the structure function obtained from simulations data is still possible

and such analysis is justified.

This means that the overall shape of $\tilde{S}(q)$ qualitatively represents behaviour of the center-center $S(q)$, available in simulations and described by Eq. 3.1:

$$S(\vec{q}) = \frac{1}{N}\sum_{j=1}^{N}\sum_{k=1}^{N} e^{-i\vec{q}\cdot(\vec{r}_j-\vec{r}_k)}, \tag{3.1}$$

When considering the simulation structure factor, it is worth noting that the center-to-center structure factor calculation above does not consider the shape of the particles, neglecting any scattering from the extended discs, presenting an additional challenge for direct comparisons. Despite these issues, we find an excellent agreement in terms of peak height, peak separation and overall shape as shown in Figure 3.4. The monodisperse simulation result finds the peak at $2\pi/0.1 \approx 63$ nm and shows a secondary peak at roughly 2π / $0.2 \approx 31$ nm, which corresponds to the distance where the radial distribution function begins to be non-zero. In the polydisperse case, we also see the peak at slightly greater distances than in the monodisperse case, confirming what was shown by the radial distribution function.

To conclude this section, we can determine that the coarse-grained representation adequately describes the system of polydisperse magnetic platelets. Thus, one can conclude that the system's polydispersity leads to an overall spread in the characteristic inter-platelet distances. In the following sections, we will rely on simulation data to describe the structure of isotropic phase in greater detail, both in systems of poly- and monodisperse nanoplatelets.

3.2.1.a Bond-Order Parameters

In order to quantitatively characterize the spatial monomer distribution, we calculate the order parameters for platelet centers. In order to do that we obtain

$$Q_{lm}(\vec{r}_{ij}) = Y_{lm}\left(\theta(\vec{r}_{ij}), \phi(\vec{r}_{ij})\right), \tag{3.2}$$

where Y_{lm} are spherical harmonics of the respective order, lm, and the angles θ and ϕ are the azimuthal and polar angles of the displacement vector $\vec{r}_{ij}$ between two platelets in the lab reference frame. Only pairs of platelets with a separation is smaller than the value of the first RDF minimum as shown in Figure 3.3 (the nearest neighbor peak), are taken into consideration. The function $Q_{lm}(\vec{r}_{ij})$ is averaged over all such particles, i, j, then over time and, finally, over all simulation runs:

$$\overline{Q}_{lm} = \langle Q_{lm} \rangle. \tag{3.3}$$

The resulting cumulative bond order parameter Q_l,

$$Q_l = \left[\frac{4\pi}{2l+1} \sum_{m=-l}^{l} |\overline{Q}_{lm}|^2 \right]^{1/2}, \tag{3.4}$$

is plotted in Figure 3.5 as histograms. This was chosen to distinguish between different crystalline orderings which could be present in the system, based on the Q_l distribution[130].

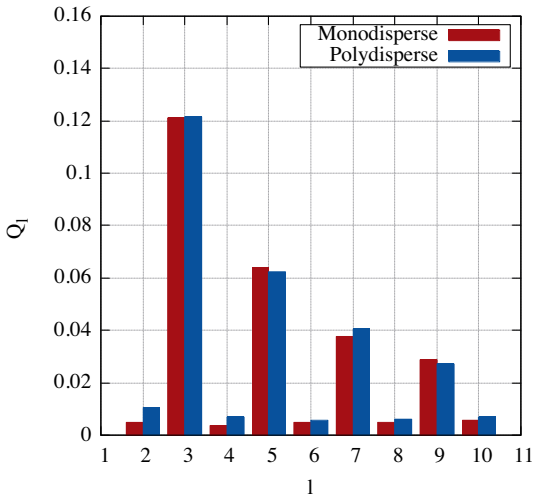

Figure 3.5: Bond order parameter Q_l, Eq. 3.4, as a function of l. Red indicates monodisperse, blue polydisperse suspensions. We see low ordering overall, with little difference between the two systems.

In Figure 3.9, one can see that the bond order parameters Q_4 and Q_6, which are indicative of crystalline order, are negligibly small. The largest value is obtained by Q_3, which might be attributed to a precursor to a honey-comb-like structure. However, the values of Q_3, as well as the other bond order parameters, are so low that the system is clearly in a fully liquid state for both mono- and poly-disperse systems. In general, Figure 3.5, shows that on the level of nearest neighbors the polydispersity does not affect the relative local structure, instead contributing to the long-range properties.

3.2.2 Impact of an applied magnetic field

To induce nematic ordering, we applied external magnetic fields between $H = 0.1$ (≈0.25mT, very low) and $H = 10$ (≈ 25mT, very high) to the simulated suspensions of monodisperse platelets and analysed both structural transformations and the magnetic response.

3.2.2.a Field-induced structural anisotropy

In this section we investigate the impact of an applied external magnetic field on the structural properties of both poly- and monodisperse systems. In Figure 3.6, we depict a set of simulation snapshots for a range of fields. Examining the top row of snapshots from left to right, we see that

the system remains completely isotropic for low fields (left), then, as the field goes above $H = 2$, begins to exhibit faint signs of an orientational alignment with the field (center), and appears strongly aligned once H grows to 8 (right). However, the ordering in the rightmost snapshot in the upper row is far from perfect.

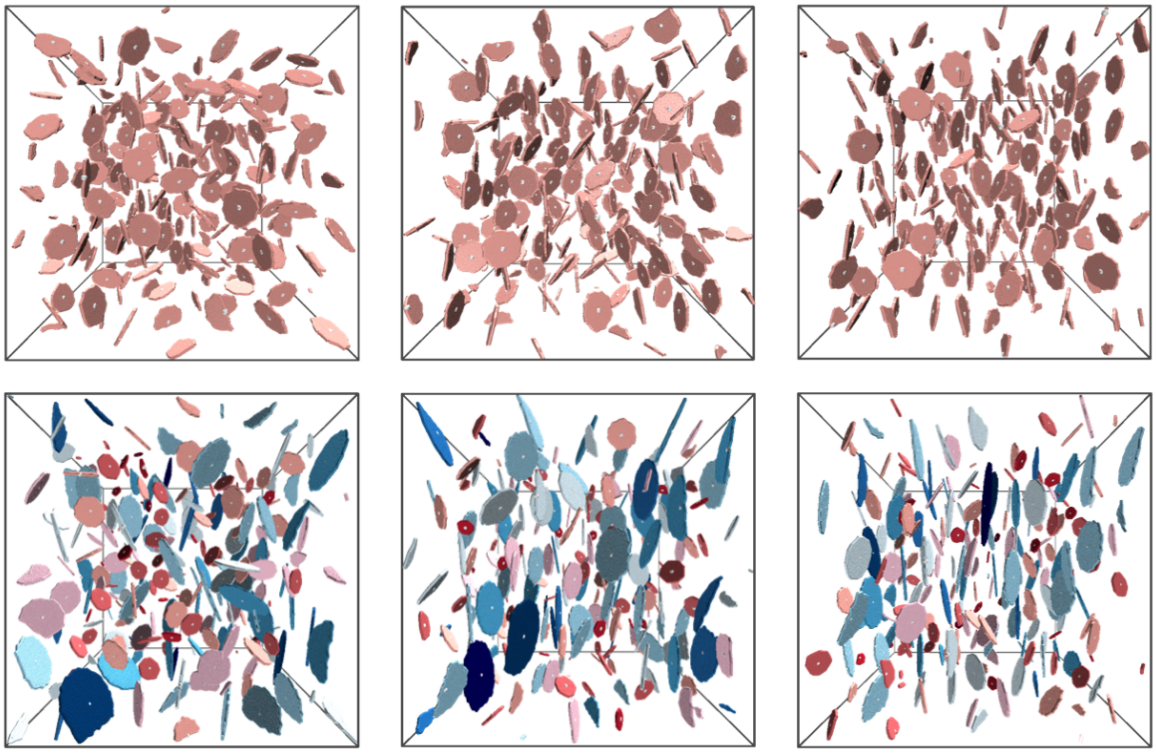

Figure 3.6: Simulation snapshots of the platelet system in fields of varying strength. The top row is monodisperse: (a) $H = 2$; (b) $H = 4$; (c) $H = 8$. The field points along x-axis and corresponds to the direction from the left to the right in the figure. The bottom row shows polydisperse systems: (d) $H = 2$; (e) $H = 4$; (f) $H = 8$. The color coding of platelet sizes corresponds to Figure 3.2.

In the polydisperse case, shown in the lower row, we see a much more pronounced shift occurring as soon as the field strength exceeds the median dipole moment, $H = 1$. For $H = 2$ (left) some platelets seem to be already aligned with the field H. Comparing the two central snapshots, in which $H = 4$, it is easy to notice that even a small fraction of highly anisotropic large diameter platelets is sufficient to induce much higher ordering than in the monodisperse case. The fact that large platelets have higher magnetic moments makes them more susceptible to weak fields. At the same time, their high anisotropy once they are aligned with the field perturbs the system. Thus in combination with the external field, the polydisperse system supports an earlier and more pronounced induced nematic-like ordering. For $H = 8$, as shown in right lower corner, the suspension of polydisperse platelets seems to be highly orientationally ordered. This agrees with the evolution of the order parameter shown in Figure 3.10, albeit with the ordering of the two

already coinciding for $H = 8$. This indicates that, while helpful, perhaps the larger size of more magnetic (and therefore more aligned) platelets in the snapshots can bias the visual perception.

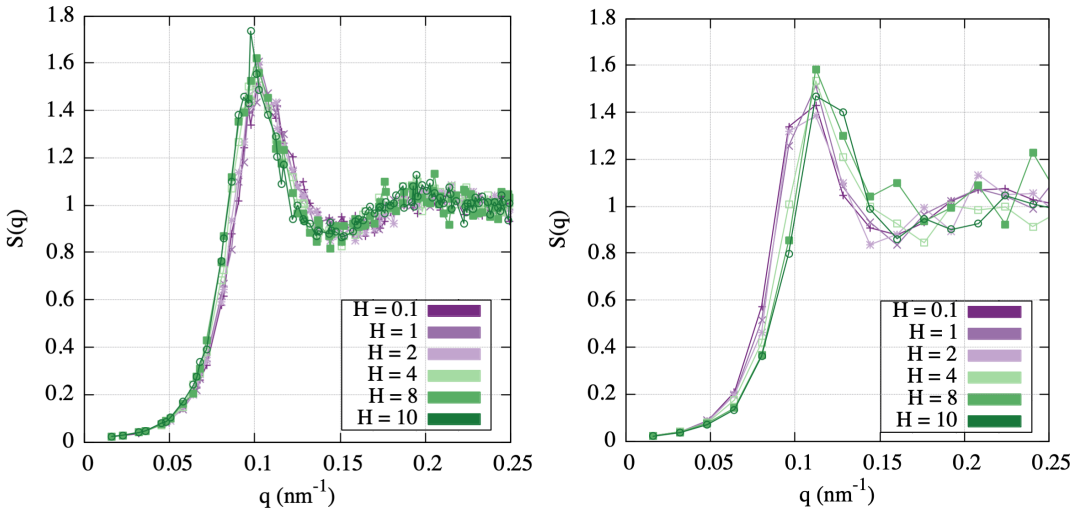

Figure 3.7: Structure factors of the monodisperse system; left, $S(q_\perp)$, calculated in the plane perpendicular to the vector of an applied magnetic field, H. Right: Structure factor, $S(q_{||})$, calculated along the field direction.

As we expect the system to become spatially anisotropic under the influence of an external field, H, the microstructural properties also must be characterized by a measure that takes this difference into account. Therefore, we calculated center to center structure factors parallel and perpendicular to the direction of H. This is done by splitting $\vec{q}$ into two components $q_\perp = |\vec{q}_\perp| = |(0, q_y, q_z)|$ and $q_{||} = |\vec{q}_{||}| = |(q_x, 0, 0)|$. The results for monodisperse systems are shown in Figure 3.7. The trends in ordering seen in the snapshots is reflected in the structure factor perpendicular to the field, which appears nearly identical to that of the zero-field suspension for fields lower than $H = 2$ (in purple), then shifts to larger distances as the field grows large (in green). The opposite trend can be observed for the structure factor parallel to the field, which is initially identical to that perpendicular to the field, then shifts to nearer distances as the field grows: one observes a small shift of the first peak position to the right (comparing the purple and green curves). Overall, the characteristic separation found in the field-free case is conserved up to fields of approximately $H = 2$: after this, the characteristic distance splits into a characteristic short separation parallel to the field and larger separation perpendicular as a nematic-like ordering of the platelets is induced by the external field. It should again be remarked that this is mirrored by the alignment of the platelets with the field, and we only consider center-to center distances- which means that the minimum separation between platelets that may come to lie in plane would have to be at least one platelet diameter. These effects do not constitute a sharp transition taking place at a specific field strength: one can see by observing *e.g* the peak heights for a field of $H = 1$ and $H = 2$ that the increased ordering of the platelets does not perfectly correspond to the field strength. Rather,

there is an intermediate regime with partial orientational and no positional ordering, when the field strength is comparable to the dipole moment.

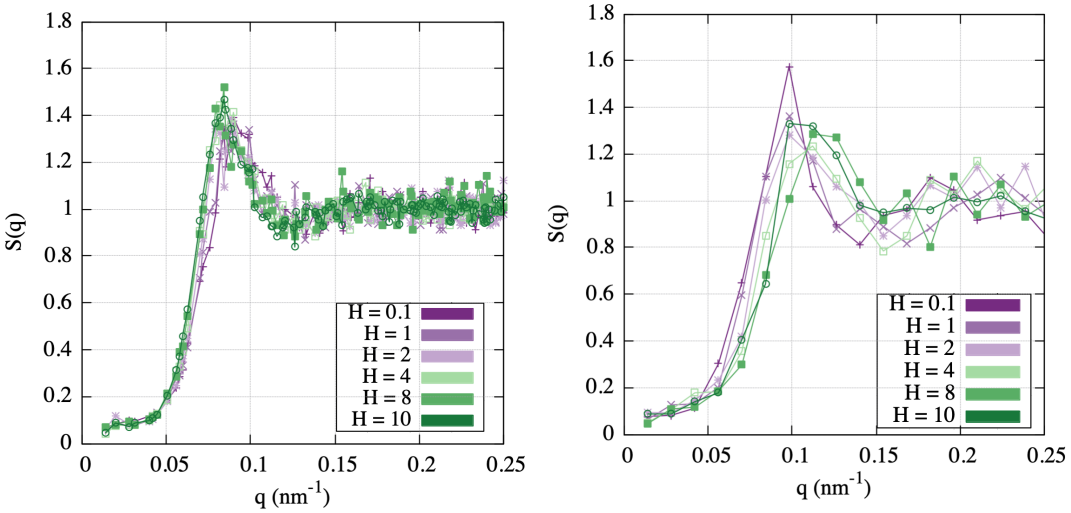

Figure 3.8: Left: Structure factor of the polydisperse system, $S(q_\perp)$, calculated in the plane perpendicular to the vector of an applied magnetic field, H. Right: Structure factor of the polydisperse system, $S(q_\parallel)$, calculated along the field direction.

On the left of Figure 3.8, in the structure factor of polydisperse suspensions, perpendicular to the field, the stronger ordering is reflected by a larger shift of the first peak into the region of smaller q, without the added noise of the monodisperse case. Again, we observe an initially isotropic structure factor at very low fields, which splits into a distinct lower separation parallel and greater separation perpendicular to the field. The orientational ordering could theoretically be accompanied by spatial ordering of the platelets centers.

Examining the bond order parameter in Figure 3.9, we see that the platelets do not adopt any specific ordering, as all values are below $Q_l = 0.5$. However, there is a distinct preference for the bond order of 3 across all field strengths, providing an indication that the system may be cultivating a honeycomb structure, which already appears at $H = 0$. Indications of this can also be seen in the analysis of the simulation snapshots. Concluding that platelets form a honeycomb structure would however be premature, as the bond order parameters value are so low that they are strongly affected by the noise of the gradual transition seen in the monodisperse system (see 3.6) in particular. In the polydisperse case, we again see the tendency towards a honeycomb-like structure which again appears uncorrelated with the field. In other words, orientational ordering caused by the presence of the low fraction of large platelets leads to a more notable evolution of the structure factor both parallel and perpendicular to the applied magnetic field, but it does not cause any spatial ordering of platelets centers.

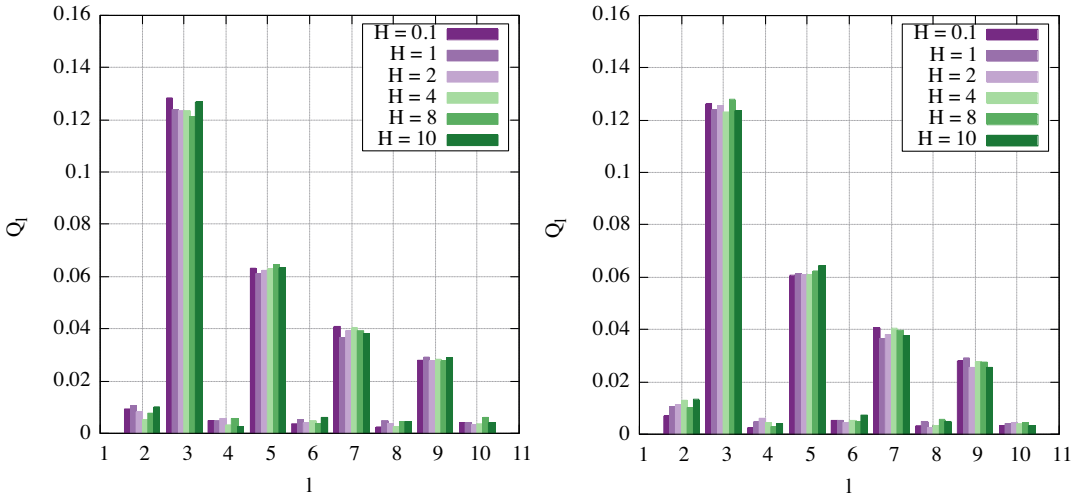

Figure 3.9: Bond order parameters calculated for different fields. The values of the field colour-coding is provided in (f) and is the same for (d) and (e).

3.2.2.b Magnetization curves

Figure 3.10 shows the magnetization M. The simulation results are indicated by symbols and analytical predictions indicated by lines. To ensure comparability, the simulation results were normalized by the saturation magnetization M_s, which was obtained by taking the direct sum of all magnetic moments in the system. As discussed in Section 2.1.4.a, the magnetization M_L of an ideal monodisperse superparamagnetic gas is given by the Langevin law[83,84]. For polydisperse systems, this can be generalized by weighting the integral average with the particle size distribution[85]. As we expect magnetic interparticle correlations to be present in this system, we chose to compare against second-order modified mean-field theory (MMFT2)[86]. The top curve uses the polydisperse generalization, while the lower curve represents the unmodified version.

Both simulation results are almost identical to the predictions of MMFT2, which in turn fully coincide with Langevin magnetization. This suggests that the platelets are magnetically uncorrelated. The reason for this is the very strong electrostatic repulsion, in combination with a very low number density. As it can be seen in Figure 3.10, the polydisperse system has a higher initial slope of $M(H)$, which represents the initial susceptibility. This can be attributed to a small fraction of very large, therefore strongly magnetic platelets in the polydisperse system.

On the right side of Figure 3.10, we can see the evolution of the nematic order parameter with increasing field H. It is important to note that this transition is not the same as the spontaneous, field-free case: it only corresponds to the influence of the external field, which is why it is juxtaposed with the magnetization curve. However, it serves to quantify an effect that we can see in the simulations snapshots Figure 3.6: the increased field response of the polydisperse system shows itself as a greater degree of alignment with the field, with $H = 2$ already crossing the

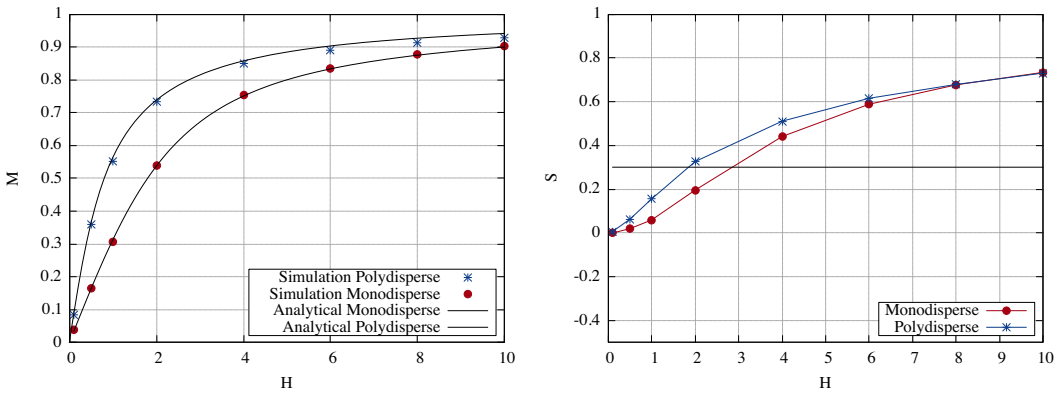

Figure 3.10: Left: Magnetization curves, where M and H are in simulation units and therefore dimensionless. Symbols represent simulation data, solid lines indicate predictions of (2.5) and (2.7). These coincide with simulation for both systems. Right: Nematic order parameter $S(\theta)$, using the field director as nematic axis. The black line represent the threshold value of $S(\theta) = 0.3$. Blue lines and star symbols are used for the polydisperse system; red lines and circles for the monodisperse case.

nematic threshold as indicated by the black line. This difference is most pronounced for low and intermediate fields. This could be explained by fact that the fraction of the larger, more magnetic platelets have a higher coupling parameter than the median, monodisperse platelets. At sufficiently strong field, there is no difference between monodisperse and polydisperse systems. We see that the strongest field of $H = 10$ is not enough to fully align as the platelets, although based on the magnetization curves, the system is almost fully saturated. One explanation for this would be that while the system is clearly nematic, the ordering is artificial, and would melt if the field were removed, as the density is too low to sustain a nematic phase.

3.3 Conclusions

This chapter presents the development of a coarse-grained molecular dynamics model which can qualitatively reproduce the experimental system for low densities and captures the structure of the fluid within reasonable expectations. The developed approach was applied to investigate the structure and the magnetic response of magnetic platelets as well as to elucidate the impact of polydispersity.

We have found that in the absence of an applied magnetic field both poly- and monodisperse systems are in a liquid state, with a preferred separation between platelets of approximately one and a half diameters. In the polydisperse case, the characteristic separations have a wider distribution that results in an overall less correlated system. These results are confirmed by SAXS measurements.

This correspondence changes drastically once the magnetic field is applied. Due to the presence of a small fraction of relatively large, highly anisotropic and strongly magnetic platelets in the

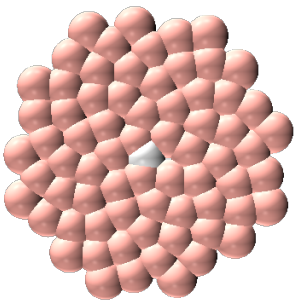

Figure 3.11: Raspberry model of the platelet. The central bead (white) carries the dipole moment perpendicular to the page plane, pink beads are raspberry beads, each of which carries a charge q as described in the main text and a steric WCA repulsion according to Eq. 2.16. All beads have a diameter $\sigma = 1$.

polydisperse suspension, weak fields already lead to the significant nematic-like ordering in the system. In the monodisperse case the platelets also orient themselves, but the application of a much stronger magnetic field is required. We calculated partial structure factors parallel and perpendicular to the field. For both poly- and mono-disperse systems we observed that for a sufficiently strong field, the characteristic distances in the plane perpendicular to the field increase, whereas those along the field get shorter. This splits the characteristic separation between platelets into a component parallel and perpendicular case, the former of which allows for a closer approach on average, which is promising, considering the platelets are expected to stack at higher densities and and form a ferromagnetic phase[46].

The analysis of bond order parameters has not revealed any pronounced long-range positional structuring of the platelets in suspension. However, we observe a precursors of a discotic honeycomb structure, which can be enhanced by the external field.

3.4 Methods

As described in 2.1, we use the "raspberry" model of MPL, with the Vogel's Method variant to generate platelets of different aspect ratio. The median platelet is shown in Figure 3.11. Due to an oversight, some of this work's platelets were 0.5 SU longer at specific edges than intended, as Vogel's Algorithm distributes simulation particle centers up to the boundary, which then have steric exclusion interactions from this center. This slight increase in particle anisotropy does not seem to have affected the results.

The dipole moment is scaled proportionally to the volume of the platelet magnetic core $v(n)$, such that $\mu(v(n)) = \mu_r \pi r^2 h$, where the constant μ_r is fixed such that the median platelet has a magnetic moment of 1 in simulation units. Even though the point dipole approximation might not be fully representative for the magnetization distribution of platelets shown in Fig. 3.2, it is a good starting point when investigating diluted systems with relatively strong electrostatic repulsion between platelet surfaces.

We consider electrostatic repulsion between platelets to be strong enough to also prevent Van

der Waals aggregation, as seen by the colloidal stability in experiment. Since the entire surface of the platelets should be repulsive, each raspberry bead carries this interaction potential with a charge of $q = Q/n$, where Q is the total platelet charge and n is the number of beads in the platelet.

3.4.1 Simulation Protocol

All simulations in this work were performed using the ESPReSso simulation package version 3.3.1[121] for Langevin Dynamics in the NVT ensemble. The timestep of the simulations is set to $\Delta t = 0.001$. All simulations were initialised by randomly placing $N = 200$ (monodisperse) or $N = 198$ (polydisperse) platelets in a simulation box sized such that the volume density corresponded to 0.04. In the polydisperse simulations, the particle size distribution was chosen by taking the relative frequency of the particle sizes in experiment (shown in Figure 3.2), doubling it and rounding to the nearest integer number of particles. The simulation then consists of 3 warmup blocks of 10000 integrations each. First, a capped block – the upper limit of forces in the system is set to a constant and all forces exceeding this value are reduced to this value – with only steric interactions enabled was run to safely distance overlapping particles. The second step was the introduction of the (initially capped) electrostatic repulsion, then in the final block the cap was removed and the magnetic interactions were enabled. After these warmups had concluded, the external magnetic field was introduced (if applicable) and we began to monitor the system energies. After approximately 60000 integrations the energy reached a steady fluctuation rate, at which point we began sampling the systems every 5000 integrations. These samples were later used to compute all the results depicted in the figures shown in this chapter. Overall, samples were drawn from 92 different simulation (re-)runs with varying field strengths, resulting in 60-300 samples for each system configuration, as (for instance) the polydisperse zero-field simulations required fewer checkpoints to produce statistically significant results.

3.4.2 Relation to Experiment

Firstly, we should note that all system parameters relevant to the simulation are described by the dimensions of length, time, mass and electric current. We set the reduced length scale by defining $\sigma = 1$ to be one platelet diameter, i.e. $l^* = 7\text{nm}$. This already allows us to compute $l_b \approx 0.46$ and $\kappa \approx 0.27$ by plugging in the values obtained in experimental studies[131] for the suspension of platelets in 1-butanol at a temperature of 25 °C. The remaining three dimensions are fixed by setting the average magnetic moment $2 \cdot 10^{18}$ Am^2 to 1 (thus fixing the electric current scale), then setting the unit charge $e_0 = 1.602176634 \cdot 10^{19}$ to 1 (fixing the timescale) and finally setting $k_b T = 1$ (fixing the remaining mass scale). This means that we are able to estimate the platelet charge for a given size by using the experimental measurement of the zeta potential[131]

and the formula for a sphere of an equivalent size[132], assuming $\psi_s \approx \zeta$:

$$Ze_0 = \frac{4\pi\epsilon\epsilon_0\kappa R_{eq}^2 k_B T}{e_0}\left(2\sinh\left(\frac{e_0\psi_s}{2k_B T}\right) + \frac{4}{\kappa R_{eq}}\tanh\left(\frac{e_0\psi_s}{4k_B T}\right)\right)$$

and calculate the magnetic moment of a platelet of a given size by scaling the average moment with the volume of the platelet. The external fields in simulation were set from $H = 0.1$ to $H = 10$, which corresponds to approximately 0.25 to 25mT. Since these considerations already fit the simulation system to experiment, two remaining potential parameters, the Lennard-Jones well depth ϵ and the magnetic Bjerrum length, are set to $\epsilon = k_b T = 1$ and $l_{BM} = 1/(k_B T) = 1$ respectively.

4 - Microstructure and Static Magnetic Susceptibility

This chapter explores the microstructure and initial static magnetic susceptibility of anisometric magnetic nanoplatelet systems in order to understand the applicability of dipolar sphere-based theories and models. We find that the microstructure of the magnetic platelets characterized by the particle distribution and magnetic clustering of platelets diverges significantly from that of spheres both quantitatively and qualitatively. The initial static magnetic susceptibilities in nanoplatelet systems are shown to be lower than in comparable suspensions of dipolar spheres. At lower values of the magnetic coupling constant λ, this can be accounted for by applying corrections to the volume fraction. However, this approach is less accurate for systems with stronger magnetic interactions. We introduce an adaptation of the chain-correction model of modified mean-field theory. It finds the same value of the magnetic coupling for the experimental data as simulations would predict to generate the experimentally suggested microstructure.

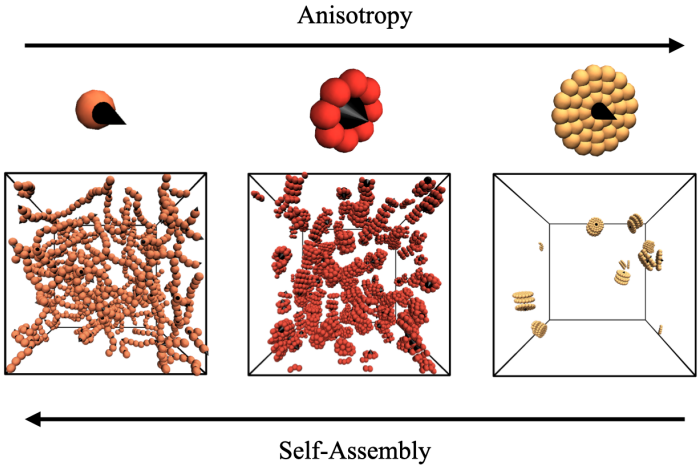

Figure 4.1: As the shape anisotropy of the particle grows from the isotropic sphere to increasingly anisotropic platelets (top row), we see that the quantity of self-assembly in the system (lower row) decreases. Top row: The simulation particle model for spheres (left), aspect ratio 1:3 platelets (center) and aspect ratio 1:5 platelets, with the black arrows indicating the fixed orientation of the dipole moment. The lower row compares the self-assembly in simulation snapshots: the volumetric density ϕ is constant, but only particles which have self-assembled into at least a dimer are shown.

Most of the material in this chapter has been published in:

[2] Rosenberg M., S. Kantorovich, "*The influence of anisotropy on the microstructure and magnetic properties of dipolar nanoplatelet suspensions*", Physical Chemistry Chemical Physics (2023), **25**, 4, 2781-2792

[3] H. Nadasi, M. Küster, A. Mertelj, N. Sebastián, P. Hribar Boštjančič, D. Lisjak, T. Viereck, M. Rosenberg, A. O. Ivanov, S. Kantorovich, A. Eremin, F. Ludwig, "*Role of ionic surfactant in magnetic dynamics of self-assembled dispersions of nanoplatelets*", Journal of Molecular Liquids (2023), **382**, 121900-,

4.1 Introduction

As it has been shown that particle shape strongly affect the overall microscopic properties of such suspensions[88], this chapter sets out to quantify the varying microstructures of magnetic nanoplatelet suspensions and their effects on the static magnetic response. Building on our knowledge of dipolar hard sphere systems's rich phase diagram, and the ordered phases of hard nanoplatelets, we explore the interplay between the shape and magnetic properties. The preliminary investigations in the first chapter of this thesis showed a remarkable lack of influence of the interparticle correlations: in order to proceed with this work, we will need to question our initial assumption that, aside from the ordered phases, dipolar magnetic nanoplatelets would behave very similarly to spheres, or possibly to ellipsoids. Early computational[133] and experimental[134] investigations of discotic systems focused primarily on the orientations and isotropic-to-nematic phase transition of the suspensions.

The work explored in this chapter targets a different region of the phase diagram: keeping both the concentration and aspect ratio of the colloids well below the threshold for a liquid-crystalline phase transition, we simulate systems of discs with varying aspect ratios to examine if their structural properties deviate from those of dipolar spheres. Our goal is to understand whether or not there are shape effects aside from the mesogenic properties, and if so, how they impact the magnetic properties of the system. To maintain a broad range of applicability, we will condense the influence of the factors listed above into three key parameters: the aspect ratio, given in disc thickness to diameter (e.g. 1:3), the volume fraction ϕ and the magnetic coupling constant λ, which is used to characterize the strength of magnetic interactions relative to the thermal energy scale of the system. These three system parameters will provide the framework with which to explore the properties and phases of the system.

4.2 Results

In order to lend a visual aid to the different system properties discussed in this section, we show the three different particle aspect ratios examined in this chapter in Figure 4.2. From left to right, we see a sphere (aspect ratio 1:1), a platelet with moderate anisotropy (aspect ratio 1:3) and a platelet with strong anisotropy (aspect ratio 1:5). These aspect ratios were chosen to sample the region where the anisotropy is both pronounced enough to influence the microstructure, and low enough that the isotropic to nematic phase transition does not occur at the densities studied.

Although a quick count shows that the rightmost platelet contains 7 spheres across one diameter, due to their overlap, the resulting aspect ratio is only $1:5$. Further discussions of the model and technical challenges can be found in Section 4.4.

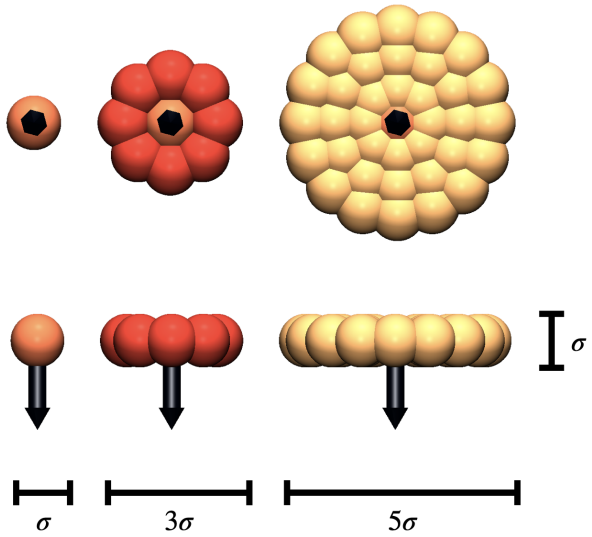

Figure 4.2: Simulation particle models for spheres (left), platelets with aspect ratio 1 : 3 (center) and platelets with aspect ratio 1 : 5 (right). The black arrows represent the position and orientation of the particles' dipoles, which are fixed relative to the platelet throughout the simulation.

4.2.1 Phase microstructure

As a general note, due to the large number of parameter sets explored, each plot will only show one representative curve per type of structure or behavior observed. Unless otherwise specified, this means that if, for a given λ, only a very low and very high ϕ are shown, the curves for all other densities can safely be assumed to lie between the two.

4.2.1.a Spatial distribution of particles

We begin this chapter with the classical center to center radial distribution function of the particles, which shows the quantity and proximity of the nearest neighbors of each particle. This can tell us if the system is in a gaseous, liquid, or otherwise structured state, where, in such magnetic system, the "structured" typically refers to the formation of chains, rings, networks or branched structures of self-assembled magnetic nanoparticles.

Examining the radial distribution of dipolar spheres in Figure 4.3 as a reference, we see a gaseous state regardless of density for $\lambda = 1$ (green curves). Increasing λ to three (blue curves) already results in the formation of an early nearest-neighbor peak. This peak flattens out with increasing density. At $\lambda = 5$ (purple), the radial distribution function indicates that the system has some clusters with regular spacing (suggesting chains or rings), as well as particles at intermediate distances. This persists despite the flattening of the curve at higher densities. At $\lambda = 7$ (orange) and $\lambda = 10$ (red), the distribution function shows a shifted and even more strongly structured version of the curves corresponding to the smaller λ values. This effect arises due to the dipole

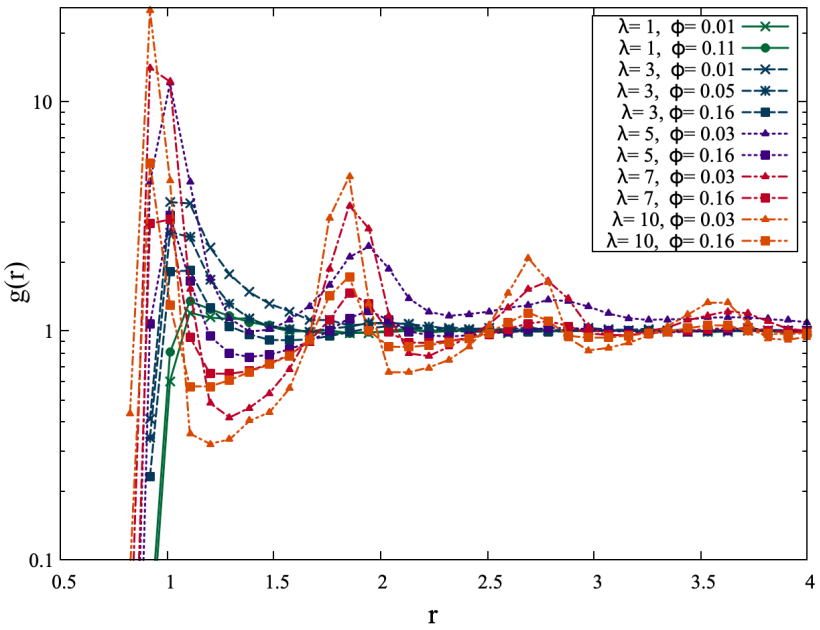

Figure 4.3: Radial distribution functions $g(r)$ of dipolar sphere particles for varying magnetic coupling λ and volume fraction ϕ. We observe initial gaseous states for low λ (green), followed by some form of self-assembly for all higher values of magnetic moment. At high λ and high ϕ, we see the most pronounced structuring with peaks and valleys persisting at longer ranges.

moment being strong enough to overcome part of the steric particle repulsion, shifting the nearest-neighbor peak from the Weeks-Chandler-Anderson minimum[135] of $2^{1/6}$ (≈ 1.12) to 0.9. Although the two highest λ values would appear a featureless dense network in simulation snapshots, the radial distributions show that they are assembled with clear spacing.

For systems of platelets with aspect ratio 1:3, Figure 4.4 shows that the $\lambda = 1$ and $\lambda = 3$ systems (blue and green curves) are in a gaseous state. At $\lambda = 5$ (purple), the shape of $g(r)$ begins to change as some close-range pairs form, although even at the highest density the system remains non-assembled and spatially isotropic overall. The actual self-assembly into pairs begins at $\lambda = 7$ (red), with a peak for the nearest neighbors that increases with higher density. At the next increase of magnetic moment, $\lambda = 10$ (orange), we can see that the system is already assembled into regularly spaced structures. Comparison with simulation snapshots shows that this corresponds to the regime where long chains are formed. This results in a clear pattern of $g(r)$. However, it needs to be noted that in this regime the chain lengths have become comparable to the box length, which means the last curves must be interpreted qualitatively. Aside from the fundamental differences that dipolar spheres' radial distribution functions evolves with λ to show an initially gaseous phase moving to a fluid with increasing levels of regular structure, as opposed to the gaseous, then suddenly highly periodic radial distribution of aspect ratio 1:3 platelets, it should also be noted that the process of this evolution is quite different between the two suspensions. In

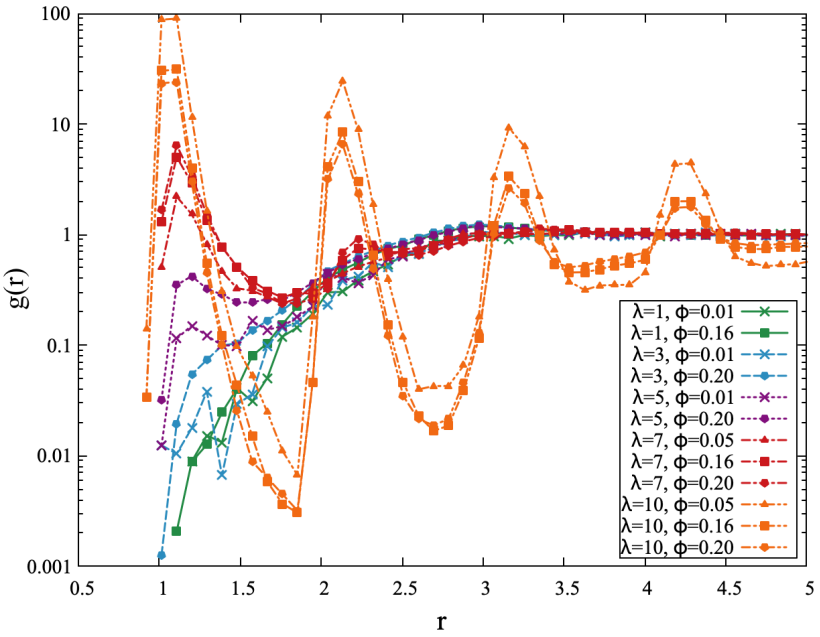

Figure 4.4: Radial distribution functions $g(r)$ of aspect ratio 1:3 particles for varying magnetic coupling λ and volume fraction ϕ. We observe initial gaseous states for low λ (blue, green, purple), some clustering for $\lambda = 7$ at high ϕ (red, square and polygonal points) and the formation of long chains at very high λ (orange).

systems of spheres, there is a gradual increase of peak height with λ and dependence on ϕ, with little qualitative change between systems adjacent in parameter-space. For platelets, there is a rather abrupt transition from $\lambda = 7$ on, with no overlap between different values of λ.

At the highest aspect ratio investigated, 1:5, shown in Figure 4.5 we observe a similar progression as with aspect ratio 1:3. Since this system faces the same issue of chains approaching box length for $\lambda = 10$, we omit those curves and focus on tracking the transition from the gaseous state to the beginnings of the assembly process. The lower values of $\lambda = 3$ and $\lambda = 5$ (light blue, light purple) are clearly still gaseous in the case of aspect ratio 1:5 platelets, with the same hint of a nearest-neighbor peak at the higher densities just over the distance of one diameter (5-less visible in logscale). The shape of the curve is slightly flatter due to the larger spread of interparticle distances due to the shape (with the closest contact distance between 1 and 5 depending on the mutual orientation). Interestingly, we see that while $\lambda = 7$ does start to form a peak at the assembled distance for the highest density (pink polygons), it is still below 1 despite the next increase of λ leading to a fully chained regime. This indicates that the transition from an isotropic to a self-assembled state is either shifted to higher λ, or takes place in a narrower region of the phase space. All the peaks found for aspect ratio 1:5 platelets' system monotonically increase with density.

We can see this behavior reflected in the center-to-center structure factors $S(q)$ as well, shown in Figure 4.6 and Figure 4.7. In the first figure, the structure factor of dipolar spheres at a higher

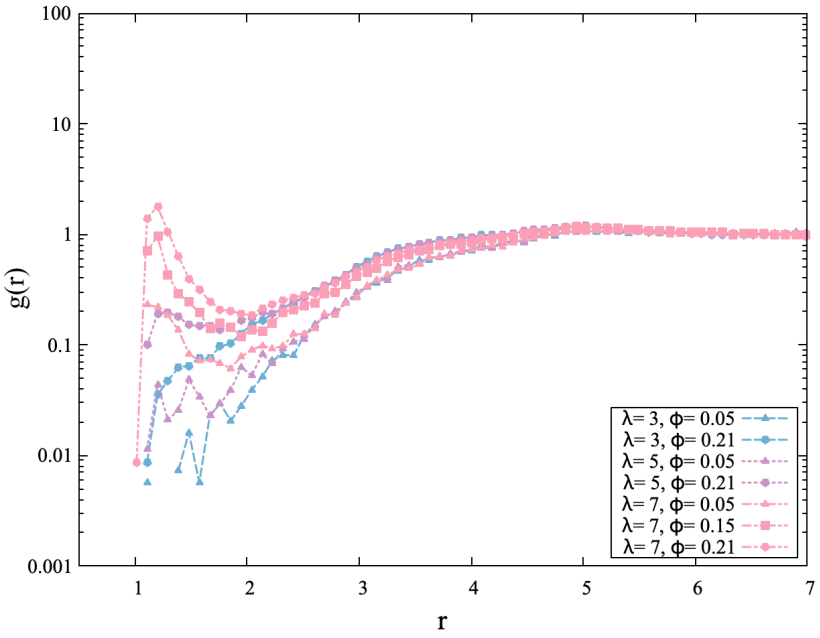

Figure 4.5: Radial distribution functions $g(r)$ of aspect ratio 1:5 particles for a reduced set of magnetic coupling parameters $\lambda \in 3, 5, 7$ and volume fractions ϕ. We observe initial gaseous states for essentially all λ (light blue, light purple, pink) with a suggestion of a peak for the highest density and λ shown (pink polygons).

density ($\phi = 0.15$) shows an increase in isothermal compressibility even at the lower $\lambda = 3$, before significant self-assembly. This effect grows more pronounced with increasing λ. At $\lambda = 7$, we can also see that the nearest neighbor peak increases in height and shifts to higher q values, accompanied by the $S(q)$ values at low q also increasing. This suggests the formation of a percolating network.

As these effects have already been studied in detail (see e.g.[136]), we will focus our attention on the left side of Figure 4.7, which shows the same λ and ϕ values in a system of aspect ratio 1:3 platelets. For $\lambda = 3$, this platelet ferrofluid is in a simple liquid phase. Increasing λ does show a clear effect, with the formation of a second peak (corresponding to the onset of self-assembly) and a shift of the first peak. However, this structuring is much less pronounced than that of even $\lambda = 3$ dipolar spheres, despite both having low self-assembly. Finally, on the right side of Figure 4.7, we see that the structure factors for aspect ratio 1:5 platelets the structure factors are essentially identical within the statistical precision reached and correspond to a homogeneous liquid.

Having discussed the onset of clustering and the progression of phases of the system, we now turn to investigating the clusters themselves by quantitatively characterizing the development of the clustering with increasing λ and ϕ. As before, we begin by showing a reference system of dipolar spheres in Figure 4.8. For $\lambda = 1$ (green), we see that the particles are mostly dispersed, with a clear progression towards small clusters at very high densities. This same effect takes place on a shifted scale for $\lambda = 3$. It is important to note that the clustering criterion cutoff used here

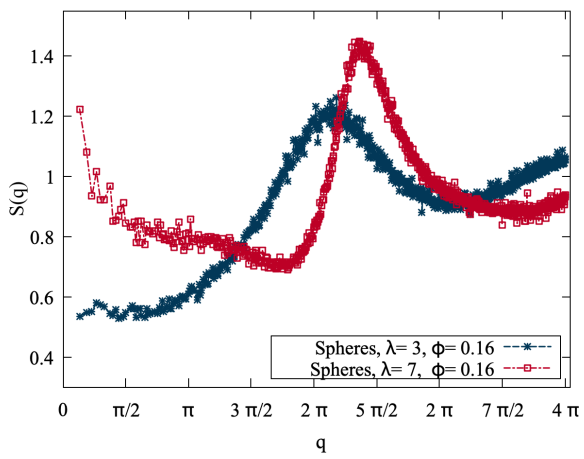

Figure 4.6: Structure factor $S(Q)$ of dipolar soft spheres at density $\phi = 0.15$, with $\lambda = 3$ (blue, stars) and $\lambda = 7$ (red, hollow squares). The spheres show a pronounced structuring that is strongly affected by λ.

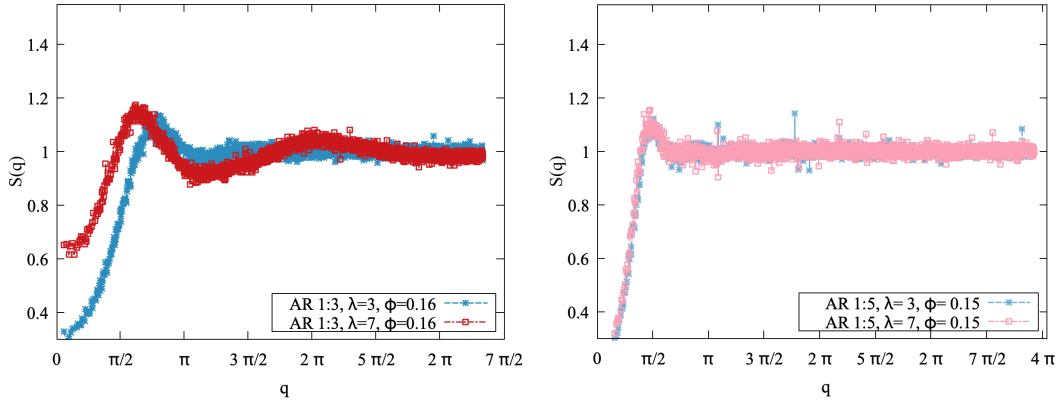

Figure 4.7: Structure factors $S(Q)$ of aspect ratio 1:3 platelets (left) and aspect ratio 1:5 platelets (right) at density $\phi = 0.15$, with $\lambda = 3$ (blue, stars) and $\lambda = 7$ (red, hollow squares). While the spheres showed a pronounced structuring that is strongly affected by λ, only aspect ratio 1:3 platelets with high λ show structure beyond that of a homogeneous fluid.

was adapted from that used in similar studies[88]), which is discussed in greater detail in the Section 4.4. This ensures greater comparability between dipolar sphere and platelet system, but causes a slight deviation from the literature in terms of the onset of clustering for low λ. At $\lambda = 5$ (purple), clusters dominate from the outset and large clusters begin to form. Finally, both $\lambda = 7$ and $\lambda = 10$ show networks encompassing almost all particles as the dominant structure, except for the lowest densities, where distinct intermediately sized clusters can still coexist. Comparing across all systems, we can roughly parse 3 regimes. In the first regime, at the lower ends of the lambda and density ranges, dipolar interactions do not play a significant role in the overall system structure. While particles can self-assemble, these clusters remain small. Regime 2 is the clustered region of the phase diagram, where different sizes and types of clusters coexist. Based on studies of similar systems[137], we expect the system to form rings (closed-flux structures) that are inherently limited in size, so this range of cluster size deserves its own mention as a distinct region of the

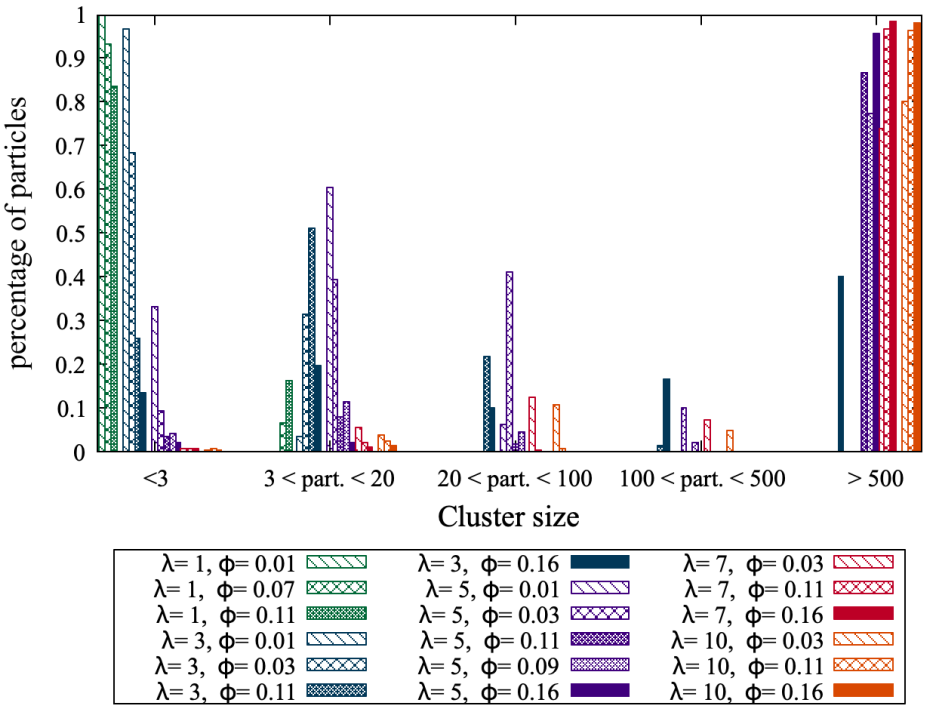

Figure 4.8: Histogram depicting the percentage of spheres in a cluster with n particles. The color indicates the value of λ, the fill indicates the volume fraction ϕ. We see that increasing the value of λ (warmer colors) or increasing ϕ (more filled bars) leads to the majority of particles being contained in larger clusters.

phase behavior, as opposed to an intermediate state. Ultimately, for the highest λ and density, the system collapses into a (fully) networked state. At the high λ and ϕ limit, it is difficult to give confident quantitative statements as the exact density at which the system transitions to a fully networked state can be influenced by the box-size. For the purposes of this chapter, we restrict ourselves to pointing out that qualitatively, the limiting case of the system behavior for dipolar spheres is as described.

Slightly deforming the aspect ratio from 1:1 to 1:3, we already expect a decrease in cluster formation based on the radial distribution functions. One naive conjecture based on the clustering shown for spheres is that platelets do show the same qualitative and quantitative behavior, simply shifted by density- while a unit sphere has a volume of $v_s = \frac{4}{3}\pi r^3 = \frac{\pi}{6}$, a $1:3$ platelet has the volume $v_p = \pi r^2 \cdot h = \frac{9\pi}{4}$, which corresponds to a ratio of $v_s : v_p$ equal to $1:13.5$. Examining Figure 4.9 shows significantly less clustering: none for any of the densities for $\lambda < 7$ (save a minuscule percentage at $\lambda = 5, \phi = 0.2$). The shift to small clusters observed in $\lambda = 7$ could be argued to resemble the behavior of $\lambda = 3$ for spheres; however, this breaks down at $\lambda = 10$ when assembly does occur, but clearly peaks in an intermediate regime not favored by dipolar spheres.

The aspect ratio 1:3 platelets do not exhibit this intermediate peak, going from majority isolated to majority clustered in assemblies of $20 < n < 100$ particles. The largest clusters sizes shown to

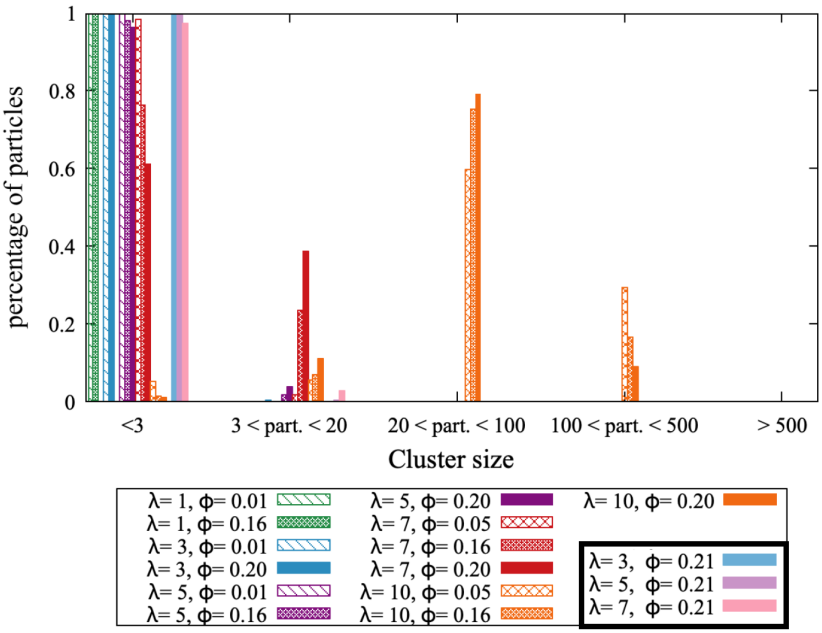

Figure 4.9: Histogram depicting the percentage of aspect ratio 1:3 (bright colors) and aspect ratio 1:5 (pastel colors, black box in legend) particles in a cluster of size n. We see that clusters only form for high values of λ (orange and red), and that none of the large clusters observed as high λ, ϕ limit for spheres are formed.

be the limiting cases to not appear at all. It could be argued that by increasing λ sufficiently, larger clusters might be attained. For this argument, it is instructive to question what sort of structures platelets can be expected to form, as it is not clear if platelets can form the networks of branched structures necessarily to achieve such large clusters considering the interplay between the steric repulsion and the weakened dipolar interactions due to the greater distances. We expect platelets to form stacks (the equivalent of chains in spheres), which should grow in length for increasing λ: due to the steric repulsion, we would not expect rings or strongly curved structures to form.

The clustering of platelets with aspect ratio 1:5 was integrated into Figure 4.9 as its meaningful quantification is quite succinct: there is no clustering for $\lambda < 7$ (pastel blue and purple), a very small fraction for the highest density at $\lambda = 7$ (pink) and a jump to long chains for $\lambda = 10$. The latter could not be evaluated quantitatively due to issues with equilibration, as the chains spanned the box length. These discrepancies in clustering are not purely a question of volumetric differences. While the different density surely places a role, it is clear from Figure 4.9 that shifting ϕ would not be sufficient to transform the platelet distribution into those formed by spheres.

This is explored further in Figure 4.10, which shows a more detailed cluster size distribution for spheres and aspect ratio 1:3 platelets at fixed densities. Based on previous work by Sciortino et al.[138–140], we expect that the size distribution of clusters of dipolar spheres should follow a power law as given by Wertheim theory. If we examine the curves marked with spherical points, we find

excellent agreement with studies of defect clusters[140] for clusters with 3 to 100 particles, which show a clear linear trend. For the platelet clustering (stars), the limited clustering for $\lambda = 5$ is still linear. The next highest value, $\lambda = 7$ is arguably still similar to trends for lower-λ spheres: however, $\lambda = 10$ (orange curve) does not follow any form of power law.

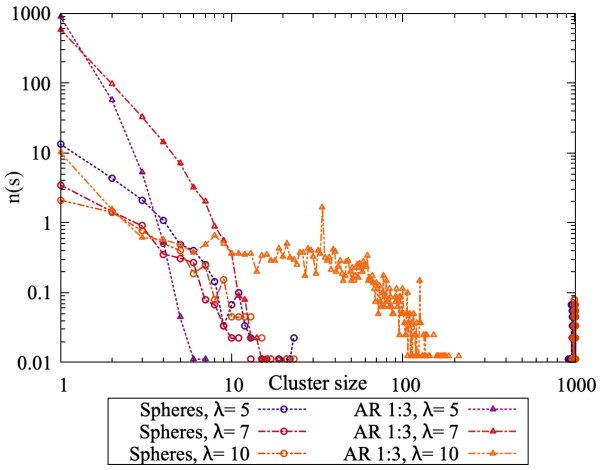

Figure 4.10: The average number of particles n in clusters of size s, normalized by the number of checkpoints, shown for the fixed densities $\phi = 0.03$ (spheres) and $\phi = 0.16$ (aspect ratio 1:3 platelets). The systems of dipolar spheres (lines with circular points) agree with the Wertheim theory, systems of platelets (stars) either do not cluster sufficiently (purple) or strongly diverge from any expected power law (orange).

Another explanation could be that differences in structures formed plays a role in the quantity of clustering. As the platelets are rigid, they are not able to self-assemble into certain compact structures - such as rings - due to steric exclusion. Perhaps the lower clustering only reflects the difference in configuration space due to the shape?

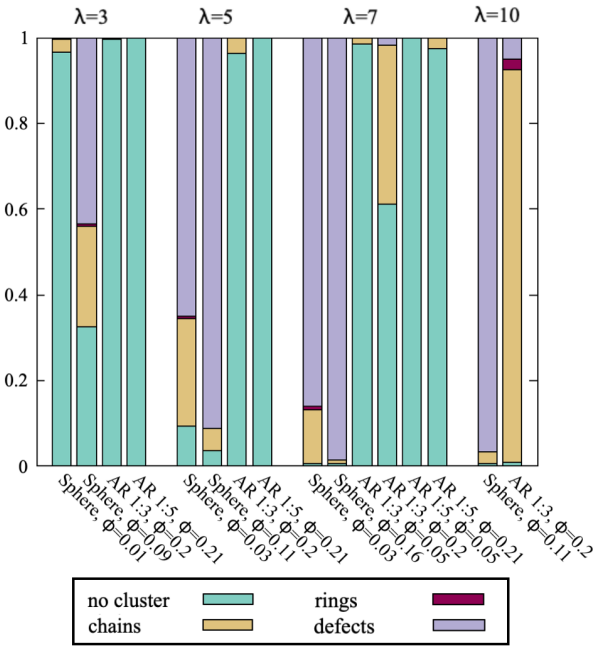

Figure 4.11: Percentage of particles either not clustering (green, lowest bar), forming defect-free chains (gold, second bar), rings (red, third bar) or branched structures with at least one defect (purple, top bar). We see that the proportions of particles in these different assembled structures are different for spheres and platelets, with the former favoring branched structures and the latter favoring chains.

In order to explore this hypothesis, we study which microstructure motifs are formed and

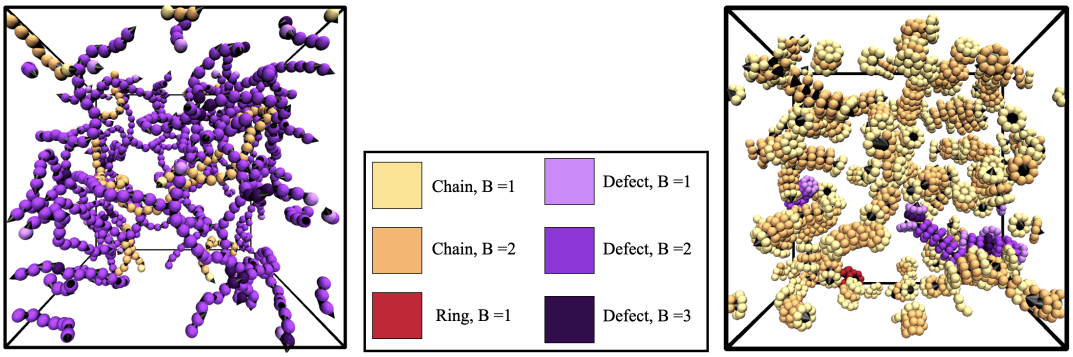

Figure 4.12: Two simulation snapshots of (left) dipolar spheres at λ=7, $\phi = 0.03$ and (right) aspect ratio 1:3 platelets with λ=7, $\phi = 0.16$. Particles which are not part of any structure are not shown. We see a network of branched structures has formed in the system of dipolar spheres, with a few independent spheres. For the platelets, there is a "ring" of three particles in red -argue-ably also a defect due to the lack of flux closure- , and two "defect" structures in purple. The small black cones placed on the particles represent the dipole orientations- these are present for all particles, but given lower visual priority than the particles (*i.e.* only visible when not covered by any other particle component).

the relative frequency of their occurrence. Figure 4.11 shows the percentage of particles which are either: not in clusters (singlets and pairs, fewer than 3 particles), in defect-free chains, in rings or in branched ("defect") structures, i.e. self-assembled structures that contain at least one defect. As defect structures for dipolar spheres have already been studied in-depth for comparable systems[140], we do not engage in further discussions of the different defect types and relative frequencies. For spheres, defect structures rapidly begin to dominate over all other structures, with some chains and, at specific densities, rings. The lack of the latter is due to the higher densities studied. The proportion of defects to chains does not change significantly once λ is sufficiently high. For aspect ratio 1:3 platelets, we see an entirely different progression. There is very limited assembly into chains, even for high λ, until for very high $\lambda = 10$ chains come to dominate the assembled structures. While there is a small fraction of rings at the highest densities, these were revealed to largely stem from the technical issue that sufficiently large chains at very high λ and ϕ reach the length of the simulation box and self-interact across the periodic boundary conditions. Very few defects were found. As expected, aspect ratio 1:5 did not yield any structures for the densities studied, except some chains at high λ. While the difference in rings can be explained away by steric exclusion, it is interesting to note the stark discrepancy in terms of defect structures which are - in principle - available in configuration space. This suggests that the secondary energy minimum of the dipole-dipole interaction is too shallow for both aspect ratio 1:3 and aspect ratio 1:5 platelets to form branched structures, barring a small fraction at very specific densities.

To summarize, the lack of available configurations strongly reduces the types and the quantity of clusters formed in the system. This is illustrated in Figure 4.12, where we compared a system of aspect ratio 1:3 at the λ and ϕ values with the highest percentage of defect formation to an equivalently dense system of dipolar spheres, which consists of a network of branched structures.

It is interesting to note that although both systems are initially quite similar in the isotropic low λ, low ϕ regime, the high λ and high ϕ limiting cases of the particles are a fully connected network with no overall orientational order, and, in case of platelets, stacks which cannot curve significantly due to their rigidity and therefore have greater local orientational order. We will explore the orientational attributes of the system microstructure in the following section.

4.2.1.b Orientational distribution of particles

Although we have now shown that platelets may lack positional ordering at densities where it would be expected from spheres, it would be remiss not to acknowledge that there could still be strong orientational correlations due the long-range dipolar interactions and, hypothetically, due to the particle anisometry, although this is not expected at the densities studied. In order to investigate these, we calculate the orientational pair correlations $g_2(r)$ as defined in similar works for platelets[141]. To extend this definition to otherwise isotropic spheres, the orientation of the magnetic dipole moment of the sphere is defined to be the director of the particle.

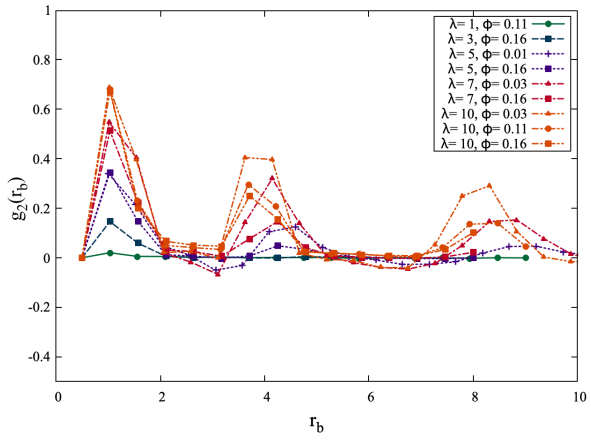

Figure 4.13: Pairwise orientational correlation of spheres, where the x-axis indicates the radial distance and the y-axis is the pairwise orientational correlation, ranging from perfectly aligned at 1 to negatively correlated at −0.5. We observe that the correlations peak at positions where the neighbors in an assembled structure would be located.

Examining the orientational correlations in the sphere system, shown in Figure 4.13, we find that $g_2(r)$ is almost identically 0 for $\lambda = 1$ (green) regardless of density, only slightly going above the x-axis for $r \approx 1$ where some pairs may have formed. This grows more pronounced for $\lambda = 3$ (dark blue), matching the expected start of pair formation. For $\lambda = 5$ (purple), we see periodic structure of peaks starting at the lowest density. At close ranges and multiples of slightly higher values than the diameter, there is a significant correlation which drops off in between. This pattern, which even shows a hint of negative correlation after the first peak, is most present for the lowest density $\phi = 0.01$. As the density increases, the correlation of close particles remains and the secondary remaining peaks flatten, with the curve at the highest density being reduced to two peaks at the nearest and second-nearest distances. Both the same pattern and trend are found in the $\lambda = 7$ curves, although there are two important differences. Firstly, the curve retains multiple

peaks even at higher densities. Secondly, these peaks are significantly higher- while the exact threshold for is debatable, overall correlation values > 0.3 are generally considered to be the criterion for significant ordering. Finally $\lambda = 10$ (orange) completes this pattern to a seemingly almost periodic ordering. As opposed to the clustering, the orientational correlations show a clear progression from disorder to order that increases with λ.

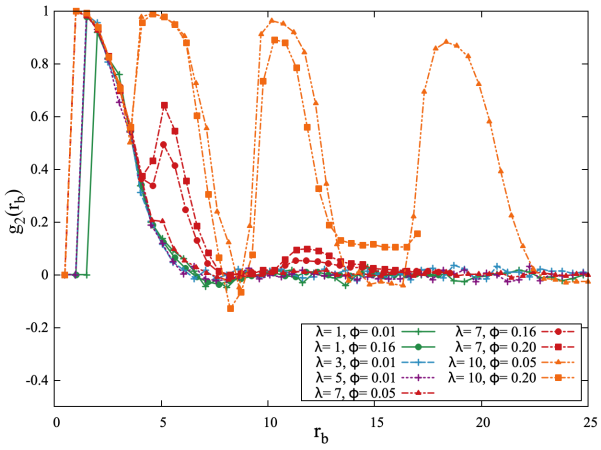

Figure 4.14: Pairwise orientational correlation of aspect ratio 1:3 platelets, where the x-axis indicates the radial distance and the y-axis is the pairwise orientational correlation. We note a much stricter alignment at close distances due to the steric repulsion, as well as more pronounced peaks for the higher λ systems.

The orientational correlations for platelets in Figure 4.14 show a very clear shape at close range: if we presume a particle at distance roughly the order of the platelet diameter, it must be highly aligned with the platelet in order to not violate the steric exclusion. This is enforced even for otherwise low-density systems: it should be noted that in this measure, as opposed to the previously shown radial distribution functions, the frequency of particles at a given distance is irrelevant. As opposed to the more diffuse peaks shown for spheres, platelets have a very clear pattern of alignment. For $\lambda < 7$ (green, blue, violet) this explains the gentle decorrelation we see: at close range, the particle shape enforces an ordering, while at greater distances the correlation drops to 0. This remains at low-density $\lambda = 7$, while for higher densities we see the formation of periodic correlations corresponding to the chain formation, which appears fairly pronounced considering the few chains in the system at this stage. Finally, for $\lambda = 10$, there is a clear periodicity to the correlations which seems to span the entire box, corresponding to the result that the particles are aligned (in long chains).

For aspect ratio $1:5$, we see the same shape for all densities and λ values as in the previous figure, albeit shifted and stretched to account for the greater aspect ratio of the platelets. This lends credence to the idea that these close-range orientational correlations are an effect strongly driven by shape. The figure also shows that there is no pre-nematic ordering affecting the platelets. In summary, the orientational correlations in the system seem to fall into two distinct categories: short-range correlations driven primarily by the shape for low λ, and periodically occurring correlations at larger distances in assembled chain structures driven by magnetic self-assembly.

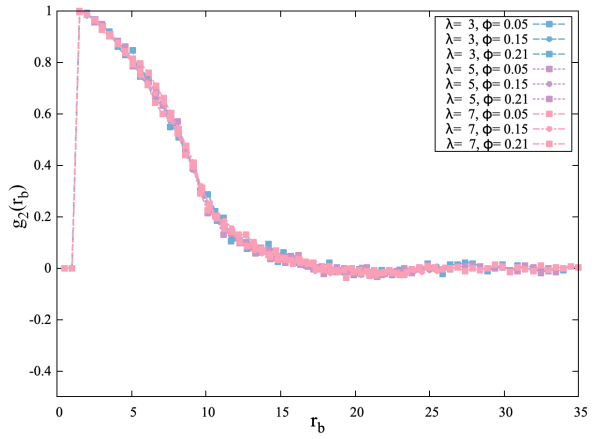

Figure 4.15: Pairwise orientational correlation of aspect ratio 1:5 platelets, where the x-axis indicates the radial distance and the y-axis is the pairwise orientational correlation. We see no orientational ordering at greater distances, confirming that we are both well below the magnetic assembly and the nematic thresholds.

Another possibility for characterizing the ordered structures formed in such systems are the Steinhardt order parameters[142]. These can shed light on the structure of the system as a whole, provided it shows a sufficiently high first peak of the radial distribution function from which to define nearest neighbors. We therefore only investigate systems with a clear first peak of the radial distribution function.

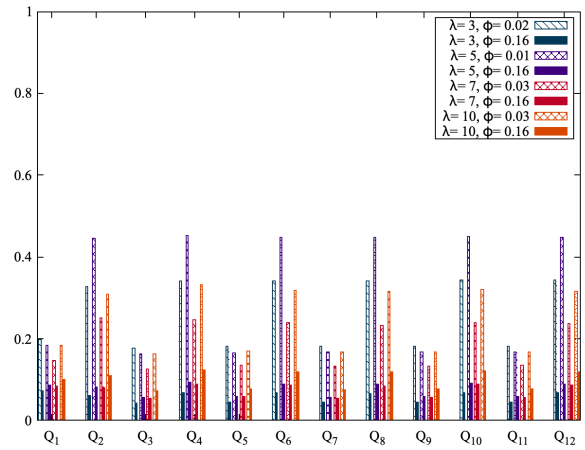

Figure 4.16: Steinhardt bond order parameters for spheres, Q_1 through Q_{12}. We see that the even Q values are significantly higher than the odds, especially for higher λ.

For spheres, the bond order parameters are relatively low and have the consistent trend of even-valued Q being higher than odd-valued Q, presumably due to the chain formation. The order parameters also decrease for higher values of the density, and the gap between even and odd parameters decreases. For $\lambda \leq 5$, high densities flatten all bond order parameters into essentially 0; for higher λ, some difference between even and odd values is preserved regardless of density.

In terms of bond order parameters, platelets show noticeably higher values for the even bond order parameters, but qualitatively follow the same trends as the higher λ spheres for lower values of λ or higher densities. At low densities and high values of λ, shown by the patterned orange and red bars, the values of the even bond order exceed those of spheres by far. In particular, the system

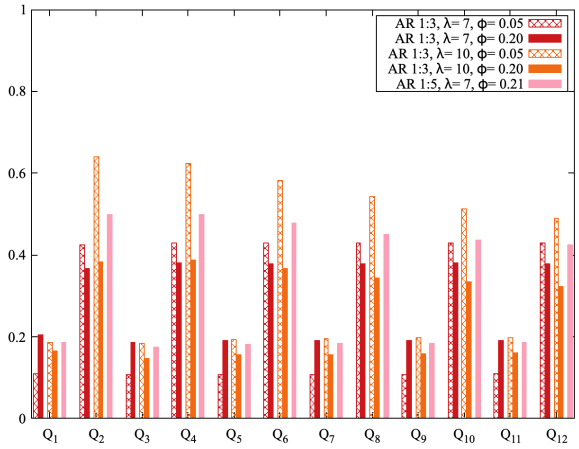

Figure 4.17: Steinhardt Bond order parameters for platelets of aspect ratio 1:3 (red and orange curves) and 1:5 (pink curve), Q_1 through Q_{12}. We see that the even Q values are significantly higher than the odds, especially for higher λ. Moreover, at high λ and low density these peaks easily surpass their equivalents in dipolar sphere systems.

of aspect ratio 1:3 platelets with $\lambda = 10$ has a peak at Q_2, although this should be considered critically since the system as at the boundary of what could be equilibrated due to the long chain formation. The only aspect ratio 1:5 platelet system for which bond order parameters could be defined, $\lambda = 7$ and $\phi = 0.20$, behaves similarly to the low-density variant of the $\lambda = 7$, aspect ratio 1:3 system. The conclusion of this section is that while predominance of chains in platelet systems does lend itself to some structuring, due to the homogeneity of the order parameters there is no overall lattice-type structure formed. Despite the different microstructures in terms of clustering, and the lower orientational correlation, spheres and platelets show surprising qualitative similarities where bond order parameters apply, presumably because the treatment of orientations in the definition of bond order parameters collapses the differences between chains which are bent (including network-like structures) and rigid, inflexible chains.

4.2.2 Initial Static Magnetic Susceptibility

What consequences do the differences in microstructure explored in the previous sections of this chapter have for the magnetic susceptibilities? Figure 4.18 shows the analytical expression for dipolar spheres for different values of λ as dashed lines, calculated using the chain approximation by Ivanov et al.[51] and the static initial magnetic susceptibilities calculated as in similar works[88] as solid lines with point represented by small spheres. Comparing these theoretical and analytical results for spheres, we see good agreement as expected. In contrast, the curves and values for platelets of various aspect ratios, shown with squares and stars, do not match the analytical approach. Two conjectures to explain this behavior spring to mind. Firstly, while the platelets do behave very differently than spheres as evidenced above, neither system shows a significant fraction of closed-flux structures (rings) which would decrease the susceptibility. It could be that the differences in microstructure are largely irrelevant, and that the qualitative shape of the curve that comes from mechanisms could still be the same, albeit shifted due to the difference in volume. Perhaps these

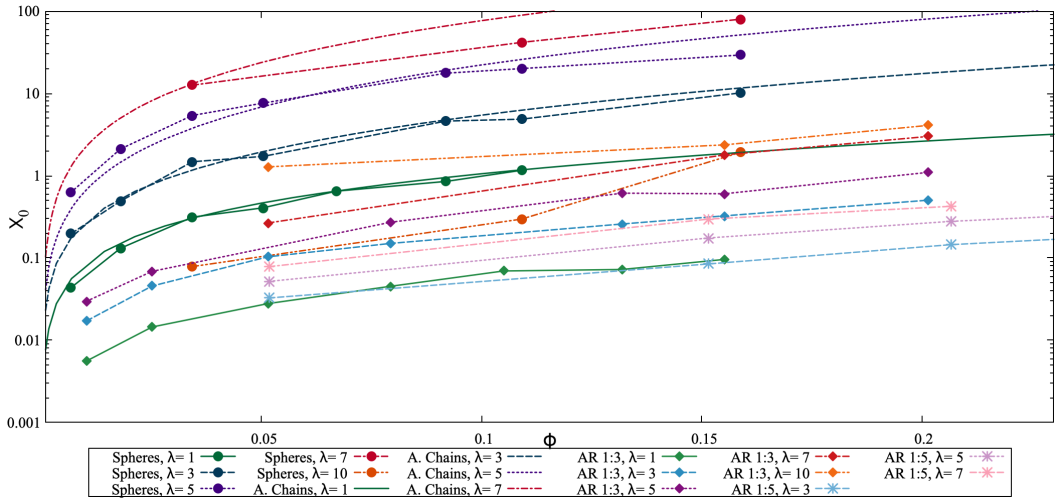

Figure 4.18: Initial magnetic susceptibilities (y-axis) at different volume fractions (x-axis): analytical approximations for spheres (dashed lines), simulation values for spheres (dark colors with circular points), simulation values for aspect ratio 1:3 platelets (medium colors, rhombi) and aspect ratio 1:5 platelets (light colors, stars). We see that platelets have lower magnetic susceptibilities that their spherical equivalents.

initial susceptibilities for platelets are qualitatively equivalent to spheres at a lower volume fraction. If there is a constant shift factor for each platelet aspect ratio, this would indicate that there is no significant impact of the shape on the static initial magnetic susceptibilities. Alternatively, the platelets might exhibit qualitatively different susceptibilities that will not fit to the equivalent curves for spheres.

To approach this distinction systematically, we begin by testing the basic assumption that, at least in the low-λ, low-ϕ system, the platelets should behave like dipolar spheres. As discussed in Section 2.1.4.a, the Langevin susceptibility of non-interacting dipolar spheres is given by $\chi_L = 8\lambda\phi$. Does the shape of the particles already affect their initial magnetic susceptibility even without interparticle interactions? Considering that at higher densities, platelets can form nematic and columnar phases, it is possible that there exists some orientational ordering of the platelets which in turn would result in an alignment of the dipole moments, departing from the Langevin curve. As this is a simulation work, we can simply remove magnetic interparticle interactions and check if the initial magnetic susceptibility of platelets still follows the Langevin law, *i.e.* if there are yet no nematic- or pre-nematic correlations affecting the susceptibility of platelets. Figure 4.19 tests this hypothesis by showing initial magnetic susceptibilities of systems without interparticle dipole-dipole interactions, rescaled by volume to correspond to the spherical case. We see that the magnetic susceptibilities fall exactly onto the Langevin curve. This suggests that there are no purely steric shape effects on the initial magnetic susceptibilities in the studied range of parameters, aside from the difference in density.

It also suggests that, although denser systems are more difficult to equilibrate, the rescaling

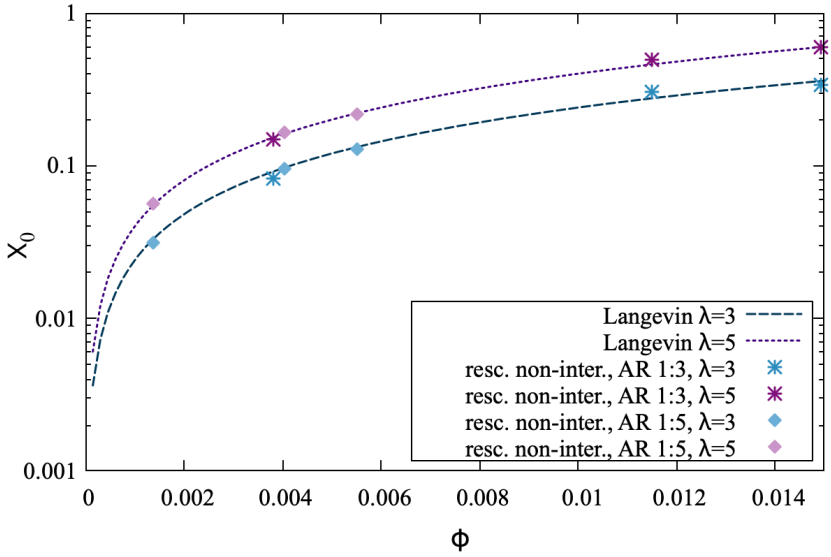

Figure 4.19: Langevin curves for two different values of λ, as well simulations results for non-interacting platelets at rescaled densities. If the densities are rescaled to match the equivalent sphere system, and magnetic interparticle interactions are disabled, platelets follow the Langevin law.

shown in this plot, specifically calculating the volume fraction based on the central magnetic sphere as opposed to the entire platelet, is a reasonable approach for low enough densities. We therefore select some of the susceptibilities shown in Figure 5.4 and rescale the densities in this manner, the result of which is depicted in Figure 4.20. In the top plot of this Figure, we see that for low values of $\lambda = 1$ and $\lambda = 3$, both aspect ratios of platelets fit the theoretical curves very well and essentially agree with the results for spheres, considering simulation accuracy. However, for $\lambda = 5$ at aspect ratio 1:5, and $\lambda = 7$ at aspect ratio 1:3 in the lower plot, the slope of the initial magnetic susceptibility appears steeper than that of spheres. The challenge in this context is that, as the density of the platelets needs to be so dramatically rescaled to be fitted to the curves, it is difficult to leave the region where dipolar sphere systems are still predominantely isolated, with few clusters. Therefore, the difference in microstructure is not as apparent as might be expected. While Figure 4.20 is difficult to interpret consistently across the scales, comparing to previous works on cubes[88] suggests that spheres agree very well with the analytical expression for magnetic susceptibilities at low ϕ, which for rescaled platelets hold for $\lambda = 1$ and $\lambda = 3$ but grows progressively worse for higher λ. This suggests that rescaling is an effective solution for low-density systems (which still exhibit a qualitatively microstructure to spheres) but becomes increasingly inaccurate once the platelets and spheres microstructures diverge.

Another option is to consider the physical underpinning of the issue in more detail. Firstly, we will drop the rescaling and use the Langevin function as calculated for platelets, $\chi_L^p = 8\lambda\phi \cdot (\frac{2}{3}\left(\frac{h}{d}\right)^2)$ (where $h = \sigma = 1$ to d is the aspect ratio). As previously explained, the current analytical model

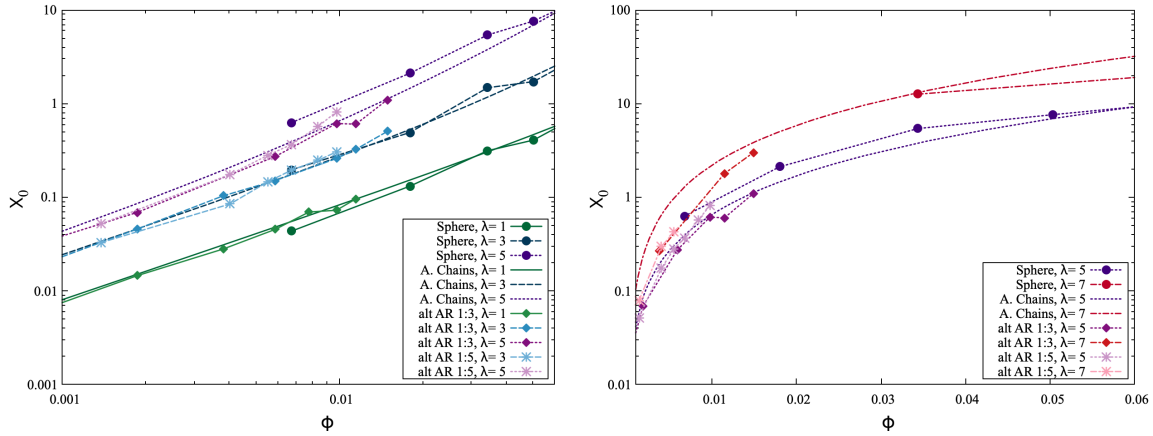

Figure 4.20: Initial susceptibilites of magnetic platelets and spheres, shown with a rescaled volume fraction for platelets. We see excellent agreement for the lower values of λ (blue and green curves, top plot), while at higher λ, the initial magnetic suscepibilities appear to follow a steeper progression than spheres and still appear lower than theoretical predictions.

uses the partition function of dipolar hard spheres. In Section 4.5, we will calculate the partition function for dipolar hard platelets, then insert this expression into the chain model (2.10), with χ_M being chosen as second-order modified mean-field theory. This model can be further refined by replacing K with another term expressing the interparticle correlations in chains, since K implicitly derived from the spherical shape[51]. One candidate would be $Q = \tanh \kappa\phi$, where κ is a system-specific constant that can be fitted (based on Onsager's approach)[143,144]. The value p is now the partition function for platelets, as opposed to that for dipolar hard spheres used in the original work. This should give a better agreement with the initial magnetic suscepibilities.

To test which theories are most applicable, we compare them to simulation data in Figure 4.21. This shows simulation data for aspect ratio 1:3 platelets (rhombi) and different values of λ (colors) with various theoretical models (lines). For $\lambda = 1$, we see agreement with the Langevin susceptibility χ_L. At $\lambda = 3$, second-order modified mean-field theory χ_{MMFT2} already gives better agreement, while for $\lambda = 5$ this new platelet chain-correction χ_c is most accurate. As is the case for spheres, higher λ yields more a complicated result: for $\lambda = 7$, the new χ_c does not fit the initial data point. This indicates a lack of agreement with the shape of the curve, which is not a promising sign. However, if we consider the difference in interparticle correlations on assembly and substitute Q for K, a variation written as χ_{cp}, we see excellent agreement. This means that we can very clearly link the effects our models describe (no correlations, few correlations, self-assembly and signficant self-assembly) both with the microstructure described so far, and the static susceptibilities. Unfortunately, this still falls short for the highest $\lambda = 10$, where χ_p does described the susceptibility in the highly clustered fluid, but fails for the lower density.

In Figure 4.22, we revisit this plot for aspect ratio 1:5 platelets and see the same trends in

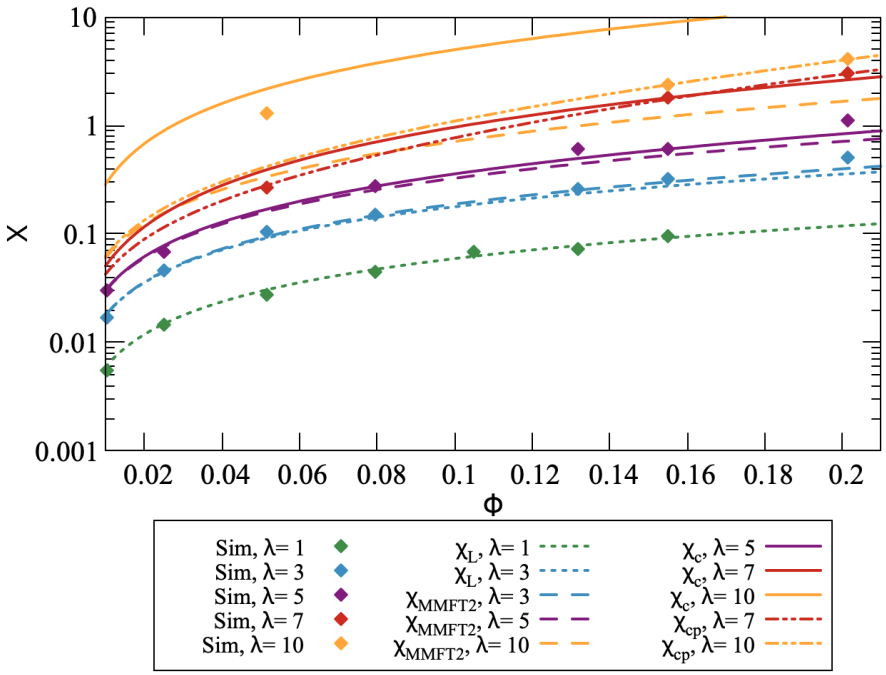

Figure 4.21: Initial static magnetic susceptibilities, with simulation values for aspect ratio 1:3 platelets (rhombi). Lines indicate analytical results. As λ increases, we see the best agreement shift from Langevin models to models that consider increasing correlations and self-assembly.

model agreement. We again see that χ_{MMFT2} is suitable for $\lambda = 3$, but interestingly enough, both $\lambda = 5$ and $\lambda = 7$ best agree with the modified correlations chain model χ_{cp}. Given the increasing anisotropy of the shape, it is perhaps not surprising that the interparticle correlations are even more different from the spherical case. It should be noted that the aspect ratio $1:5$ platelets include some very high density runs ($\phi > 0.3$), for which the values exceed the prediction limit- this was to be expected.

One advantage of this new theoretical model is its greater accuracy for intermediate and higher values of λ. Experimental results often observe some self-assembly, which indicates that λ should be considered in those ranges. A potential pitfall is that λ, as used herein, remains defined in a way that assumes one central dipole moment, which may not correspond to actual magnetic nanoplatelets where the magnetic moment is spread over the surface. If and to which extent the point-dipole λ corresponds to the closest-contact λ will be discussed in future sections. Since we still fundamentally assume that the overall platelet magnetic moment is dipolar, an adaption of λ would effectively amount to a platelet volume normalization.

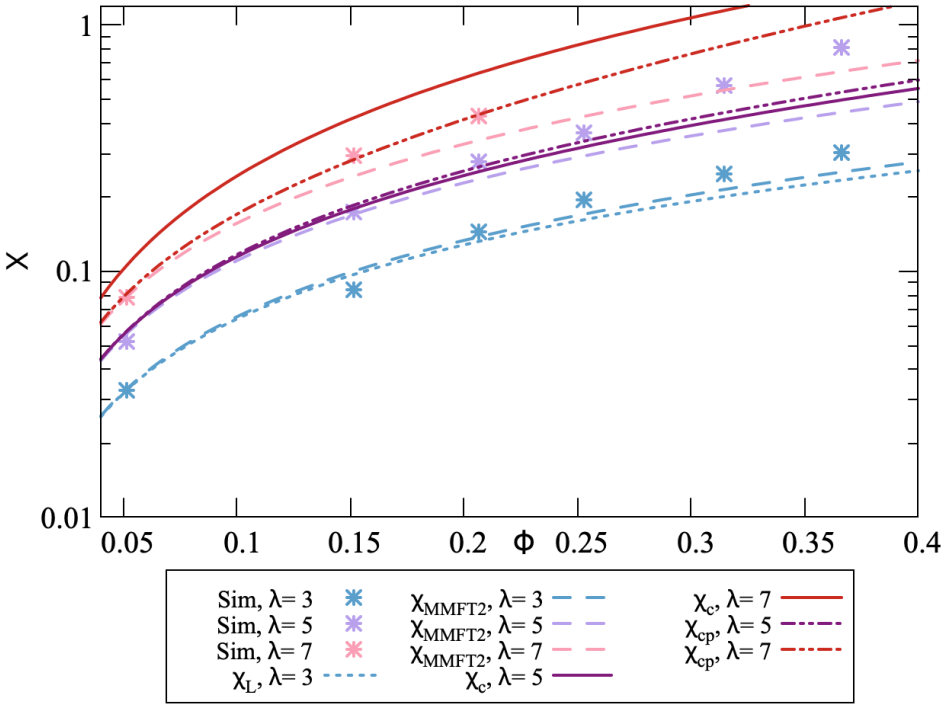

Figure 4.22: Initial static magnetic susceptibilities, with simulation values for aspect ratio 1:5 platelets (rhombi). Lines indicate analytical results. As in the 1:3 case, there is a clear progression of suitable models. However, the increased anisotropy means that the platelet corrected correlation coefficient is necessary from the onset of clustering.

4.2.2.a Initial Static Susceptibilities in Experiment

In experimental systems, the initial static magnetic susceptibilities can be calculated from the AC spectra. By using the high frequency peak to determine the Brownian relaxation time, the susceptibility can then be fitted via the following empirical formula from Rusanov et al.[145]:

$$\tau_{B,H} = \frac{\tau_{B,0}}{\sqrt{\left(1-\frac{\chi_{eff}}{3}\right)^2 + 0.076\zeta^2}} \tag{4.1}$$

These fittings were performed by our experimental collaborators, who provided the data shown as red crosses in Figure 4.23. The black line indicates a least-squares fit to the chain-modified platelet model using λ as a fitting parameter, with $h/d = 0.1$ chosen as an effective aspect ratio based on the experimental size distribution of the platelets. This is a remarkably good agreement, especially given that based on the simulation results, a value of $\lambda \approx 7.4$ would indicate a microstructure at coexistence of smaller clusters and singlets, which is supported by other experimental results (see Chapter 5). These results indicate that the current simulation model is best applied in certain limited regions of λ, ϕ phase space.

However, this agreement comes with a strong caveat: the mapping of experimental to simula-

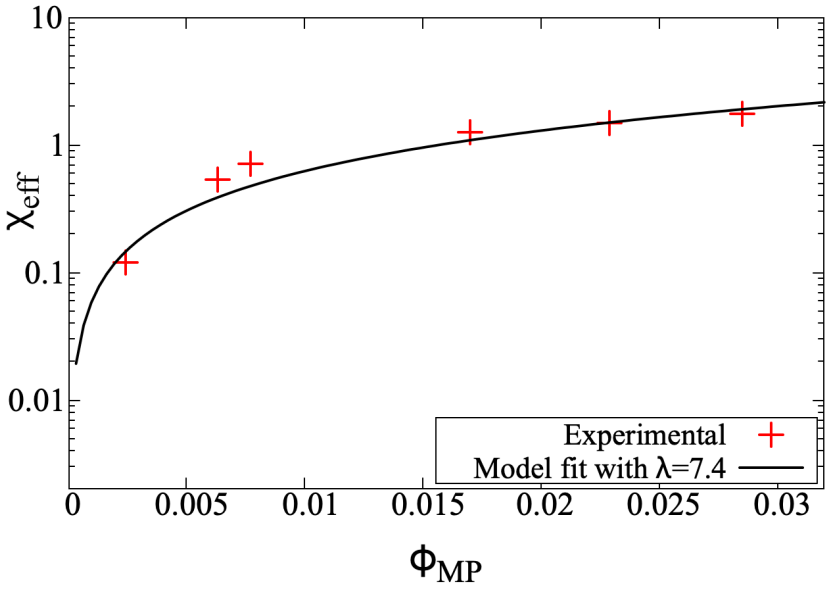

Figure 4.23: Comparison between the static magnetic susceptibilities of magnetic nanoplatelet suspensions as measured in experiment (red crosses) compared to the theoretical prediction of the chain platelet model (black line), where λ was used as a fit parameter. All experimental data was provided by Nádasi et al.[146] The results show good agreement, with the additional advantage that the microstructure indicated in simulation for $\lambda = 7$ conforms to experimental indications of the microstructure.

tion volume fractions does not have a conclusive, productive answer. As we saw in the previous Chapter, while a direct mapping from experiment to simulation parameters can yield some insight, but has its limits. In the case of this fit, the χ_L used as prefactor was the spherical-normalized version, which has been since pointed out as to be inconsistent. This is a valid critique, however the Rusanov formula is also based on mostly-spherical ferrofluids. Refitting with simulation-consistent values required two orders of magnitude λ, which is inconsistent with both theory and experimental measurements. Ultimately, the agreement of the microstructure as showing some self-assembly, the value of $\lambda = 7$ as an approximation is a first step for a phenomenological matching.

4.3 Conclusions

Although dipolar spheres and platelets might not be expected to differ strongly, we find significant differences in the microstructure of these systems, especially where self-assembly is concerned. Using a standard definition of the magnetic coupling constant poorly serves to predict magnetic platelet behavior, as a significantly higher value of the magnetic moment is required to elicit structure formation. For fixed values of λ and density ϕ, platelets self-assemble into fewer structures both quantitatively and qualitatively. When assembled, platelets favor chain structures with no rings and few defects. The cluster size distribution of platelets does not follow Wertheim exponen-

tial law. Despite the platelet aspect ratios being significantly below the threshold for nematic or pre-nematic ordering, once self-assembly begins, the platelet systems shows much higher short-range orientational correlations due to the particle shape. The resulting structures, especially for high λ, shows higher even-valued Steinhardt bond order parameters. The initial susceptibilities for platelets are significantly lower than those of spheres. Introducing volume corrections can solve this issue for lower λ, but higher λ values still do not agree with the rescaled spherical case. These discrepancies do not appear to be related to any pre-nematic ordering, as platelets without interparticle magnetic interactions follow the Langevin laws perfectly. Introducing an adapted version of the chain model for the initial static magnetic susceptibility results in a good fit for most values of λ. Overall, systems of magnetic dipolar platelets show large discrepancies in microstructure to the reference case of dipolar spheres, which also affects their magnetic susceptibilities and therefore must be taken into consideration.

4.4 Methods

4.4.1 Simulation Protocol

All of the simulation data in this work was obtained by carrying out Molecular Dynamics simulations using the software package ESPResSo 4.1.4[121]. As outlined in 2.1, we use a Langevin in the NVT ensemble with periodic boundary conditions. The simulation protocol was straightforward: given the fixed number of total particles $N = 1024$ and particle volume v determined by the choice of aspect ratio, the box length a was calculated to give a target volume fraction $\phi = \frac{N \cdot v}{a^3}$ (as $V = a^3$). Generally speaking, simulations were run for aspect ratios 1 : 1, 1 : 3 and 1 : 5, with ϕ ranging from 0.01 to 0.2 (with additional high density runs for Figure 4.20) and λ varying between 1 and 10. At the start of the simulations, the particles were placed randomly in the box, then separated to avoid steric overlaps. The time step was set to $\delta t = 0.01$. Simulations were warmed up for $1000\delta t$, then run for $10000 \cdot 100\delta t$. During the simulation run, checkpoints were taken every $10000\delta t$. Before the begin of statistical evaluation, the energy of the system was carefully checked in order to determine if thermodynamic equilibrium was reached. For simplicity's sake, the threshold of $10000\delta t$ was chosen as threshold after which checkpoints were considered equilibrated, since all low λ and almost all high λ were equilibrated. The $\lambda = 10$, aspect ratio 1:3 systems required higher, custom thresholds based on the energy. At high densities and magnetic moments, some planned systems could not be properly equilibrated (e.g. aspect ratio 1:5, $\lambda = 10$): therefore, they are mentioned as a qualitatively and not included in any statistics.

The dimensionless parameters and particle model were chosen as described in 2.1.

4.4.2 Analysis

All initial magnetic susceptibilities were calculated according to Ref.[88], with the analytical expression for chains derived in Ref.[51]. In cases where $Q = \tanh \kappa x$, the fitted values of κ were obtained via non-linear least-squares fit. The values obtained for aspect ratio 1:3 were $\kappa(\lambda = 7) = 5.5$, $\kappa(\lambda = 10) = 2.3$ and for aspect ratio 1:5, were $\kappa(\lambda = 7) = 19.5$ and $\kappa(\lambda = 10) = 1.4$. The same fitting algorithm was used to obtain the fit to experimental data. The orientational correlations were calculated as in Ref[141], albeit with the following distance and averaging protocol. First, each pair of particles' center-to-center distance is computed, then the orientational correlation is calculated and binned with a bin size of 0.5SU. Next, the average correlation per bin is calculated, and normalized by the number of particles at distance r_b. This means that the value of the curve at r_b reflects the average correlation of two particles at distances between $r_b - 0.5$ and r_b.

4.4.2.a Clustering, Defects

In the analysis of dipolar spheres or shapes such as cubes, a typical cutoff criterion for clustering would be a radial distance less or equal to 1.3σ (Ref. 140) or even 1.1σ (Ref. 88) and a negative dipolar interaction energy. However, using an isotropic cutoff on platelets would rule out any clustering with other than chains of platelets stacked along their height, since all platelet radii used are greater than 1.1. To solve this issue, we decouple the energy criterion from the distance criterion: the interaction energy is calculated as seen in Equation 2.17, but the minimum distance between two platelets for the purpose of the cutoff is redefined as the minimum distance between any pair of interaction sites on the two platelets. This means that for a hypothetical pair of platelets in the same plane, with a center to center distance of $2r$, the minimum distance is now counted as σ (*e.g.* the distance between the two outermost interaction sites). This solution tackles the platelet shape issue, but leads to the unfortunate side effect that in low-λ systems, non-interacting particles that will in a statistically significant number of cases also have favorable dipole alignments are counted as clusters due to the extended cutoff. This was prevented by adding an energy criterion, $U_{dd} \leq -0.5$ with adjusted distance. For the comparison figures shown of sphere assembly, the same criteria were applied (albeit with the distance definition coinciding with literature due to spheres only having one interaction site).

Since defects in dipolar systems have already been studied intensively, we simplify the categorization used in Ref. 137 and only consider the number of "bonds" each particle has, collapsing defects into a single category due to their rarity in platelet systems. This leads us to the following cases and definitions (for clusters with $n \geq 2$ particles):

1. a cluster containing at least one particle with more than 2 bonds is a defect cluster ("branched structure")

2. a cluster where each particle has exactly two bonds is a ring

3. any remaining cluster is a chain

Some high-λ systems of platelets appear to form rings. Closer investigation showed that these appear to be simulation artefacts, either resulting from the definition listed below which allows 3-particle "clusters" to count as rings despite the fact that in the platelet case, the magnetic flux is typically not closed, or resulting from a technical problem with chains that span the length of the box being counted as rings due to the periodic boundary conditions. Since the former is argueably still a valid ring, these structures were retained as such. Most of the simulation runs that showed the latter type of ring were cut from the quantitative results due to equilibration concerns.

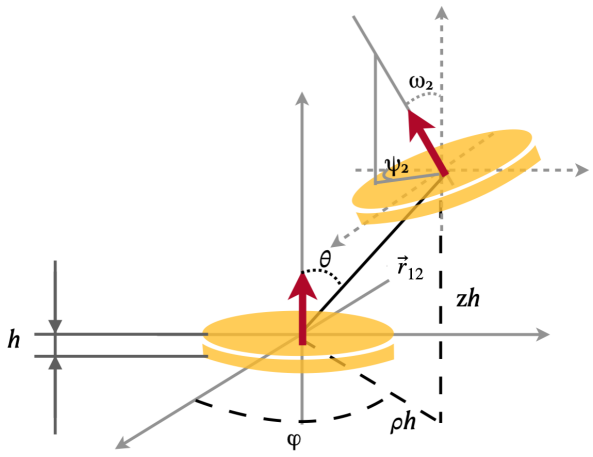

Figure 4.24: Sketch of two magnetic platelets with central dipoles, illustrating the naming convention of the angles used in the derivation below.

4.5 Appendix: The Partition Function of Dipolar Hard Platelets

This section details the derivation of the mathematical expression of the partition function for dipolar hard platelets. This calculation was originally carried out by A.O. Ivanov, to whom the primary credit for the intellectual work of this supplementary section belongs.

As laid out in Chapter 2.1, the partition function q_0 of particles interacting via a steric central particle-particle interaction U_s and a dipolar interaction U_{dip} can be written as:

$$q_0 = \frac{1}{v}\int d\vec{r}_{12}\int d\vec{\Omega}_2 \exp\{[-\beta U_s(12) - \beta U_{dip}(12)]\} \tag{4.2}$$

where v is the platelet volume, $\beta = 1/(k_B T)$ and the subscripts 1 and 2 refer to the two interacting platelets. Without loss of generality, we will assume that platelet 1 is fixed relative to platelet 2, and that platelet 1 is in the origin. Then the integration is carried out over the volume which the centre of the second platelet can move in, with the volume element $d\vec{r}_{12}$, and over the all possible orientations of the dipole moment of the second platelet $d\vec{\Omega}_2$. Both platelets have the height h; we will use cylindrical coordinates to describe their distance and relative orientations. We also assume that we can measure all the distances in the units of h, so that the actual dimensions of the platelet become irrelevant and only the aspect ratio h/d matters. The key task of this section is to calculate the dipolar interaction term, which is:

$$-\beta U_{dip}(12) = \lambda\left(\frac{h}{r_{12}}\right)^3 [3(\hat{\mu}_1, \hat{r}_{12})(\hat{\mu}_2, \hat{r}_{12}) - (\hat{\mu}_1, \hat{\mu}_2)] \tag{4.3}$$

where we used $\lambda = \mu_0 m^2/(4\pi h^3 k_B T)$ to express the dipolar interaction strength in a compact way. The remaining vectors in the bracketed term are now unit vectors, as indicated by their stylish hats. This is where the cylindrical coordinate notation introduced in Figure 4.24 come into play: without loss of generality, we will assume that platelet 1 is the platelet positioned in the

origin, with the dipole moment pointed along the z axis. From the sketch, we can see that the angles $(\hat{\mu}_1, \hat{r}_{12}) = \cos\theta$ and $(\hat{\mu}_1, \hat{\mu}_2) = \cos\omega_2$. For the remaining term $(\hat{\mu}_2, \hat{r}_{12})$, we have both the azimuthal term $\cos\theta\cos\omega_2$, as well as the radial term which is composed of the relative rotation of platelet 2 in its radial plane, and the projection of the azimuth components. We can then rewrite and simplify Eq. 4.5 as:

$$
\begin{aligned}
&= \lambda\left(\frac{h}{r_{12}}\right)^3 \left[3\cos\theta\left(\sin\theta\sin\omega_2\cos(\psi_2-\varphi)+\cos\theta\cos\omega_2\right)-\cos\omega_2\right] \\
&= \lambda\left(\frac{h}{r_{12}}\right)^3 \left[3\cos\theta\sin\theta\sin\omega_2\cos(\psi_2-\varphi)+\cos\omega_2\left(3\cos^2\theta-1\right)\right]
\end{aligned}
$$

Now that the orientations have been dealt with, we will introduce the expression $r_{12}^2 = h^2\rho^2 + h^2(1+z)^2$, with $0 \le \rho \le 1$ and $0 \le z \le 1$ for the separation between platelet centers, where $|\vec{r}_{12}| = r_{12}$. The goal is to use these new parameters ρ and z as perturbation variables. We assume that these two variables ρ and z are dimensionless parameters that characterise small deviations of the distance between the centres of the platelets from the effective height h due to thermal fluctuations. This h is also the unit of all lengths. Assuming that rho and z are zero for any terms of order higher than 3, we can then express:

$$
\left(\frac{h}{r_{12}}\right)^3 = \frac{h^3}{[h^2\rho^2+h^2(1+z)^2]^{3/2}} = \frac{1}{[\rho^2+(1+z)^2]^{3/2}} = \left(1+2z+z^2+\rho^2\right)^{-3/2}
$$

And using Fig. 4.24, we can also simplify:

$$
\begin{aligned}
\cos\theta = \frac{1+z}{[\rho^2+(1+z)^2]^{1/2}} = \frac{1+z}{[1+2z+z^2+\rho^2]^{1/2}} &\approx (1+z)\left[1-z+z^2-\frac{1}{2}\rho^2\right] \\
&= 1+z-z-z^2+z^2-\frac{1}{2}\rho^2 \approx 1-\frac{1}{2}\rho^2
\end{aligned}
$$

and:

$$
\sin\theta = \frac{\rho}{[\rho^2+(1+z)^2]^{1/2}} \approx \rho\left(1-z+z^2-\frac{1}{2}\rho^2\right) \approx \rho(1-z)
$$

and then revisit:

$$\left(\frac{h}{r_{12}}\right)^3 \approx 1-\frac{3}{2}\left(2z+z^2+\rho^2\right)+\frac{15}{8}\left(2z+z^2+\rho^2\right)^2+\ldots \approx 1-3z-\frac{3}{2}z^2-\frac{3}{2}\rho^2+\frac{15}{2}z^2 = \\ = 1-3z+6z^2-\frac{3}{2}\rho^2$$

Inserting these results into our expression for the dipole-dipole potential gives:

$$\begin{aligned}
-\beta U_d(12) &= \lambda\left(1-3z+6z^2-\frac{3}{2}\rho^2\right)\cdot \\
&\quad\left[\cos\omega_2\left(3\left[1-\frac{1}{2}\rho^2\right]^2-1\right)+3\sin\omega_2\cos(\psi_2-\varphi)\rho\,(1-z)\left(1-\frac{1}{2}\rho^2\right)\right] \\
&= \lambda\left(1-3z+6z^2-\frac{3}{2}\rho^2\right)\left[\cos\omega_2\left(3\left(1-\rho^2\right)-1\right)+3\sin\omega_2\cos(\psi_2-\varphi)\rho\,(1-z)\right] \\
&= \lambda\left(1-3z+6z^2-\frac{3}{2}\rho^2\right)\left[\left(1-\frac{\omega_2^2}{2}\right)\left(2-3\rho^2\right)+3\omega_2\rho\cos(\psi_2-\varphi)\right] \\
&= \lambda\left(1-3z+6z^2-\frac{3}{2}\rho^2\right)\cdot\left[2-\omega_2^2-3\rho^2+3\omega_2\rho\cos(\psi_2-\varphi)\right] \\
&= \lambda\left[2-\omega_2^2-6\rho^2+3\omega_2\rho\cos(\psi_2-\varphi)-6z\right] = \lambda\left[2-6z-\omega_2^2-6\rho^2+3\omega_2\rho\cos(\psi_2-\varphi)\right]
\end{aligned}$$

We can now insert these simplifications in the expression for the platelet partition function. To calculate the integral, we also note $d\vec{\Omega}_2 = (4\pi)^{-1}\sin\omega_2 d\omega_2 d\psi_2$ and $d\vec{r}_{12} = 2\pi h^3\rho d\rho dz$:

$$\begin{aligned}
q_0 &= \frac{2\pi}{\nu}\int_0^1\rho d\rho\int_0^1 h^3 dz\int_0^{2\pi}\frac{d\psi}{2\pi}\int_0^\infty\frac{\omega_2 d\omega_2}{2}\exp\{2\lambda\}\exp\{-6\lambda z\}\cdot \\
&\qquad\exp\left\{-\lambda\omega_2^2\right\}\exp\left\{-6\lambda\rho^2\right\}\exp\{-3\lambda\omega_2\rho\cos\psi\} \\
&= \frac{1}{\nu}\exp\{2\lambda\}h^3\frac{2\pi}{6\lambda}\int_0^1\rho d\rho\int_0^\infty\frac{\omega_2 d\omega_2}{2}\exp\left\{-\lambda\omega_2^2-6\lambda\rho^2\right\}\mathrm{I}_0(3\lambda\omega_2\rho) = \\
&= 2\pi\frac{h^3\exp\{2\lambda\}}{6\lambda\nu}\int_0^1\rho d\rho\frac{1}{2}\exp\left\{-6\lambda\rho^2\right\}\frac{\exp\left\{\frac{9\lambda^2\rho^2}{4\lambda}\right\}}{2\lambda} \\
&= \frac{h^3\exp\{2\lambda\}2\pi}{24\lambda^2\nu}\int_0^1\rho d\rho\exp\left\{-6\lambda\rho^2+\frac{9}{4}\lambda\rho^2\right\} = \\
&= \frac{h^3\exp\{2\lambda\}2\pi}{24\lambda^2\nu}\int_0^1\rho d\rho\exp\left\{-15/4\lambda\rho^2\right\} \\
&= \frac{h^3\exp\{2\lambda\}}{2}\pi 24\lambda^2\nu\frac{1}{2}\frac{4}{15\lambda} = \frac{h^3\pi\exp\{2\lambda\}}{24\lambda^2\nu 3\lambda} = \frac{2}{15}\left(\frac{h}{d}\right)^2\frac{\exp\{2\lambda\}}{3\lambda^3}
\end{aligned}$$

where the integral over ω_2 was simplified using a zero-order modified Bessel function of the first kind, $I_0(\cdot)$. This derivation used an approach similar to previous work[51]. The expression obtained here for the partition function has the main leading term $\exp(2\lambda)/3\lambda^3$ (see[147]), which is the same as for spherical particles. The only difference in this approximation is hidden in the prefactor, which is proportional to the aspect ratio of the platelet.

5 - Dynamic Susceptibility

This chapter explores the influence of microstructure on the susceptibility spectra of magnetic nanoplatelet suspensions. We select a dipolar coupling constant which both corresponds to experiment and samples the coexistence of singlets and clusters. This allows us to traverse the microstructural phase diagram by varying the volume fraction. We begin by characterizing the static properties, including the magnetization and initial static magnetic susceptibility. Then, we study the dynamic magnetic susceptibility $\chi(\omega)$, in both zero field and with a static applied field, to correspond to experiments in which bias fields are utilized. In the absence of an external field, we can see distinct bands of $\chi(\omega)$ which can be identified with individual particles and other bands which can be identified with small and medium clusters. An applied external field increases the aggregation, and leads to the formation of longer chains, with slower relaxation. Simultaneously, the individual platelet frequency increases due to the interaction with the field in field direction. While we see the same underlying mechanisms as found to affect the dynamic susceptibilities of dipolar hard spheres, the platelet microstructure leads to dramatic increases in the reorientational relaxation times. To conclude, we compare our results to experimental work and posit an explanation for one of their more surprising findings.

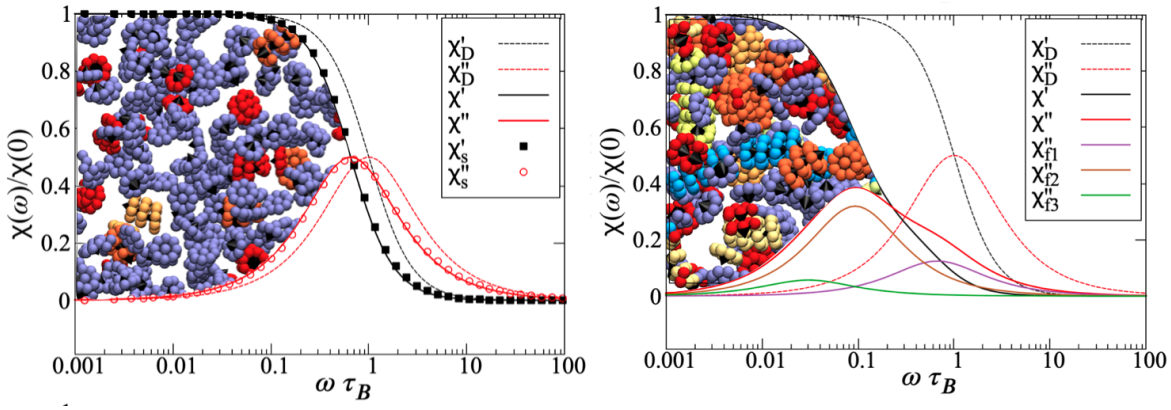

Figure 5.1: The dynamic magnetic susceptibility of a low density (left) and high density (right) suspension of magnetic nanoplatelets. The subscript D indicates Debye, the other curves are simulation results. Simulation snapshots show the corresponding microstructure, with bright smscolors indicating self-assembly.

The material in this chapter is also contained in:

[4] Rosenberg M., S. Kantorovich, P. J. Camp "*Structure and dynamics in suspensions of magnetic platelets*", in preparation

5.1 Introduction

As discussed in previous chapters, colloidal suspensions with well-defined, strong responses to external magnetic fields are of interest for both biomedical and industrial applications[80,148–151]. With sufficiently fine control by uniform or gradient magnetic fields, these suspensions are functional materials.

Recent experimental findings suggest pronounced differences in the dynamic magnetic susceptibility $\chi(\omega)$ of magnetic platelet suspensions[152] as opposed to the classical case of spherical colloids. This property describes the response of the magnetization to an AC magnetic field. Each of these spectra consists of a real-valued, in-phase component and an imaginary-valued out-of-phase component. This property in particular would be of great interest for magnetic hyperthermia applications[52]. In the experiments by Küster et al.[152], the out-of-phase component of dispersions in the isotropic phase was shown to exhibit three modes at low concentrations, with the lowest and highest frequency peaks separated by three orders of magnitude. The authors attribute the low-frequency modes to collective relaxation, and point out that some of the longer relaxation times could be attributed to the effects of polydispersity. In our joint paper referenced in the previous chapter, they showed that varying the surfactant and/or the magnetic nanoparticle concentration can shift or suppress the low- and medium-frequency modes, reinforcing the idea of a link between these modes and platelet aggregation.

In the case of ferrofluids with spherical colloidal nanoparticles, the dynamic magnetic susceptibility can be described theoretically via modified mean-field theory for weakly interacting particles, and computed in simulation via the fluctuation-dissipation theorem[153,154]. In these investigations, the strength of the magnetic particle interactions was shown to play a key role. If it is sufficiently low, there is a single characteristic timescale corresponding to the Brownian rotation time of the particles, which gives rise to a single peak at the corresponding frequency of the out-of-phase component. As the interactions increase, the interparticle correlations cause an increase in the rotation time and a decrease in the peak height.

In ferrofluids with strong magnetic intraparticle interactions, the changes in microstructure induced by the self-assembly of the particles have been shown to affect the dynamic susceptibility[155]. In particular, features associated with long timescales associated with cluster relaxation, and features associated with the relaxation of single particles within clusters. The inclusion of a static uniform magnetic field, as in the experimental setup of *e.g.*[152], can also shift the peak of the dynamic susceptibility to higher frequencies. This is due to the field serving as an additional restoring force on the orientation of particles, which accelerates the rate of particle relaxation[156].

This chapter explores the effects of the platelet shape on the dynamic magnetic susceptibility, and concludes by putting forward an explanation for the atypically broad peak of the dynamic susceptibility found in experiment.

5.2 Results

5.2.1 Static Properties

The center to center radial distribution function $g(r)$ of the magnetic nanoplatelet suspensions at varying density ϕ is shown in Figure 5.2. Even at lower concentrations, such as $\phi = 0.05$, some self-assembly is shown by the nearest-neighbor peak. While the minimum of the WCA interaction is located at $r \simeq 1.12\sigma$, the lowest-energy separation with nose-to-tail dipolar interactions minimizes

$$\frac{U_{\mathrm{WCA}}(r)}{k_{\mathrm{B}}T} - 2\lambda\left(\frac{\sigma}{r}\right)^3,$$

and with $\lambda = 7$, this is $r \simeq 0.96\sigma$.

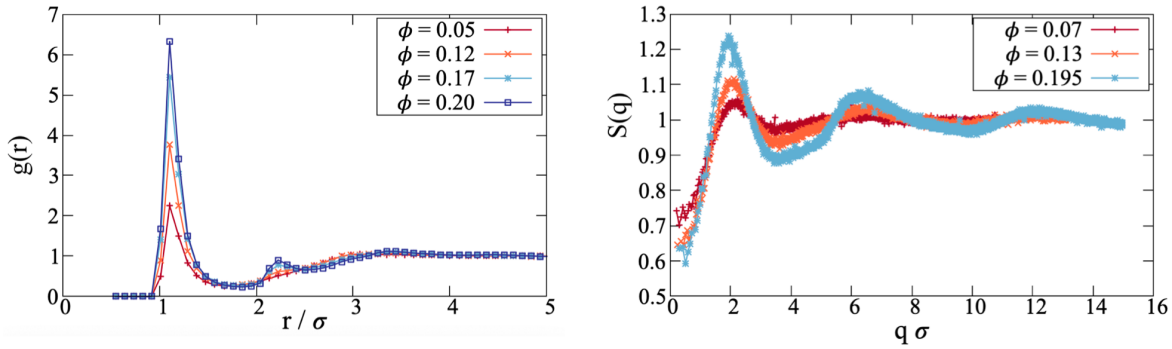

Figure 5.2: Center to center radial distribution function $g(r)$ (top) and structure factor S(q) (bottom) for different volume fractions ϕ of platelets in the absence of an external field. As the volume fraction grows from $\phi = 0.05$ to $\phi = 0.2$, we see gradually increasing self-assembly as evidenced by the formation and growth of multiple nearest-neighbor peaks.

The peak height increases with growing concentration, with an emerging second peak indicating the formation of chains. The distance at which the radial distribution function levels out, initially $r = 3$, is equal to one platelet diameter, also shifts to higher values, hinting at a future third peak. Both of these processes are monotonic with increasing volume fraction. This agrees with previous results on platelets[157], and indicates that we have correctly chosen a coexistence region, where the platelets are initially predominantly dispersed, then self-assemble into increasingly large structures.

The structure factor $S(q)$ also reflects growing structural inhomogeneity arising from cluster formation. At low q, the values indicate that the isothermal compressibility (due to magnetic and steric interactions) decreases with increased concentration, as expected. We can again observe the platelets' shape affecting the structure, in that the local minima in $S(q)$ are flatter and broader than those for highly clustered dipolar-sphere fluids, since the distance of closest approach depends on the mutual orientations of the platelets. The primary peak at $q\sigma \simeq 2$ indicates structuring

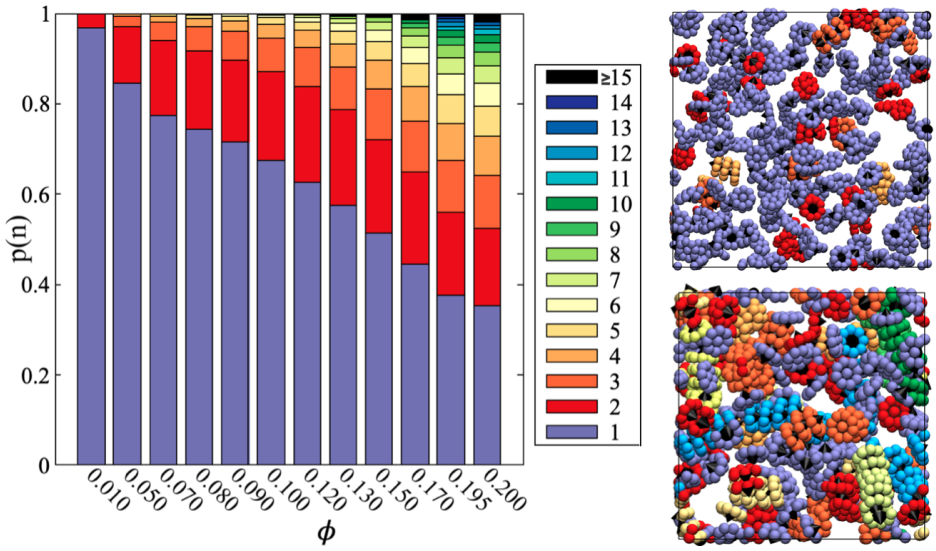

Figure 5.3: Left: Percentage of particles in a cluster of size n for increasing density, including n=1 singlets in purple. Due to their scarcity, assemblies of $n \geq 15$ are condensed into a single color. Right: Simulation snapshots corresponding to $\phi = 0.07$ (top) and $\phi = 0.195$ (bottom). The coloring of the platelets corresponds to the number of particles in each cluster. The black arrows on the surface indicate the orientation of the particles' dipole moment, with the arrow being positioned on the "head" side. If a platelet does not appear to have black dipole moment arrow, this means that the visible side is the "tail" side.

on the length scale of $r \simeq 2\pi/q = 3\sigma$, which corresponds to the range over which $g(r)$ deviates significantly from 1. This corresponds to a 'pre-peak', indicating intermediate-range order over that length scale. The next peak at $q\sigma \simeq 6$ corresponds to the nearest-neighbor separation around $r \simeq \sigma$. The second and third peaks show a pronounced asymmetry, which is characteristic of chain-like correlations between dipoles[158,159], or in this case, columnar correlations between platelets.

These ideas about the formation, size and quantity of self-assembly in the system are pursued in Figure 5.3, which delivers both a visual representation of the simulation particles (right) as well as a quantitative summary of the percentage of clustered particles (left). We see the fraction of clustered particles (all but purple) grows from ca. 15 % to ca. 65 % as the volume fraction ϕ increases to $\phi = 0.2$. It is interesting to note that the dimer fraction (red) stays roughly constant at 17-20 % for volume fractions $\phi > 0.05$, peaking at $\phi = 0.13$. Similar behavior is seen for other small-cluster fractions, like trimers and tetramers. Essentially, as ϕ is increased, the fraction of monomers decreases, the fractions of particles in medium-sized clusters remain roughly constant, and the fractions of particles in large clusters increase. An important caveat is that, as in the previous chapter, this clustering algorithm is predominantly based on a distance criterion, which means that the distinction between clusters becomes blurred at high concentrations.

The simulation snapshots in Figure 5.3 illustrate the amount of aggregation, with different colors representing the size of the cluster (if applicable) which the platelets are contained in. At

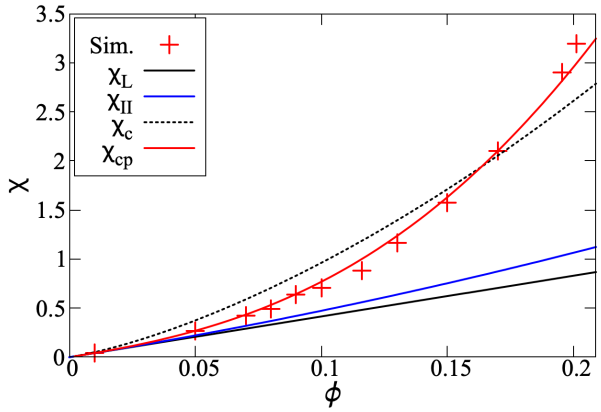

Figure 5.4: The initial static magnetic susceptibility calculated from simulations (red crosses), compared to different theoretical models: the Langevin susceptibility (black), second-order modified mean-field theory (blue), the chain-model with the platelet partition function term (black dashed) and the chain-model with a platelet partition function and an adjusted correlation coefficient (red). We see the best agreement for the latter theory, suggesting that the altered interparticle correlations are indeed key to understanding platelet susceptibility.

the lower density shown, $\phi = 0.070$, most of the platelets are monomers (purple). The average separation between neighboring particles is $\overline{r} = \sqrt[3]{V/N} \simeq 4.66\sigma$, which is larger than the platelet diameter, and the particles are not oriented in suitable ways to form clusters. At $\phi = 0.195$, $\overline{r} \simeq 3.31\sigma$, the self-assembled structures formed by platelets are mostly chains, with few branched structures. Since this has been discussed in detail in previous work[157], we will only note due to the predominance of chains, and due to the shape of the platelets constraining their positions in the head-to-tail dipole alignment, the larger platelet assemblies do not allow for much intracluster particle movement. This means that there are no significant intracluster fluctuations, which is important to remember when interpreting the dynamic magnetic susceptibility. It should also be noted that while $\phi = 0.200$ is around the largest feasible concentration where there are distinct columns, simulations of monodisperse steric platelets do not exhibit a nematic phase at this aspect ratio[141], and no signs of nematic ordering were observed in the present case.

The initial static magnetic susceptibilities are shown in Figure 5.4. Due to the chosen high value of $\lambda = 7$, we again see that Langevin (black) and second-order modified mean-field theory (blue) are insufficient to capture the effects of self-assembly. As in the previous chapter, using the chain-correction model with the platelet partition function term yields significantly better agreement. However, for a true description of the susceptibility, we must account for the different interparticle correlations, as shown with the adjusted correlation coefficient $Q = \tanh \kappa\phi$. In this case, $\kappa = 5$. Since much of the findings were discussed in the previous chapter, we only note that the inclusion of more densities highlights the importance of the correlation term. In this Figure, χ_c denotes the chain model for platelets (with no modification to K), shown as gray dots, and $\chi_c p$ indicates the modified version including Q, shown as a red line. The latter clearly has much better agreement.

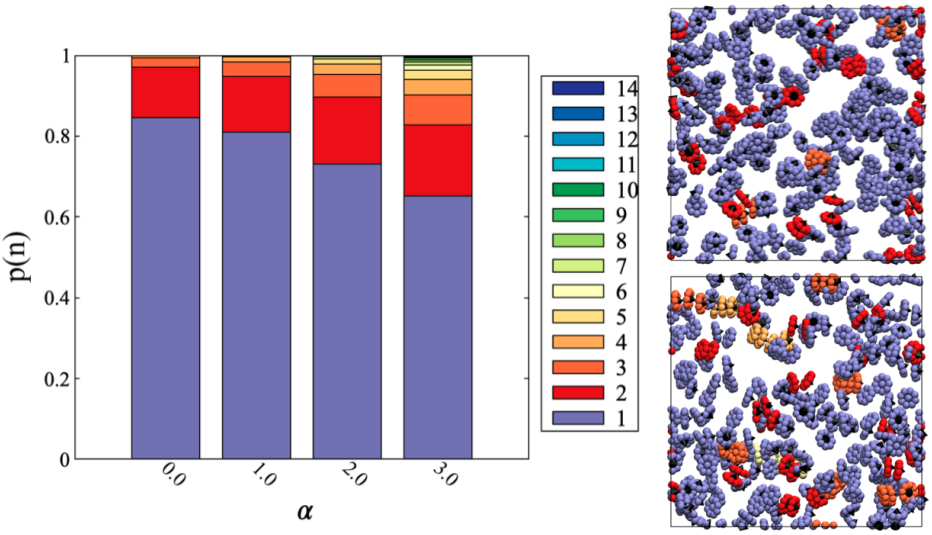

Figure 5.5: Left: bars showing percentage of clustered particles for $\phi = 0.05$, $\alpha = 0..3$. Not only does the clustering increase in absolute terms, the clusters also grow much larger (especially at lower densities). Right: Snapshots of the $\phi = 0.05$ system at $\alpha = 1$ (top) and $\alpha = 3$ (bottom), where H is parallel to the page.

Aside from the options of increasing the density or dipolar coupling constant, another way to alter the self-assembly is to apply an external magnetic field to the suspension. This is expected to increase aggregation. The strength of this field relative to the dipolar coupling constant is characterized by the Langevin parameter (see Section 2.1.4.a). The effect of the applied field on the self-assembly is shown in Figure 5.5.

As even low fields significantly increase the clustering, these studies were carried out at lower values of the density $\phi = 0.001$ to $\phi = 0.05$. Examining the breakdown into different cluster sizes in the histogram, we see that the clustering increases strongly with field application. Moreover, comparing to Figure 5.3, while the percentage of clustered particles at $\phi = 0.05$ and $\alpha = 3$ is close to $\phi = 0.1$, the size distribution has changed: for $\phi = 0.1, \alpha = 0$, only $\approx 2.4\%$ of particles are in clusters with size $n > 4$, and $p(n)$ roughly halves with each increasing n (up to a maximum size of 10 with $p(10) = 0.002\%$), whereas for $\phi = 0.05, \alpha = 3$, the fraction of particles in clusters with size $n > 4$ is 6.1%, (up to a maximum size of 14 with $p(14) = 0.04\%$). It appears that the application of an external field favors the formation of longer chains at lower volume fractions, than would be the case in absence of a field. This is also made plausible by the simulation snapshots: in the field-free case (Figure 5.3 right), we observe that the short chains are oriented randomly, while the presence of an external field aligns them in a favorable configuration for self-assembly (Figure 5.5, right).

In Figure 5.6, we can see the magnetization of the system depicted as points for two low densities, up the the maximum of $\phi = 0.05$. The line indicates the Langevin (black) prediction for the system. For the lower values of ϕ, we see almost perfect agreement with the Langevin case,

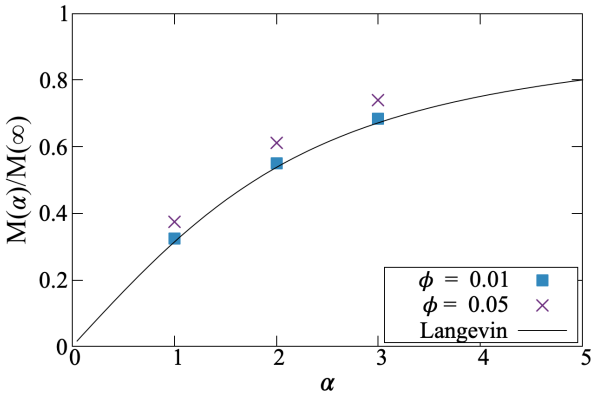

Figure 5.6: At sufficiently low densities, the magnetizations follow the Langevin law. But once the particles are dense enough to begin clustering, they approach the higher values.

suggesting that the particles in this system have very weak interactions. These systems will be useful in differentiating between effects induced purely by the external magnetic field, as compared to the combination of self-assembly and the magnetic field. At the higher density, these values increase markedly due to the strong correlations.

As the additional field breaks the symmetry of the system, we split the structure factor into two components, one for the wave vectors parallel ($q_{\parallel}$) and one perpendicular ($q_{\perp}$) to the field H[160–163]. These were studied in detail for magnetized ferrofluids containing spherical particles[147,164–168].

Such structure factors are shown for platelet systems in Figure 5.7, for $\phi = 0.05$. Perpendicular to the field, we see the growing first peak, indicating some increasing clustering. Since we expect chains to align with the field, it makes sense that no long-range ordering appears. The peak also shifts to lower $q_{\perp}$ with increasing field strength. This is consistent with alignment of the platelets in the field direction, and that any side-by-side correlations occur over distances comparable to the platelet diameter $r \simeq 3\sigma$, giving rise to the peak at $q_{\perp}\sigma \simeq 2$. With increasing field strength, the columns repel each other more due to the side-by-side parallel alignment of the dipoles, and this explains the shift to smaller values of $q_{\perp}$. For the structure factor parallel to the field, there is a greater difference between the field-strengths: for $H = 1$, there is no discernable structure, while the two higher values of H seem to show a clear periodicity of peaks that would indicate chain formation, with peaks near 2π and 4π. The peak heights grow with increasing field strength, indicating an increase in clustering. This would support that the external field is inducing self-assembly into long chains which are closely aligned with the field.

To recapitulate this section, the zero-field results have the absence of orientational and spatial ordering and show the extent of self-assembly we would expect, considering the results of the Chapter 4. An interesting note is that the zero-field clustering has an almost constant dimer fraction. The initial static magnetic susceptibility highlights the importance of including some modified correlation term. Following that, the platelets are very responsive to low fields. At sufficiently low densities, the magnetization obeys the Langevin susceptibility. Based on the clustering calculations, the external magnetic field promotes a greater degree of self-assembly at low densities. The

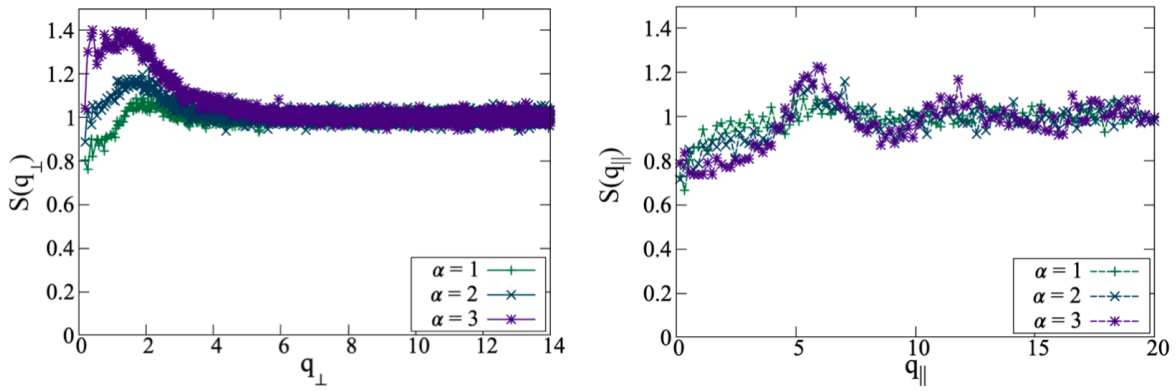

Figure 5.7: Structure factors perpendicular to the field $S_\perp(q)$ (top) and $S_\parallel(q)$ to the field (bottom) at $\phi = 0.05$ and α=1,2,3. The resulting perpendicular-to-field components show a field-dependent increase in peak height and shift of the peak to lower values. The structure factor parallel the field indicates a featureless gas at $\alpha = 1$, which then develops a peak near 2π for $\alpha = 2$ and a second peak around 4π for $\alpha = 3$.

computed structure factors are consistent with field-induced aggregation of the platelets into columns aligned along the field direction, as also seen in the snapshots.

5.2.2 Zero-field Dynamic Susceptibility

Figure 5.8 shows the key findings of this paper: the dynamics magnetic susceptibility $\chi(\omega)$ in zero field for systems over the concentration range $0.010 \leq \phi \leq 0.200$. While some numerical transforms were carried out, the higher densities required fitting due to the noise at long relaxation times. In these cases, $C(t)$ was fitted with a sum of exponentials and $\chi(\omega)$ was calculated as a sum of Debye-like functions, with the simulation data included as points.

The first three plots, Figure 5.8(a)–(c) show the frequency spectra for systems with $\phi = 0.05$, 0.09, and 0.195. We are most interested in the imaginary part $\chi''(\omega)$, as it indicates the relevant time scales. The solid red and black lines indicate the reference Debye spectra for non interacting particles. At $\phi = 0.05$, we see a simple shift in the peak, indicating longer relaxation times. At $\phi = 0.090$, the peak in $\chi''(\omega)$ below $\omega\tau_B = 1$, which indicates the growing effects of interparticle interactions. These generally result in a slowing down of the rotational dynamics due to correlated, collective motions of the particles[153,154,169]. The situation is actually even more complicated, because $\chi''(\omega)$ is considerably broader than a Debye-like function. Since the system at this density contains a mixture of clusters and monomers, there could be a superposition of dynamical features in $\chi(\omega)$. Without a more nuanced model for both the features due to different clusters, and the interactions between them, we cannot fully separate out the features. Instead, we present the two Debye-like components obtained by our methodology that, when summed, provide a sufficiently good fit to the simulation data. One component has its peak near $\omega\tau_B \simeq 1$, and the other near $\omega\tau_B \simeq 0.2$. A tempting interpretation of this is that these peaks correspond to monomers and

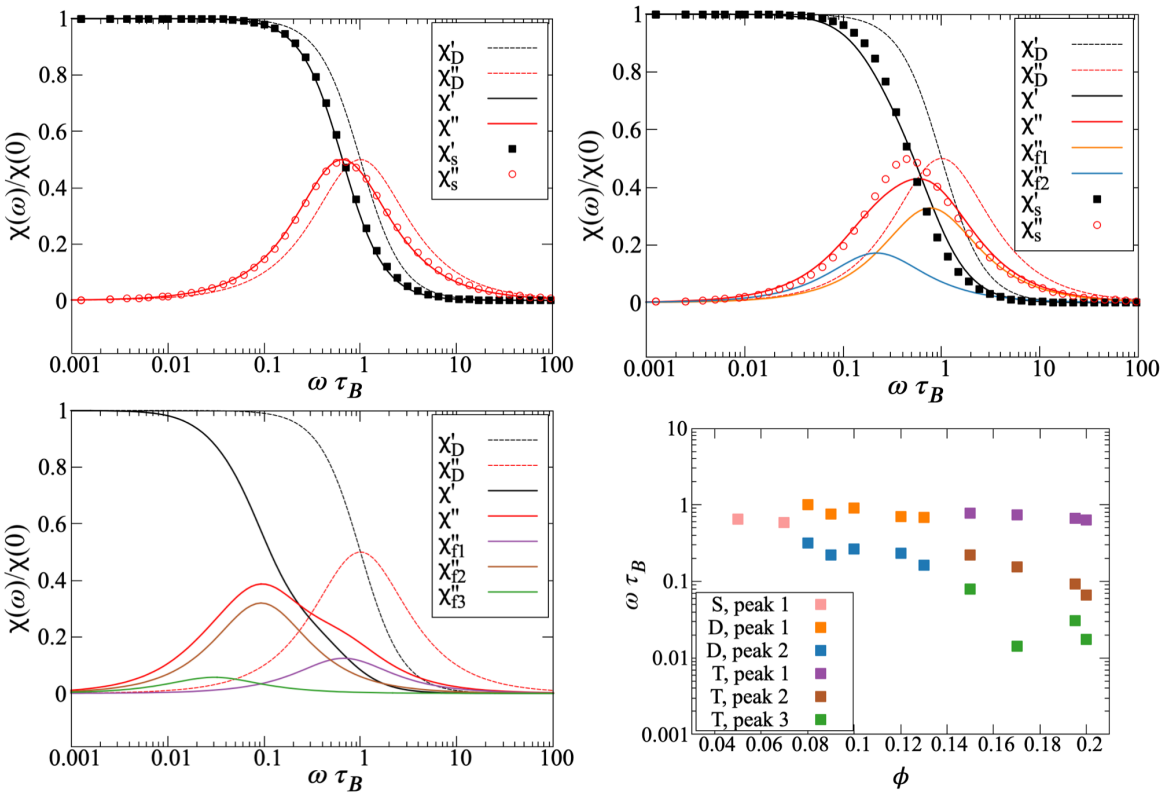

Figure 5.8: The zero-field dynamic susceptibility at a few key concentrations. Black and red dashed lines indicate the Debye susceptibilities, black and red solid lines denote the simulation values based on fits of the autocorrelation functions. Clockwise from the top left: $\phi = 0.05$, $\phi = 0.09$ and, in the bottom row, $\phi = 0.195$. The top row includes simulation data (dots), which agrees well for low ϕ and becomes increasingly problematic for higher ϕ. The additional lines denote the fits to additional peaks, an overview of which is given in the bottom right figure.

clusters (predominantly dimers), respectively.

Turning to a higher concentration, $\phi = 0.195$, it is clear that $\chi''(\omega)$ broadens substantially. In this case, three Debye-like functions were required to provide an adequate fit. This shows that lower frequency reorientational dynamics have appeared, which presumably arise from clusters much larger than dimers. This is consistent with the evolution of the cluster-size distribution discussed in Section 5.2.1. The low-frequency features in $\chi''(\omega)$ are dominant, and there is a clear high-frequency shoulder. The three required components are centered on frequencies of $\omega\tau_B \simeq 1$, 0.08, and 0.03.

It is important not to overstate this interpretation: fitting a discrete sum of exponentials to $C(t)$ is an effective solution, but not well-defined one, especially when a distribution of time scales should be fitted[170,171]. The number of exponentials to fit was always chosen as the smallest possible number yielding sufficient fit accuracy, which is a methodological choice, not a result. This means that having a fit of two or three exponentials does not mean that there are only two or three characteristic timescales. What the broad peaks of the results do indicate, and the fits do reinforce, is that there are motions spanning up to several orders of magnitude. Given this caveat, Figure 5.8(d) shows the peak positions in $\chi''(\omega)$ as functions of the concentration ϕ. As these fits are a numeric approximation, it is important to note that the lowest frequency peaks are most vulnerable to noise, which explains the lack of monotonicity at $\phi = 0.175$. For concentrations $\phi \leq 0.070$, a single characteristic time scale is sufficient to describe $\chi(\omega)$, and the corresponding frequency is a bit less than $\omega\tau_B$ due to a combination of weak interactions between monomers, and the presence of some small clusters. In the concentration range $0.080 \leq \phi \leq 0.130$, two time scales are sufficient, and they differ by up to one order of magnitude. Referring to the results of Section 5.2.1, this concentration range is where a substantial number of dimers are formed, and some larger clusters begin to appear. For concentrations $\phi \geq 0.15$, three time scales are required, and the lowest-frequency motions are almost two orders of magnitude slower than the single-particle ones. So, the combination of the cluster-size distributions and the spectra indicates that there are distinct features arising from single particles (with peak frequencies $\omega\tau_B \sim 1$), small clusters like dimers and trimers ($\omega\tau_B \sim 0.1$), and larger clusters ($\omega\tau_B \sim 0.01$). Cluster formation does not give rise to any high-frequency features, meaning $\omega\tau_B > 1$. Due to the steric exclusion enforced by the particle model, intracluster motions occuring on short timescales could be missed. However, $\chi(\omega)$ is dominated by the contributions from single particles, and clusters with large net dipole moments[155].

5.2.3 Dynamic Susceptibility in an Applied Field

Applying a static external magnetic field H necessitates the split of the susceptibilities into two components, parallel and perpendicular to the field direction. The physical meaning is that when a

weak AC probing field $h(t) = h_0 e^{-i\omega t}$ is applied parallel and perpendicular to H, it causes different dynamic responses in the magnetization. In the parallel case, the average magnetization is $\overline{M} \neq 0$, and $\delta M(t) = M(t) - \overline{M} = \chi_{\parallel}(\omega)h(t)$. In the perpendicular case, $\overline{M} = 0$, and $M(t) = \chi_{\perp}(\omega)h(t)$. For ferrofluids with weakly to moderately interaction spherical colloidal particles, it has been shown that the application of a static uniform magnetic field leads to increases in the single-particle peak frequency with increasing field[156], mostly due to the restoring force of the field and partially due to chain-like correlations between the particles[156,172,173]. These effects are not expected to be very pronounced, unless there is extensive structuring in the system[156].

Based on the previous sections of this paper, we also expect the increasing degree of aggregation in the system to influence the peak frequencies. The peak frequencies for low density suspensions are shown in Figure 5.9. It is subdivided into two plots based on the presence of additional peaks. The left side of shows the effects of increasing (low) density and increasing (low) fields. The lines are guides to the eye, based on the following formulas for the relaxation times of non-interacting spherical particles parallel and perpendicular to the field:

$$\tau_{\parallel} = \left[\frac{\alpha L'(\alpha)}{L(\alpha)}\right]\tau_{\mathrm{B}}; \tag{5.1}$$

$$\tau_{\perp} = \left[\frac{2L(\alpha)}{\alpha - L(\alpha)}\right]\tau_{\mathrm{B}}. \tag{5.2}$$

Here, $L'(\alpha)$ is the first derivative of the Langevin function $L(\alpha) = \coth(\alpha) - 1/\alpha$. These formulas were put forward in Refs.[172] and[173] as the longest relaxation times parallel and perpendicular to the field, respectively, and were shown to agree well with simulation data[156]. A limitation of these formulas is that the relaxation times apply only to isolated or very weakly interacting particles. To take account of some kind of effective field experienced by the particles, the Langevin parameter was replaced by a scaled value, $\alpha_{\mathrm{eff}} = f\alpha$, where the fitted scaling factors were $f_{\parallel} = 0.90$ and $f_{\perp} = 0.95$ for $\phi = 0.001$.

At these concentrations, the degree of clustering is low despite the presence of the field, and this results in the fitting of a single characteristic decay time for both the parallel and perpendicular field components. At the lowest field strength, $\alpha = 1$, the results effectively correspond to the Debye prediction, and there is no significant difference between the relaxation parallel and perpendicular to the field. With increasing field strength, the single particle frequency increases. This effect takes place both parallel and perpendicular to the field, although it is stronger parallel to the field. Both the frequencies, and the difference between them, increase with increasing field strength. These trends are apparent for all three, low concentrations studied, with very little difference. This is to be expected, as these three systems show effectively the same microstructure.

For the highest volume fraction, $\phi = 0.05$, we observe significant increases in clustering. This results in a splitting into two peaks. The results are shown in Figure 5.9 (right), with the field

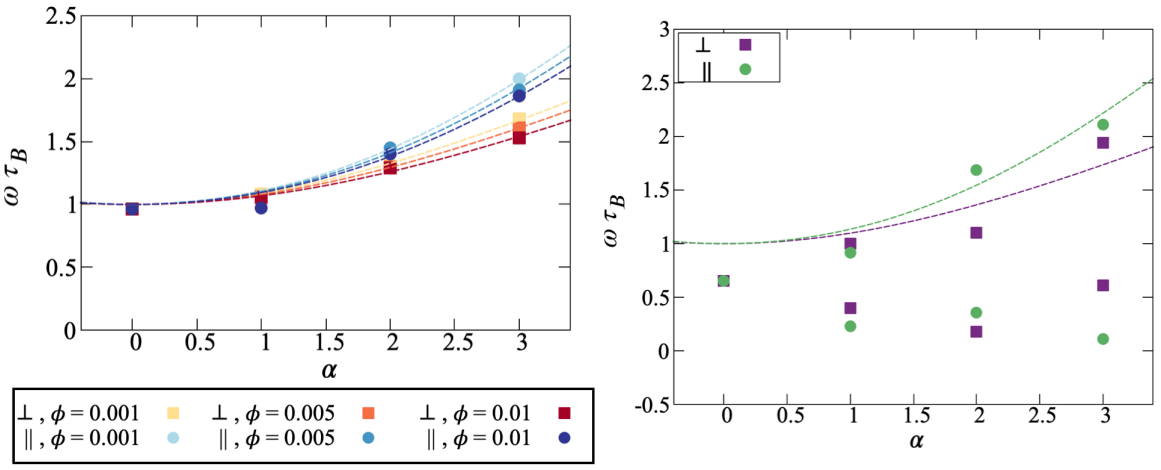

Figure 5.9: Left: the evolution of the peak frequency with increasing density for different fields parallel and perpendicular to the field. Right: the peak frequency at the fixed density of 0.05, with increasing field.

increase shown along the x-axis. As in the previous section, we can identify the higher peak with single particle relaxation, and the lower peak with the relaxation of clusters. The numerical values do not vary smoothly with α, most likely due to poor statistics and possibly due to modelling constraints, but we can put forth a general explanation for the underlying trends. At $\alpha = 0$, $\tau_{\parallel} = \tau_{\perp}$ and longer than τ_{B} due to interaction. Moreover, at this volume fraction, there is no zero-field clustering, and so a single exponential is sufficient to fit $C(t)$. This explains the single peak frequency $\omega\tau_{\mathrm{B}} < 1$.

At the lowest field of $\alpha = 1$, there is already sufficient increase in clustering to split into different characteristic timescales. The higher peak frequencies can be identified with single particles, and they are higher than the zero-field frequencies as expected. The lower peak frequencies are due to clustering. With increasing α, the single-particle frequencies increase, as expected, and the cluster frequencies decrease, due to the increase in cluster size. The ordering of the parallel and perpendicular frequencies is not regular, due to the difficulty in resolving the peak positions in $\chi''(\omega)$ accurately. For single particles, the parallel frequency is generally higher than the perpendicular one, as shown in Figure 5.9 (left).

5.3 Conclusions

5.3.1 Key findings

This chapter's study of sought to explore the link between microstructure and dynamic susceptibility of magnetic nanoplatelets near the coexistence point of monomers and clusters. While the same underlying mechanisms are at play as for dipolar hard spheres, the spectra of platelets have

some interesting quirks. Their microstructure results in relaxation time scales spanning almost two orders of magnitude. These relaxation times can be split into 3 bands: initially, a single exponential suffices to describe the dynamic susceptibility $\chi(\omega)$. As the aggregation increases, we used two and then three exponentials to represent the distinct timescales. The highest-frequency feature present in all cases corresponds to single-particle rotations. These are only weakly affected by the long-range dipole-dipole interactions. We identify the other timescales with clusters: in the fit, these are separated roughly into small and large clusters, based on the order of magnitude of their relaxation time, although this distinction cannot be made without a more precise analytical model. When an additional static external field is applied, the aggregation in the system increases strongly. At low concentrations, we observe an increase in the in-field particle relaxation frequency, due to the additional torque arising from the field. As the aggregation also increases, some new low-frequency features appear. Weaker versions of these trends appear perpendicular to the field. A more detailed analysis of these changes would require both a more nuanced rotational model of how the anisotropic clusters undergo Brownian rotation, and interact with one another.

5.3.2 Relation to Experiment

As discussed in Chapter 3, the experimental systems of barrium hexaferrite nanoplatelets have a lognormal polydisperse particle size distribution, with up to an order of magnitude difference in magnetic core size[152]. Since the Brownian relaxation times τ_B are proportional to $1/d^2$, we can make the following estimate: assuming a particle diameter of $d = 20$–80 nm, the range of relaxation times should vary by a factor of around $(80/20)^2 = 16$. If we roughly split the system into 'small' and 'large' fractions, then even without clustering or interparticle interactions, the peak frequencies would correspond to $\omega \simeq \tau_{B,small}^{-1}$ and $\omega \simeq \tau_{B,large}^{-1}$, respectively. Given that the gap between high-frequency and low-frequency peaks in experiment was found to span up to three orders of magnitude, this factor of 16 is clearly not sufficient. However, based on the results in this chapter, we know that the combination of interparticle interactions and clustering can lead to an increase in the relaxation times up to two orders of magnitude. The polydispersity in experiment also means that self-assembly would not be as straightforward as presented. If the large particles self-assemble into clusters, and the small particles do not self-assemble, then the dynamic magnetic susceptibility would retain a high-frequency feature at $\omega \simeq \tau_{B,small}^{-1}$ and a low-frequency feature at $\omega \ll \tau_{B,large}^{-1}$ (due to self-assembly), it is entirely possible that the frequencies could vary by up to three orders of magnitude.

5.4 Methods

Brownian Dynamics simulations were performed using the simulation package ESPResSo, version 4.1.4 and 4.2.0[121]. Brownian Dynamics was achieved by overdampening Langevin simulations in the NVT ensemble, meaning that N particles in simulation box of volume V at temperature T were simulated, with the friction coefficient $\gamma = 20$ and timestep $\delta t = 0.005$. The system is 3D, with periodic boundary conditions used to mimic a larger suspension. This gave a Brownian rotation time of $\tau_B^* = 10$ in Lennard-Jones units. The inertia tensor was set to that of a cylindrical platelet with radius $R = 3\sigma/2$ and height $h = \sigma$, and so the elements were $I_x = I_y = m(3R^2 + h^2)/12$, and $I_z = mR^2/2$, where $m = 2$ is the platelet mass. This relaxation value does not match the corresponding Stokesian-derived γ for spheres. In this work, the rotational diffusion of a platelet would not be expected to match that of a sphere. While there are solutions for oblate spheroids, specifically Perrin coefficients[174], these shapes have a rounded surface not applicable to the present case. However, the choice τ_B and γ was shown to reproduce the relaxation of dipolar particles both in terms of the magnetic autocorrelation function, and reproduces the Debye spectra.

Initial simulations were carried out with $N = 1024$ particles at volume fractions $\phi = 0.050$ and $\phi = 0.200$. Long simulations were required to access all of the relevant features in the dynamic magnetic susceptibility, and so for subsequent calculations at other volume fractions, smaller systems of $N = 256$ particles were used. The volume fractions studied were as follows. For the field-free case, simulations were run at $\phi = 0.010$, 0.050, 0.070, 0.080, 0.090, 0.100, 0.120, 0.130, 0.150, 0.170, 0.195, and 0.200. For the case of an external applied field, simulations were run with $N = 256$ particles at $\phi = 0.001$, 0.005, 0.010, and 0.050, *i.e.*, at lower concentrations because of field-induced aggregation. The temperature was fixed at $T = 1$, and the box length was varied between runs in order to achieve different values of the volume fraction $\phi = Nv_p/V$, where $v_p \pi R^2 h = 9\pi\sigma^3/4$ is the platelet (cylinder) volume. Simulations were run for a warm up of $10^6 \delta t$ equilibration steps, after which magnetization was sampled every timestep and the system's particle positions, orientations, momenta and velocities were recorded every $10^4 \delta t$.

The platelets were constructed as in Chapter 4, with the same dipole-dipole and soft-sphere interactions. Where an external field is applied, the particle-field interaction was given by the Zeeman interaction $U_H = -\mu_0(\vec{\mu}_m \cdot H)$. Unless otherwise specified, the static properties in Section 5.2.1 were calculated using the same methodology as Chapter 4.

The dynamic susceptibilities were calculated as in Ref[155] by taking the Fourier transform of the magnetization autocorrelation function $C(t)$, where:

$$C(t) = \frac{\langle M(t) \cdot M(0) \rangle}{\langle M^2 \rangle} \tag{5.3}$$

with $M = \sum_{i=1}^{N} \mu_i$. With an applied external magnetic field, $\langle M \rangle \neq 0$, and therefore $C(t)$ will not

decay to zero. In those cases, we replaced $\delta M(t) = M(t) - \langle M \rangle$ as in[156]. The dynamic susceptibility is given by

$$\frac{\chi(\omega)}{\chi(0)} = 1 + i\omega \int_0^\infty C(t) e^{i\omega t} dt. \tag{5.4}$$

At systems with low volume fraction ϕ, which had low degrees of self-assembly, $C(t)$ and $\chi(\omega)$ were characterized by a single, short time scale, and it was found that direct numerical transforms of $C(t)$ (using scipy) were adequate. In order to reduce the noise, one can also apply windowing functions. These effectively consist of multiplying the function with a bounded function that tapers to lower values, effectively reducing the scale of the noisier tail of the function. For the autocorrelation functions studied, the Blackman window was found to be the most effective. With increasing concentration, the presence of slower relaxation timescales meant that numerical transforms were found to be inadequate. In these cases, $C(t)$ was fitted with a sum of exponentials,

$$C(t) = \sum_{i=1}^{n} a_i e^{-t/\tau_i}, \tag{5.5}$$

where $\sum_{i=1}^{n} a_i = 1$, and $n \leq 3$. The value of n was chosen to be as low as possible, while maintaining accuracy and realistic fitting errors. Given this representation of $C(t)$, the dynamic magnetic susceptibility $\chi(\omega) = \chi'(\omega) + i\chi''(\omega)$ is given by the sum of Debye susceptibilities:

$$\frac{\chi'(\omega)}{\chi(0)} = \sum_{i=1}^{n} \frac{a_i}{1 + \omega^2 \tau_i^2}; \tag{5.6a}$$

$$\frac{\chi''(\omega)}{\chi(0)} = \sum_{i=1}^{n} \frac{a_i \omega \tau_i}{1 + \omega^2 \tau_i^2}. \tag{5.6b}$$

6 - Binary Mixes of Magnetic Spheroids

Inspired by the experimental protocol of mixing indium- and scandium doped magnetic nanoplatelets, this chapter explores properties of platelet mixtures with different magnetic moments. This is contrasted with mixtures of dipolar ellipsoids, with some dipolar sphere reference systems. We explore the microstructure to see if the presence of depletants or less magnetic particles results in quantative or qualitative changes to the radial distribution, structure factors, orientational correlations, bond order parameters or static magnetic susceptibility. Similarly to spherical particles, we find the expected promotion of aggregation in depletant mixtures of dipolar spheres present for platelets. However, we find demixing effects once self-assembly occurs in both platelets and ellipsoid systems that is not found for comparable spheres. We also explore the potential for a liquid-liquid phase separation.

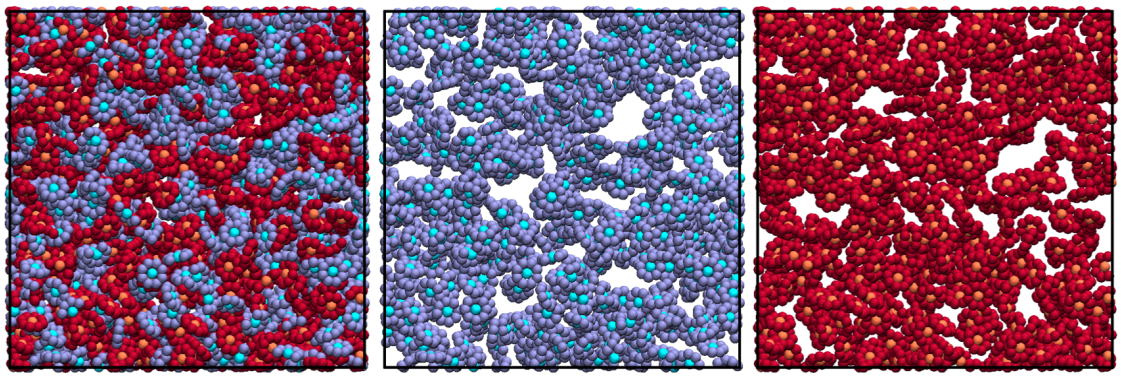

Figure 6.1: Simulation snapshot of aspect ratio 1:3 platelets of non-magnetic (blue) and magnetic $\lambda = 5$ (red) particles at $\phi = 0.2$. Visually, it is not possible to distinguish if their distribution is random.

The material in this chapter being prepared for publication:

[5] Rosenberg M., E. Pyanzina, E. Novak, S. Kantorovich, "*Binary Mixtures of Dipolar Spheroids*", in preparation

6.1 Introduction

In Soft Matter literature, the term "binary mixtures" most often refers to colloidal suspensions of particles with two distinct size scales. However, there has also been an interesting line of theoretical and computational investigation into equal-size mixtures of dipolar hard (or soft) spheres, where "binary" refers to the choice of dipolar moment. These studies predominantly focused on the phase behavior, demixing and the possibility of a liquid-vapour phase equilibrium[175–179]. Multiple groups carried out theoretical investigations using density functional theory (DFT)[180,181], including finding a demixing phase transition in mixtures of neutral hard spheres (depletants) and dipolar hard spheres with sufficiently strong dipolar interactions[182]. More recently, some works explored self-assembly and gelation, although often including a size difference between particles with different magnetic moments[183–185].

Binary mixtures of hard platelets have been studied, most frequently with density functional theory approaches[186–188]. Mixes of spheres and platelets have also attracted attention[189]. However, to the extent of our knowledge, no computational studies of platelets with equal size and differing magnetic moments perpendicular to the plane have been carried out. Similarly, the literature on dipolar mixtures of ellipsoids focuses on sphere-ellipsoids mixtures[190]. The work described in this chapter seeks to address this gap in the literature. While binary mixes of ellisoids, platelets and spheres were studied, this chapter focuses on the latter two shapes, as the ellipsoid simulations were carried out by E. Pyanzina. The work on platelets also ties into experimental investigations, where mixtures of indium- and scandium- substituted barrium hexaferrite are often used[134]. These different platelets have a very similar size (polydisperse) distribution, but slightly different magnetization. Depending on the mixtures, this resulted in inhomogenity, phase separation, or stripe-like structures not usually observed in the original barrium hexaferrite samples. This chapter focuses both on the microstructure, the importance of which has been discussed in the previous two chapters, and an exploration of which aspects of dipolar hard sphere phase behavior and demixing carry over to these shapes.

6.2 Results

Before diving into different measure calculations, it is important to find outline some ideas of interest. Firstly, we expect the presence of depletants to increase the self-assembly. Within this self-assembly, it would be interesting to see if the different magnetic moments of the particles play a significant role. In binary mixtures of oppositely-charged colloids, smaller particles can have "poisoning" effects on the overall structure, inhibiting ordering or creating defects[191].

In platelet mixes with fewer strongly magnetic particles, as shown in Figure 6.1, the more magnetic particles visually seem to form pockets, as if phase separating. While the particles are

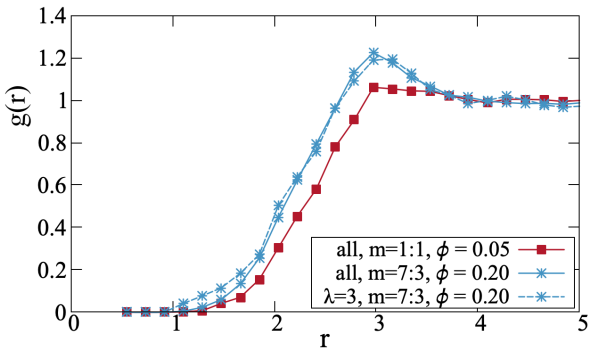

Figure 6.2: Radial distribution function $g(r)$ of aspect ratio 1 : 3 platelets, at different volume fractions (red, blue), mixture ratios (squares, stars) and of different particle types (dashed lines). We see that the suspension appears to be in a gaseous phase, growing more fluid-like as ϕ increases. Considering only the radial distribution of magnetic particles, there is a slight increase in $g(r)$ near the closest-contact distance 1.

expected to de-mix once self-assembly occurs, this intermediate stage could also be of interest. Additionally, these results can be contrasted with binary mixes of ellipsoids to tease out the differing shape effects.

6.2.1 Radial Distribution of particles

With Figure 6.2, we begin with the mixtures of 1:3 aspect ratio platelets with $\lambda = 0$ (depletants) and $\lambda = 3$. As discussed in previous chapters, such low λ for platelets does not lead to self-assembly. The resulting $g(r)$ curves are, therefore, mostly determined by the density ϕ (shown by varying colors). Increasing ϕ results in a soft-sphere fluid state, while low ϕ appears closer to gaseous. Due to the low magnetic interactions, the mix ratio m does not affect the results and neither does splitting the function by particle types, with one exception: for high values of ϕ, there is a slight increase of the radial distribution function of magnetic particles at short range (blue dashed line).

In Figure 6.3, we increase the magnetic particle interaction strength to $\lambda = 5$, again with a varying proportion of depletants. We see that the overall shape is rather gas-like, depending on ϕ, albeit now with a nearest neighbor peak. The small nearest neighbor bump is already present for magnetic particles at the lowest volume fraction, given sufficient mix ratio. However, the overall shape and the behavior of the depletant-depletant and mixed $g(r)$ remain the same, as in the 0 : 3 case. At high ϕ, we find a close-range signature of the magnetic particles even in the total radial distribution function, which depends on the particle volume fraction. In summary, although $\lambda = 5$, the magnetic particles show behavior that is more comparable to $\lambda = 3$ in spheres. It must be noted that, due to the orientational constraints, platelets show the average neighbor and the

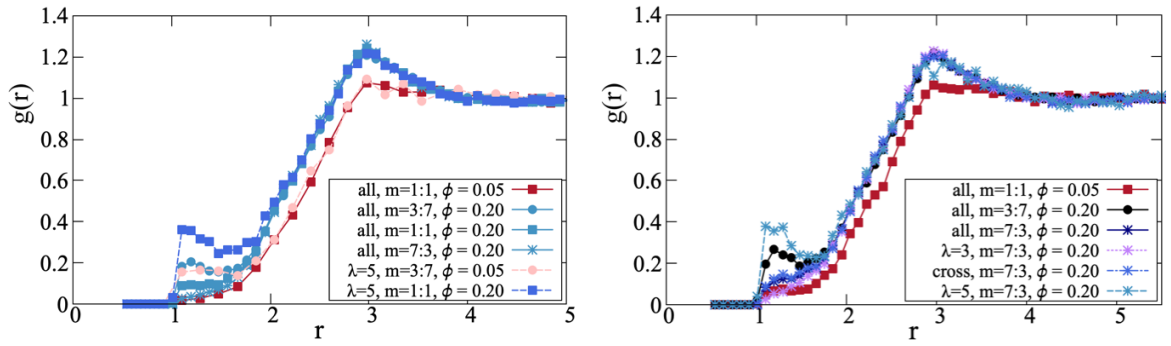

Figure 6.3: Radial distribution function $g(r)$ of aspect ratio 1 : 3 platelets. We see a similar underlying phase to Figure 6.2, but with a pronounced peak around one platelet diameter, as well as a growing feature at the closest-contact distance 1. Radial distribution function $g(r)$ of aspect ratio 1 : 3 platelets, with $\lambda = 3 : 5$. We see a close resemblance to the 0 : 3 case, except for the cross and lower-λ fractions.

self-assembly peaks at different distances, which accounts for some of the height difference to dipolar soft spheres.

As noted previously, the mixtures of magnetic platelets could give an indication of a potential phase separation. We begin again with aspect ratio 1 : 3 platelets and $\lambda = 3 : 5$, shown on the right in Figure 6.3. As previously, we see the shape is dominated by the density, and the general trends seem to agree with the left, with the difference that the cross-distribution function now shows better agreement with the total distribution function, since it also includes the pre-assembly feature near 1. While the overall shape only depends on ϕ, as previously seen, the close-range feature height depends on the fraction of $\lambda = 5$ particles.

In order to attempt to find self-assembly effects in the nanoplatelet suspensions, we can increase the value of λ. Based on Chapter 4, we begin with $\lambda = 0 : 7$ as depicted in Figure 6.4 a) and now find both the nearest-neighbor peak, and many of the dependencies that we have seen for spheres. For $\phi = 0.05$, while the cross-type and depletant radial distributions remain featureless, the total and depletant distribution functions show one peak. Interestingly enough, the density has a much smaller effect on peak height than for the spherical case, as shown by the inclusion of the blue curve. At $\phi = 0.02$, shown in 6.4 b), we again find no distinction between cross and depletant radial distribution functions - as opposed to the spherical case - and see the self-assembly features in the total and magnetic fraction distribution functions, which both depend on the mixture ratio. For the magnetic particles and total radial distribution functions where magnetic particles dominate, there is also a second assembly peak slightly past 2.

As increasing λ dramatically increases the self-assembly, we attempt to sample some $\lambda = 0 : 10$ configurations, one of which is shown in Figure 6.4 c). Unfortunately, the high degree of self-assembly in the system lead to equilibration issues (as in previous chapters). We see the self-assembly into chains as evidenced by the periodic high peaks in the radial distribution, as well as

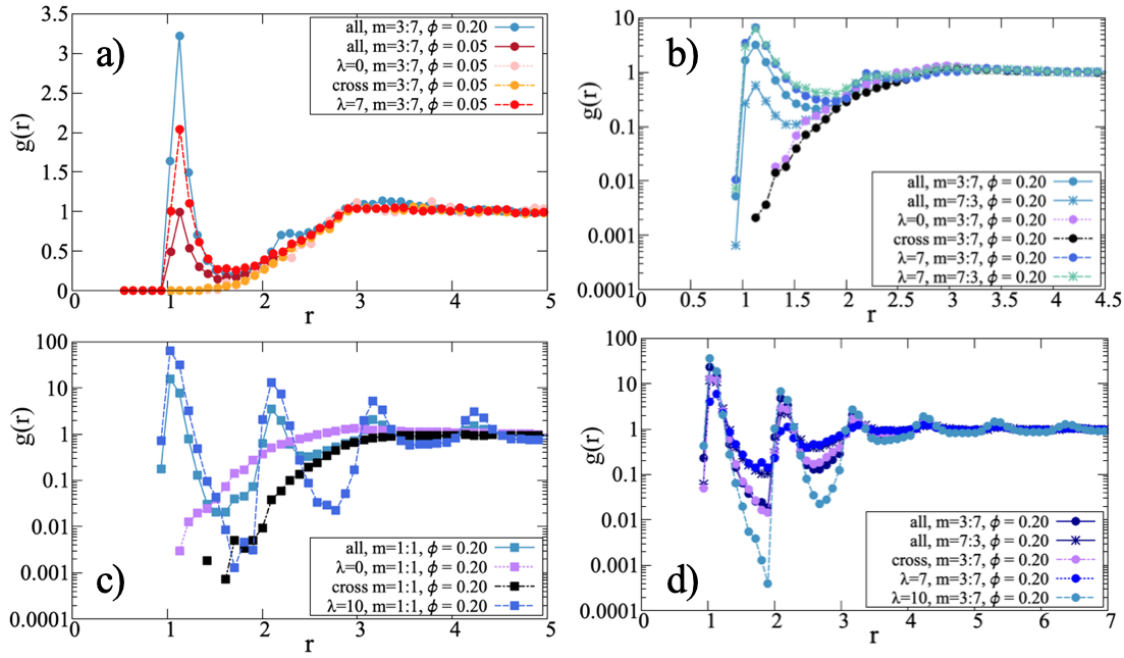

Figure 6.4: Radial distribution function $g(r)$ of 1 : 3 platelets with varying dipolar coupling constants and densities. Figure a): $\lambda = 0:7, \phi = 0.05$. Figure b) $\lambda = 0:7, \phi = 0.20$, Figure c): $\lambda = 0:10, \phi = 0.20$ and Figure d) $\lambda = 7:10, \phi = 0.20$ We observe self-assembly in the magnetic particles, while the depletants remain disordered and distributed- although the cross radial distribution indicates some separation between the types.

the low values of the depletant and cross distribution functions. At these values of $\lambda = 0:10$, we also find the cross function dipping significantly below the others, suggesting that the depletants are mostly separated from the self-assembled structure.

For mixtures of $\lambda = 7:10$, as shown in Figure 6.4 d), the system has long-range periodic structure, indicating a high degree of ordering. Interestingly enough, the values between the different peaks decrease more sharply than the peak height (barely) increases with the amount of $\lambda = 10$ particles either in the system or considered by the distribution function. The cross distribution function is similar to the total distribution function, suggesting that the $\lambda = 7$ particles are integrated into the structures as opposed to phase separating.

These results contrast findings for systems of dipolar soft sphere mixtures, as shown in Figure 6.5, where for all parameters studied we observe a high nearest neighbor peak, which depends on the volume fraction and the mix ratio. In a), at $\lambda = 0:3, \phi = 0.05$, this peak is superimposed onto a gaseous-type radial distribution of particles, and it grows with the proportion of magnetic particles in the mix. For $\phi = 0.20$ (b), presumably due to the overall proximity of particles in such a dense suspension and the normalization, this effect is not seen in the same way. Moreover, Figure 6.5 b) shows a more fluid-like distribution of particles. Splitting the radial distribution function into its different components indicates that the peak shape is being set by the $\lambda = 3$ particles as

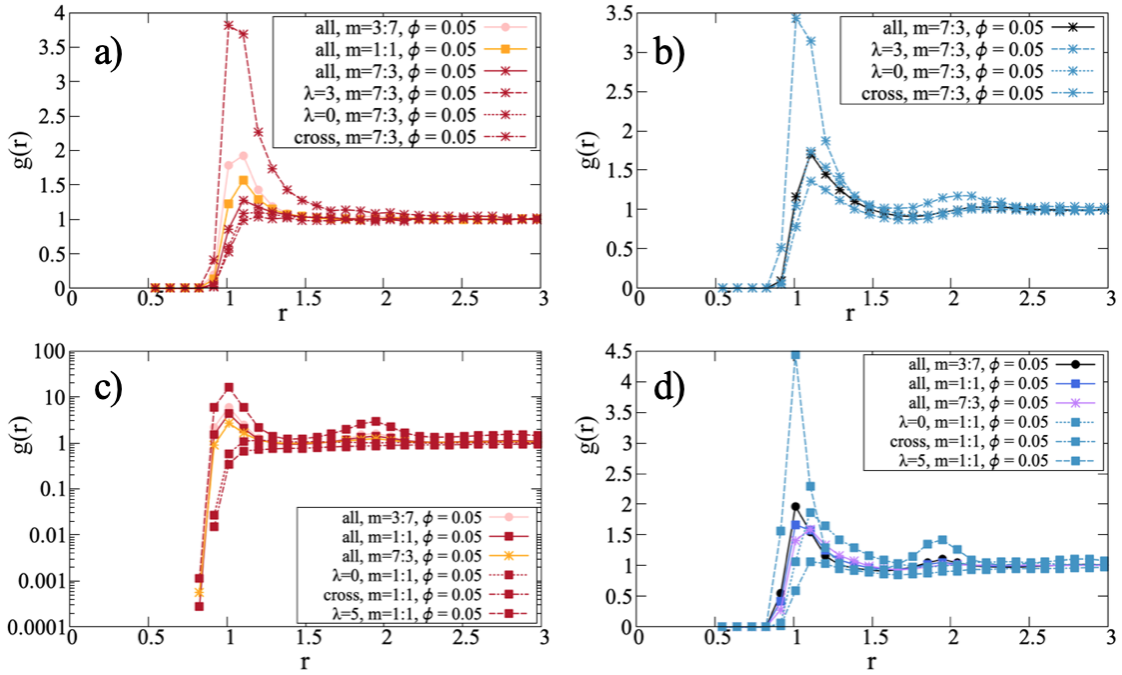

Figure 6.5: Radial distribution function $g(r)$ of dipolar soft spheres, shown for a) $\lambda = 0:3, \phi = 0.05$, b) $\lambda = 0:3, \phi = 0.20$, c) $\lambda = 0:5, \phi = 0.05$ and d) $\lambda = 0:5, \phi = 0.20$. We see that the magnetic particles have some degree of self-assembly, or heightened proximity, regardless of whether the underlying density resulted in a gas-like state (a) or fluid-like state (b). In (c) and (d), we see peaks corresponding to self-assembly for the total and magnetic functions, while the depletant and crossover distribution functions appear more gaseous.

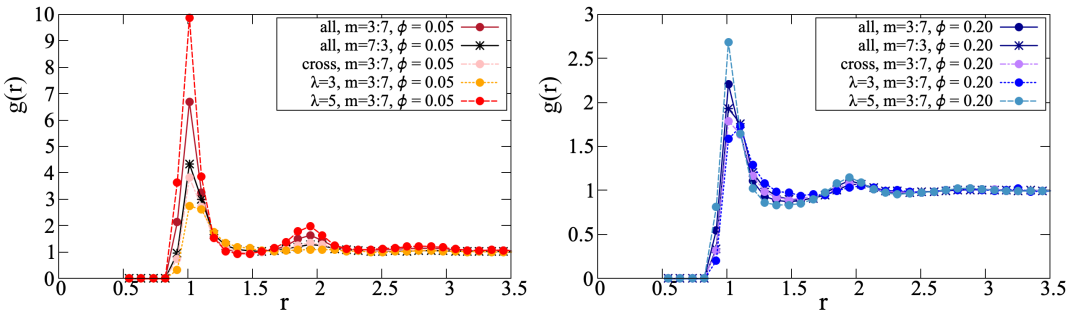

Figure 6.6: Radial distribution function $g(r)$ of soft spheres, with $\lambda = 3:5$.

expected. It is interesting to note that the cross radial distribution function is lower than all other options, hinting at some slight sorting of the particles by type. The peak is also slightly shifted. With increasing magnetic particle fractions, it moves from the soft-sphere Weeks-Chandler-Anderson maximum of 1.12σ to values closer to 1. In the lower row of Figure 6.5, c) and d), the mixture of $\lambda = 0$ and $\lambda = 5$ soft particles has a strong dependence on the density, volume fraction and mixture ratio due to the self-assembly of the magnetic particles. For c), where $\phi = 0.05$, $g(r)$ is shown in logarithmic due to the peak height. We see the clear dependence on magnetic particle fraction, with a second peak indicating some cluster formation. The depletant and cross curves are the lowest, gaseous-types, suggesting that the self-assembly of the magnetic particles has begun to separate them from the remaining fluid. Another effect is best seen at in d) at $\phi = 0.2$, where the same trends remain, but, we can see the clear difference between the nearest-neighbor peaks at the respective interaction minima. When the mix ratio is varied, this also clearly shifts the peak depending on which interactions are dominant.

In Figure 6.6, the $g(r)$ on the left shows a suspension that is clearly fluid-like, with a second peak below 2, which indicates assembly of multiple particles. For $\phi = 0.05$, there is a marked height difference between the different distribution functions and mixture ratios. The only qualitative difference in shape is for the $\lambda = 3$ curves, which show a broader peak, indicating more Weeks-Chandler-Anderson -type spacing. This is even more evident for $\phi = 0.2$, shown on the right, where the only difference between the cross and $\lambda = 3$ depletions lie in the peak shape, not height. These results give the impression that for spheres, there is no pronounced phase separation between the different magnetic constituents.

Increasing the aspect ratios of the platelets to $1:5$, Figure 6.7 will briefly explore what the progression of these trends with growing anisotropy are. In Figure 6.7 a), we present an overview of $\lambda = 0:3$ and $\lambda = 0:5$. A single curve of the $\lambda = 0:3$ systems is included as reference: however, these systems effectively show no signs of magnetic interactions influencing $g(r)$. At the higher value of λ, we have the same close-range pre-assembly bump for magnetic particles. Despite the different aspect ratio, these results closely resemble those for aspect ratio $1:3$ at $\lambda = 0:5$. The

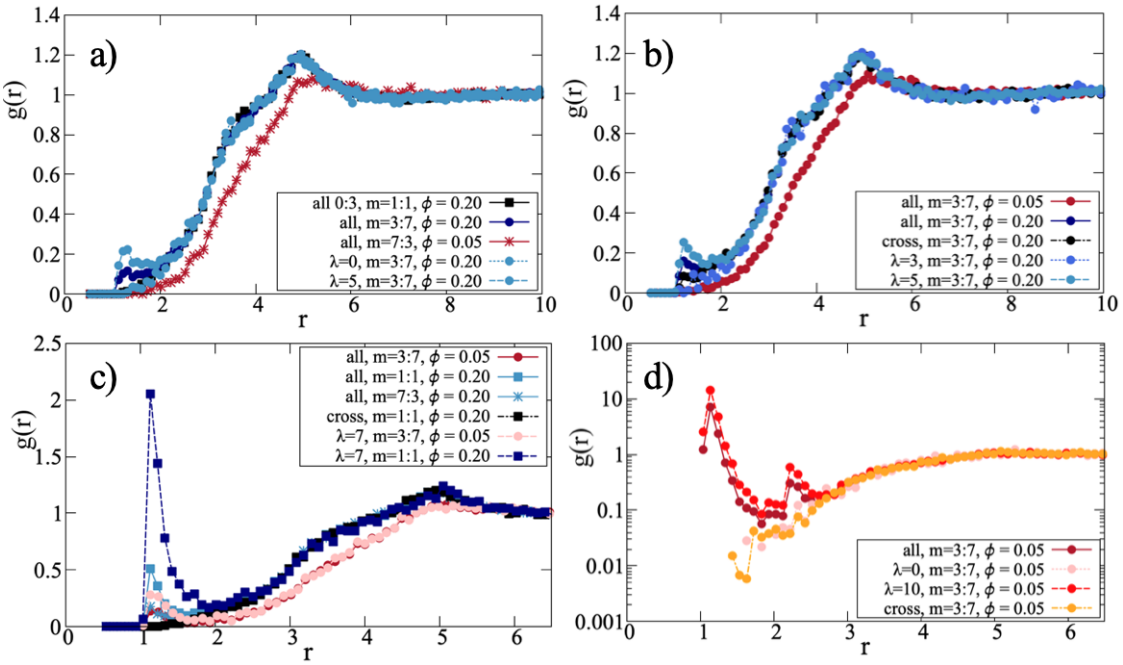

Figure 6.7: Radial distribution function $g(r)$ of aspect ratio 1 : 5 platelets, with $\lambda = 0:3$ and $\lambda = 0:5$ in a), followed by $\lambda = 3:5$ in b). Bottom row: $\lambda = 0:7$ (c) and $\lambda = 0:10$ (d). For a) and b), we see that the density ϕ fully determines the curve shape. In c) and d), the self-assembly plays a key role.

only differences are that the near feature has lower values, and the overall slope of $g(r)$ between closest-contact and platelet diameter is less smooth. For Figure 6.7 b), $\lambda = 3:5$, the situation is virtually identical to the 1 : 3 aspect ratio platelets, with ϕ governing the overall shape, a slight peak near the self-assembly minimum, but with hints of the bump near 2 that was also seen in Figure 6.6 (left). The cross distribution function is barely above the $\lambda = 3$ distribution function.

In Figure 6.7 c) and d) we raise the value of λ to $\lambda = 0:7$ (c) and $\lambda = 0:10$ (d), at which point we expect some self-assembly. This is partially borne out by $\lambda = 0:7$ (c), where there is the characteristic foot at lower densities, a self-assembly peak at higher densities and a strong dependence on the magnetic volume fraction, again closely resembling the aspect ratio 1 : 3 case, albeit without the second assembly peak. For $\lambda = 0:10$ (d), the results more closely resemble a dense suspension of 1 : 3 aspect ratio platelets: there is a high first and indications of a secondary peak, but no longer range structure. Both the depletants and cross distribution functions are gaseous. Since increasing the density further resulting in equilibration issues, we can see this as the last stage of the system before the long-chains regime alluded to in Chapter 4.

In the $\lambda = 7:10$ mixes, shown in Figure 6.8, the system shows multiple self-assembly peaks continuing in range. The effects are more noticeable for $\phi = 0.2$, which is why a single $\phi = 0.05$ is included as a height reference. Very interestingly, the $\lambda = 7$ distribution function essentially shows some noise at close range, while the cross distribution function has clear peaks. This suggests

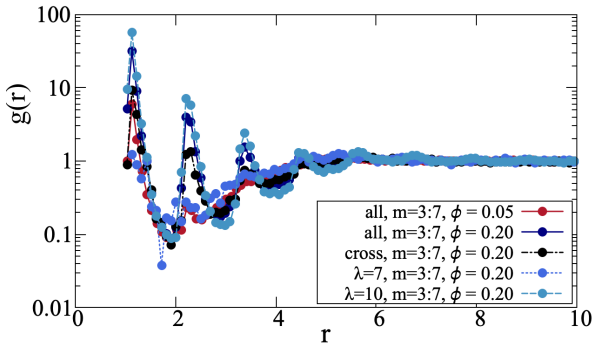

Figure 6.8: Radial distribution function $g(r)$ of aspect ratio 1:5 platelets, with $\lambda = 7:10$ (right).

that the $\lambda = 10$ platelets assemble, and include $\lambda = 7$ platelets within their structures as opposed to separating. The $\lambda = 7$ particles do not appear to support longer structures on their own, as evidenced by the lack of subsequent peaks.

Regarding our initial questions, we have found that the presence of depletants does seem to increase the aggregation in the system. The situation for potential phase separation is more complex. However, our choice of aspect ratios and coupling constants appears to sample through the phase diagram such that we can make more general predictions.

6.2.2 Structure Factors

This section will depict center to center structure factors $S(q)$. In Figure 6.9, a) and b) we can see that, in keeping with the previous, the suspensions of aspect ratio $1:3$ platelets with depletants and $\lambda \leq 5$ show no significant structuring or magnetic influence. At the lowest densities, the structure factor $S(q)$ even appears almost flat. There is a feature roughly corresponding to the peak found in Figure 6.2, although it is too broad to match precisely. The lack of effect of the magnetic particles is made clear by contrasting the structure factor considering only magnetic particles (at 70% mix ratio, light blue) and depletants (at 70% mix ratio, purple). For $\lambda = 0:3$, a) these two curves are identical. There is a slight difference for $\lambda = 0:5$, b) where the curve for $\lambda = 5$ has slightly higher values, but the total structure factor is still identical across different mix ratios.

In Figure 6.9c), $\lambda = 0:7$, which still bears a strong resemblance to the $0:5$ case in terms of $S(q)$ shape. For $\phi = 0.05$, the curve is almost flat and featureless. At $\phi = 0.02$, we finally see an effect of the magnetic particle fraction on the suspension structure. The compressibility clearly depends on the magnetic volume fraction, changing the tail of various $S(q)$. At $\lambda = 0:10$, Figure 6.9d), we see a combination of curves that are more reminiscent of the low-ϕ results: the depletant curves appear mostly flat, while the others have an increasing tail that - for the overall $S(q)$)- depends on the magnetic volume fraction. These are however the first platelet structure factors to show a self-assembly feature, with the sharp peak at $2\pi/6 \approx 1$ for the magnetic particles

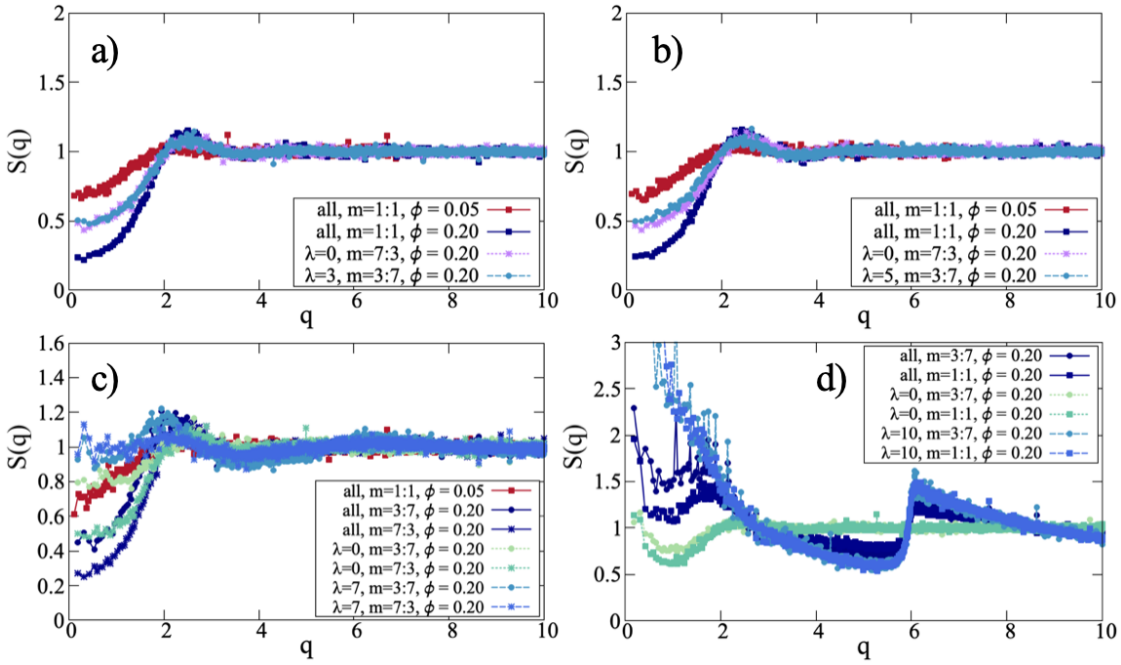

Figure 6.9: Structure factor $S(q)$ of aspect ratio 1:3 platelets, with $\lambda = 0:3$ (a), $\lambda = 0:5$ (b), $\lambda = 0:7$ (c) and $\lambda = 0:10$ (d). The curves in a) and b) solely depend on the volume fraction, with no indication of a magnetic signature.

and total curves. These $S(q)$ are also the first to show a feature near low-q, but as for the previous λ values, these peaks are all quite broad. In summary, we can say that while increasing the value of λ can result in some platelet properties more closely resembling those of soft spheres, the structures of the suspensions remain very different.

Returning again to purely magnetic mixtures in Figure 6.10, where on the left, aspect ratio 1:3 platelets with $\lambda = 3:5$ appear to be structured almost identically to the $0:5$ case shown in Figure 6.9. The only exception is that the less magnetic particle curve for $\phi = 0.20$ at the $7:3$ mix ratio corresponds to the overall $S(q)$ for $\phi = 0.05$. On the right side of this Figure, we see the reemergence of the stark self-assembly peak near 6. The total $S(q)$ have a bump that roughly corresponds to nearest-neighbor distance; both they and the more magnetic platelets have increased compressibility.

By contrast, dipolar hard spheres show stark differences in behavior with both volume fraction and mix ratio, which is why Figure 6.11 is split into the $\phi = 0.05$ (a,c) and the $\phi = 0.20$ (b,d) curves. For a), lower ϕ, we see a similar lack of structure as in the platelets' case. However, the small-q behavior varies with the fraction of magnetic particles. This indicates that despite the lack of structuring and low magnetic interaction strength, we still find an increase in isothermal compressibility. This effect grows even more pronounced for b), $\phi = 0.02$. At this density, we clearly see an overall fluid-like structure. While the total values of $S(q)$ are again virtually identical,

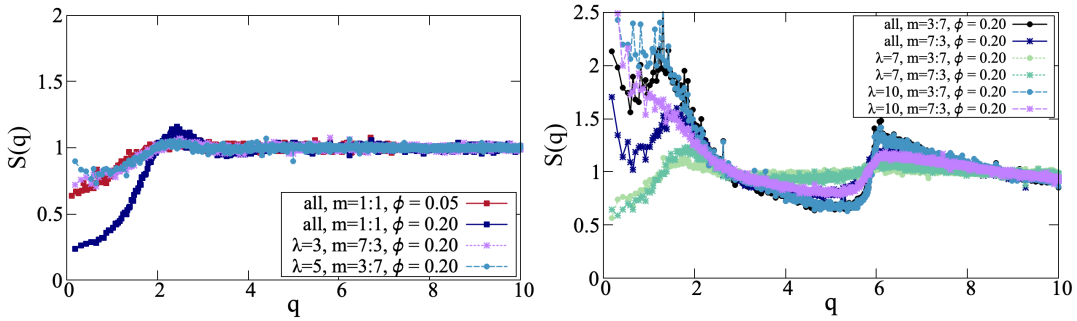

Figure 6.10: Structure factor $S(q)$ of aspect ratio 1 : 3 platlets, with $\lambda = 3:5$ (left) and $\lambda = 7:10$ (right).

we see a peak shift to higher q for the magnetic particle $S(q)$. Interestingly, the compressibility also increases in the depletant curves- this is a passive effect dependent on the fraction of magnetic particles, and the peak position does not change.

If the magnetic interaction strength in the sphere systems is increased even more, as shown in Figure 6.11 c),d), we will see some self-assembly. The most pronounced difference is seen at $\phi = 0.05$ (c), where the underlying suspension remains mostly gaseous, the depletants completely so and the magnetic particles now have a peak at 7, which gives $2\pi/7 \approx 0.9$, that corresponds to the soft-sphere minimum. The compressibility also escalates. For $\phi = 0.20$, d), the effect is more similar to $\lambda = 0.3$: the first peaks have now sorted into self-assembly (shift to larger q) and the Weeks-Chandler Anderson for depletants (remaining at lower q). The total $S(q)$ is still fluid-like, with a slight compressibility increase, which is typical for high-density, low-λ dipolar hard spheres. We also find hints of a second peak just before $q = 14$, suggesting more assembly. For comparison, the mixtures of $\lambda = 3:5$ of dipolar soft spheres shown in Figure 6.12 appear to a textbook case of increased compressibility in the gas phase (left) and some more subtle increases for the fluid phase (right). It is interesting that these are not more pronounced, which is probably due to the self-assembly.

For the platelets with the aspect ratio 1 : 5, as shown in Figure 6.13, depletant mixes of 0 : 3, 0 : 5 and 3 : 5 (a,b) both only show dependence on ϕ, with the same matching of the depletant and magnetic $S(q)$ by volume fraction as previously noted. Since $\lambda = 5$ is far below the self-assembly threshold for aspect ratio 1 : 5 platelets, this was to be expected. Increasing the value of λ to 0 : 7 or 0 : 10 (c) does not result qualitative changes: both still show mostly flat curves for $\phi = 0.05$. At $\phi = 0.20$, we can see no marked differences from the previous case either (note the different volume fraction of depletants). In brief, the suspensions of platelets with aspect ratio 1 : 5 do not attain significant structuring for these mixes. The outcomes for $\lambda = 7:10$ (d) and higher density are more interesting: there is a significant feature and an increase in the compressibility.

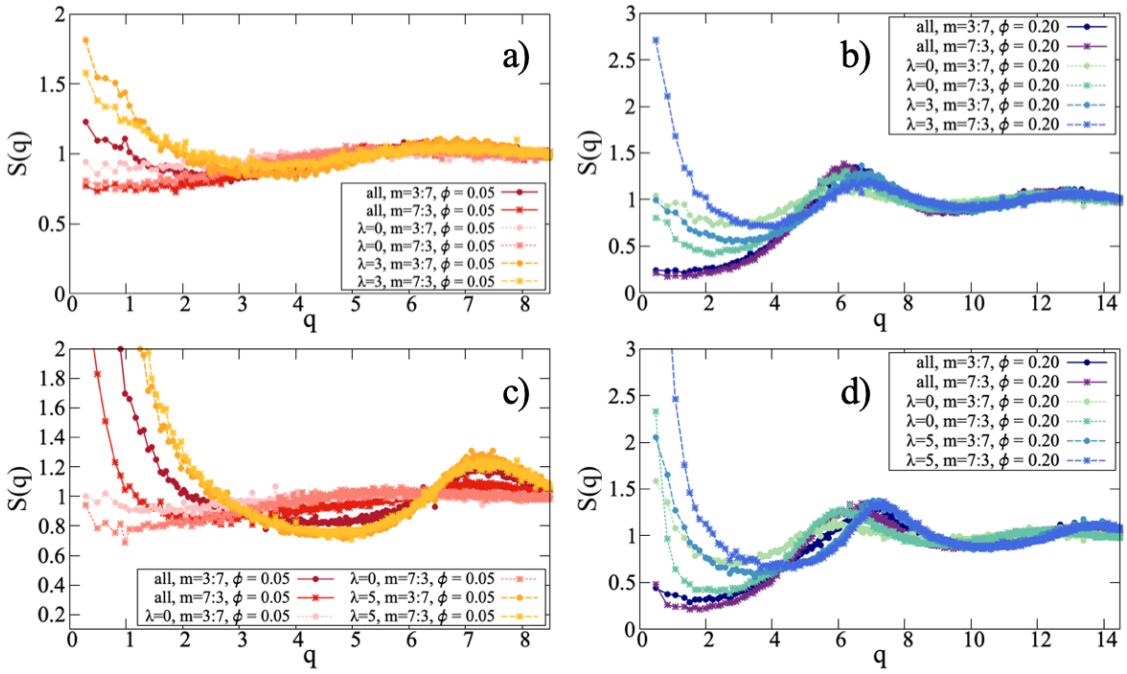

Figure 6.11: Structure factor $S(q)$ of soft spheres. Top row: $\lambda = 0:3$, at $\phi = 0.05$ (a) and $\phi = 0.20$ (b).The density ϕ determines the overall state of the fluid, while in the subtype $S(q)$, we can see the compressibility grow with the fraction of magnetic particles. Bottom row: $\lambda = 0:5$, at $\phi = 0.05$ (c) and $\phi = 0.20$ (d). For $\phi = 0.05$, the signature is clearly a gas containing some very magnetic particles, while $\phi = 0.02$ shows a classical fluid-like shape.

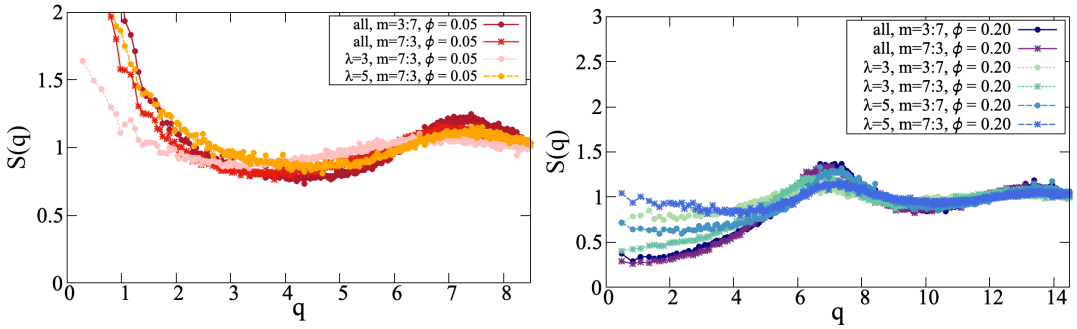

Figure 6.12: Structure factor $S(q)$ of spheres, with $\lambda = 3:5$ at $\phi = 0.05$ (left) and at $\phi = 0.20$ (right).

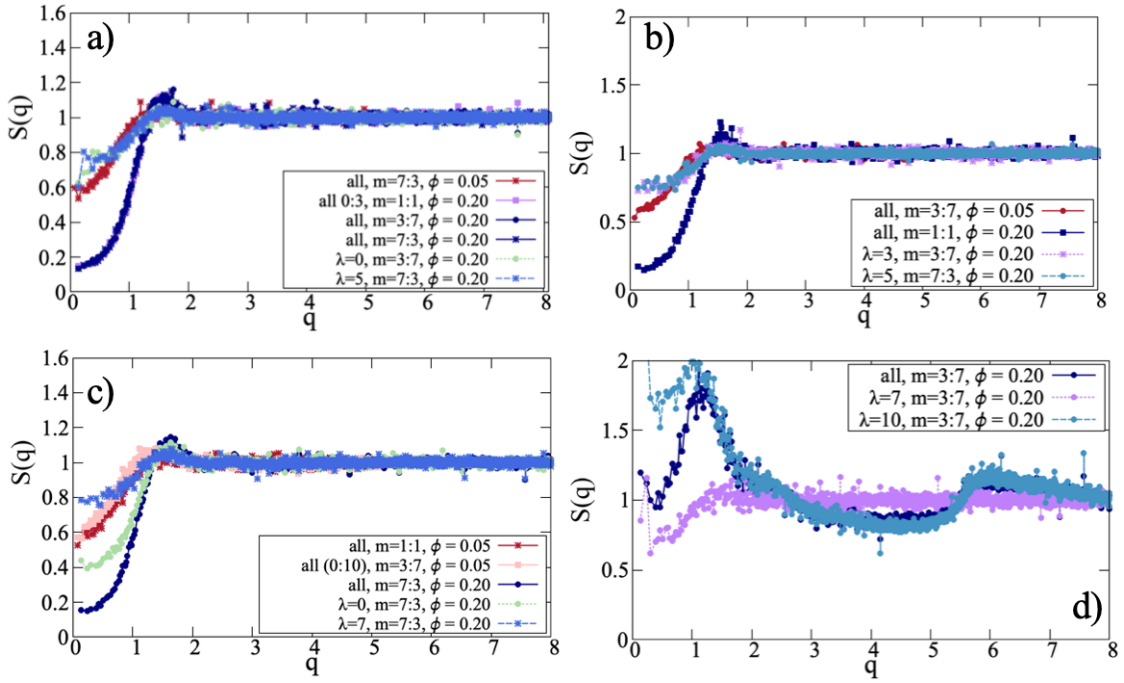

Figure 6.13: Structure factor $S(q)$ of aspect ratio 1 : 5 platelets, with $\lambda = 0:3,5$ (a), $\lambda = 3:5$(b), $\lambda = 0:7,10$ (c) and $\lambda = 7:10$ (d).

6.2.3 Initial Static Susceptibility

In order to understand the effects of the mixing on the magnetic response, we contrast first-degree modified mean-field theory with the initial static magnetic susceptibility of the mixtures in Figure 6.14. Since the volume fraction ϕ refers to the total volume of the particles in suspension, not purely the magnetic volume fraction, it is unsurprising that each set of three curves corresponding to different mix ratios is ordered by the fraction of magnetic particles. For $\lambda = 0:3$ mixtures, all of the curves lie below MMFT-1 theory, but appear to follow the same trend. By contrast, the $\lambda = 0:5$ almost coincides with MMFT-1 theory for the 3 : 7 mix ratio, and all $\lambda = 3:5$ mixtures are very similar to MMFT-1.

For platelets with aspect ratio 1 : 3, in Figure 6.15, we use Langevin and MMFT-2 for lower values of λ (left), as well as a platelet-modified chain model fit ($\kappa = 1.9$) for the highest λ on the right. For $\lambda = 0:3$, the more depletant-heavy mixes skew closer to the Langevin curve for $\lambda = 1$ (green), and the highest mixes fall below the Langevin curves for $\lambda = 3$ in a qualitatively similar way as for the sphere systems. For the $\lambda = 0:5$ mixtures, we see the same density sorting, but unlike the sphere case, the values still fall below Langevin predictions. The mix with the most magnetic particles, 3 : 7 (purple crosses), does exceed Langevin but clearly has a different functional form.

In the $\lambda = 3:5$ suspensions shown on the right side of Figure 6.15, we see much less difference

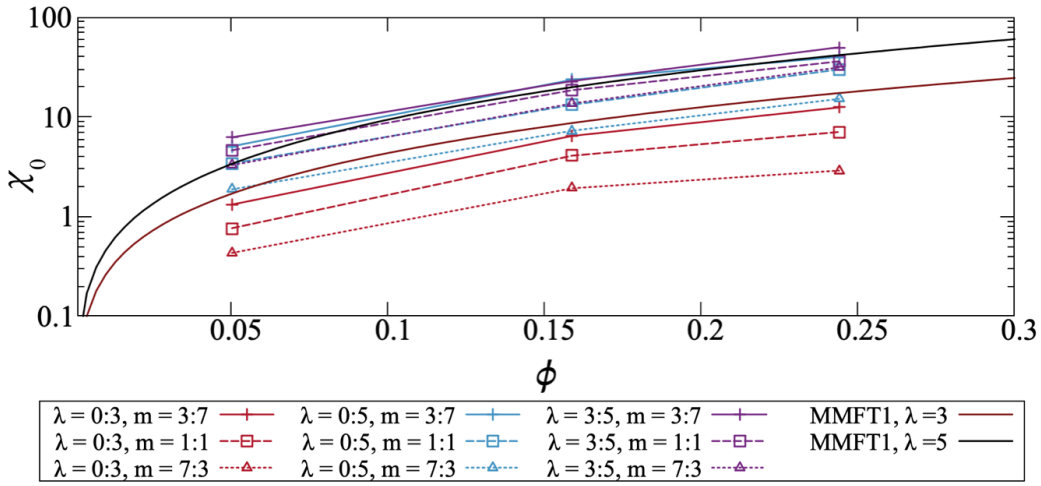

Figure 6.14: The initial static magnetic susceptibility of dipolar soft spheres mixes, contrasted with modified mean-field theory.

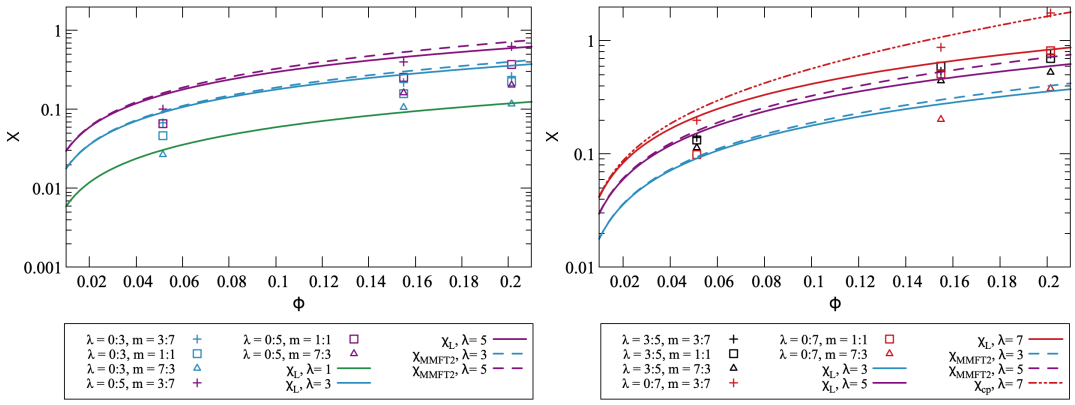

Figure 6.15: The initial static magnetic susceptibility of aspect ratio 1:3 mixes, contrasted with that theory.

between mix ratios, and we see a similar adherence to the $\lambda = 5$ MMFT2 curve as was displayed by spheres. The case for $\lambda = 0:7$ mixtures is far more interesting, showing a very strong dependence on mix ratio and a shape that is much more similar to the correlation-adjusted models. In this system, either few particles are magnetic at all, or the particles are very magnetic and exhibit strong clustering, driving up the value of χ.

Since equilibration issues made it difficult to gather sufficient statistics on at sufficient densities of high-λ platelets, we conclude this discussion with the limit case of $\lambda = 0:7$. For aspect ratio 1:5 platelets, the same equilibration issues meant that only few datapoints were available, which rendered comparisons largely ineffective. For this reason, they are not shown.

In summary, we can conclude that although the mixtures show lower magnetic susceptibilities than the fully magnetic systems, this difference is smaller than one might expect for magnetic to

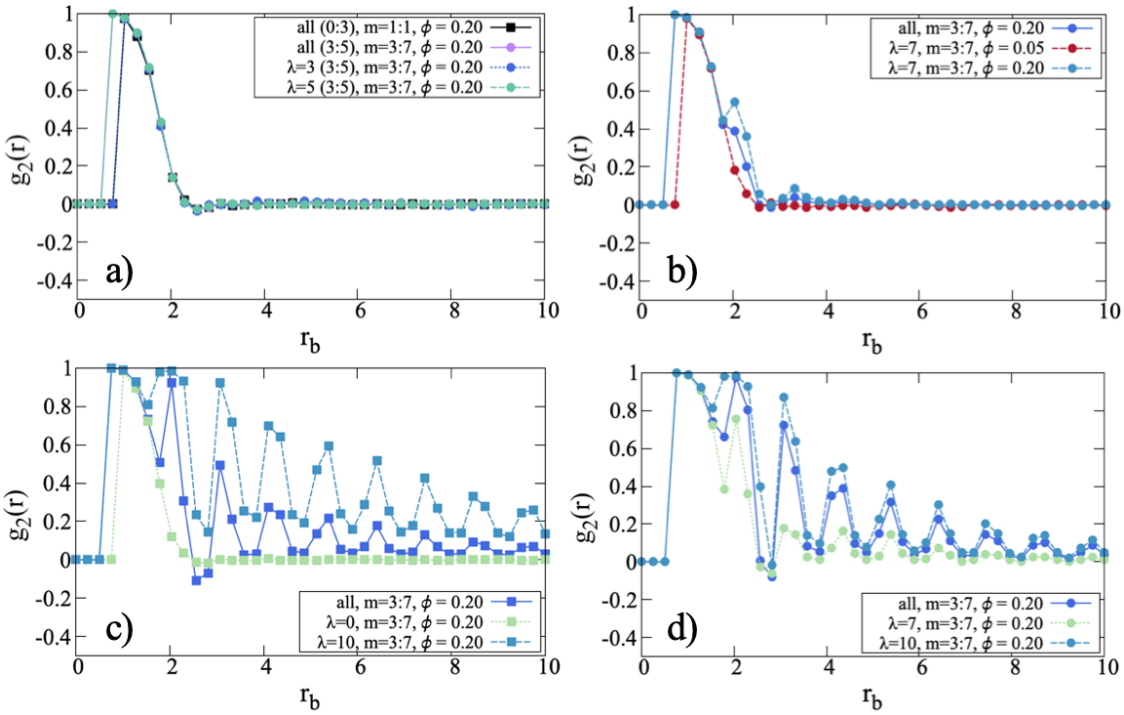

Figure 6.16: Orientational pair correlation function for aspect ratio 1:3 at low λ (left) and $\lambda = 0:7$ (right). We see some short-range order, and no long-range order.

magnetic mixtures. At higher λ, we see the signatures of aggregation for platelets despite the comparatively low overall value of χ.

6.2.4 Orientational Correlations

We now turn to the orientational pair correlations to explore the orientational ordering in more detail. This may go hand-in hand with self-assembly, or possibly be influenced by the shape. For depletants, the director is chosen to assess the orientation, as there is no dipole moment.

As in previous sections, we begin with aspect ratio $1:3$ platelets at varying λ, as shown in Figure 6.16. In the top row, there are only two behaviors observed: for any $\lambda = 0:3$ systems (a), or the majority of the others, the orientational correlations follow the black or blue curve shown in Figure 6.16 b): due to the shape, any particles at close range must be aligned. But once this distance is exceeded, the curve grows flat. The other variation, present for overall $\lambda = 3:5$ or the $\lambda = 5$ curves in $\lambda = 0:5$, only at $\phi = 0.2$ and majority-$\lambda = 5$ systems, shows an additional point at close range. This suggests that there could be self-assembly present in this system, as the particles must be at a distance less than or equal to 1 to be binned at this point. However, this effect might strongly be driven by density.

If we increase the values of λ to where clustering occurs for aspect ratio $1:3$ platelets, the

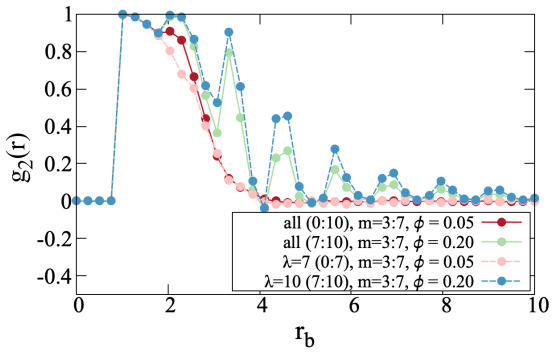

Figure 6.17: Orientational pair correlation function for aspect ratio 1:5 platelets.

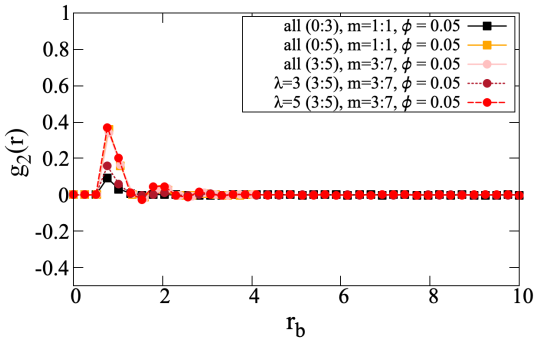

Figure 6.18: Orientational pair correlation function for spheres. We see some short-range order, and no long-range order. Orientational pair correlation function for aspect ratio 1:5 platelets.

results become much more interesting, which is why the subsequent results are split across multiple plots. In lower row of Figure 6.16, plot c) shows that for mixtures of depletants and $\lambda = 7$ platelets, there is a similar patterns as with $\lambda = 5$, with the lower volume fraction exhibiting one peak, and the higher volume fraction showing both some values at lower disances and an emergent nearest-neighbor peak at $r_b = 2$. For depletant and $\lambda = 10$ mixes, as shown in plot d), we see that while the depletants are forced to align at close range, the magnetic particles are now long-range orientationally ordered due to the self-assembly. In the cumulative function, we see a strong broadening due to the depletants present at intermediate distance with some degree of shape alignment. This is very similar to the purely magnetic mix, where we can observe these peaks for the lower λ platelets as well. To summarize, thus far mixes are even less orientationally correlated that depletant-free reference systems, except when self-assembly occurs.

For aspect ratio $1:5$ platelets, we condense the different results into one Figure 6.17. This is because for $\lambda < 7$, the only effect present is the short-ranged shape orientation correlations. For lower densities, this still holds in mixes with depletants. For $\lambda = 10$, we can see a second neighbor peak but no long-range order. For magnetic mixes, there are long-range signs of assembly and correlation. This is an interesting interplay of shape and magnetism, since there is a much less clear peak and valley structure, indicating less overall structure.

For dipolar spheres, shown in Figure 6.18, we see that there is only slight orientational correlation at close contact. For the $\lambda = 0:3$ mixes, it is effectively not present. For the mixes

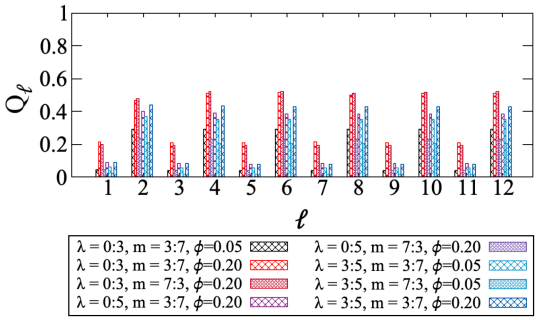

Figure 6.19: Steinhardt bond order parameters for spheres (left), showing a lack of crystalline order.

of $\lambda = 0:5$, the peak height is increased. It is important to note that, in contrast to previous chapters, the overall orientational correlations include depletants, which are oriented randomly. In the magnetic mixes, there are hints of a second peak near 2 for the $\lambda = 5$ spheres. This indicates the lack of clustering and lack of overall ordering. This reinforces the idea that the depletants reduce self-assembly, since the values are much lower than previously found. While the radial distribution functions were not very dissimilar qualitatively, the lack of orientational order is much more pronounced here.

6.2.5 Bond Order Parameters

Steinhardt bond order parameters have been used intensively in this thesis, due to the hope of finding some form of crystalline ordering. One slight drawback is that for them to be sufficiently accurate, a nearest-neighbor cutoff must be defined. This is more easily determined in more rigid structures, but slightly difficult for more fluid-like suspensions. This means that the absolute heights of the values here are subject to cutoff influence and should not be taken too seriously. These bond order parameters were calculated for the overall suspension, *i*.e. all particle types.

In the systems of dipolar spheres, shown in Figure 6.19 we see strong agreement with Chapter 4 both qualitatively and quantiatively. The height depends on the density, and exempting the highest density of $\lambda = 0:3$, on the magnetic mix ratio. Again, we see the lower odd and higher even value pattern, which is then smooth across the other values, suggesting no particular structure formation.

For aspect ratio 1:3 platelets at mixes with $\lambda \leq 5$, the bond-order parameters of suspensions at classical cutoffs are zero due to the lack of structuring. So we increase the cutoff, and increase λ, to showcase consistent trends. Then, as in Chapter 4, they show a pattern of equal, more pronounced heights at the even values. Overall, there is no true crystalline order. We do also see a concentration dependence on the depletants.

For aspect ratio 1:5, we again see the dependence on density and magnetic fraction. The one change from the basic odd-even pattern is the high Q_2 values at high densities, prompted by the chaining. This echoes a trend found in the previous chapter.

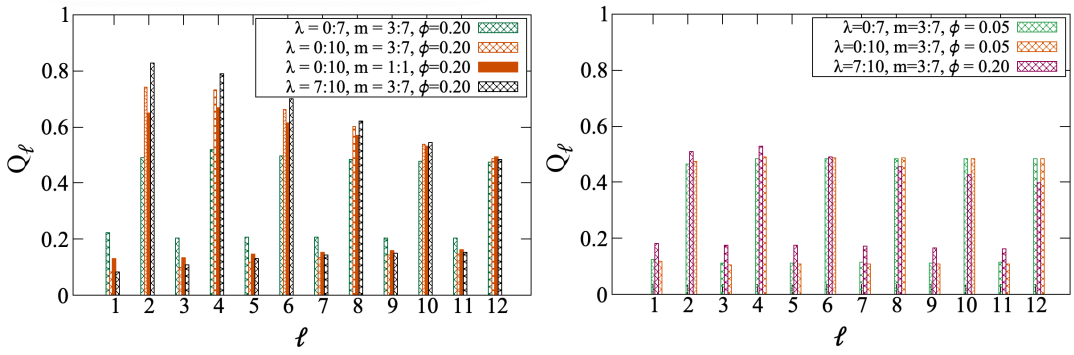

Figure 6.20: Steinhardt bond order parameters for aspect ratio 1:3 (left) and ratio 1:5 platelets (right), showing a lack of crystalline order but a slight signature of the self-assembly in the aspect ratio 1:3 case.

While it was interesting to explore different possibilities, the conclusion is that despite the depletant's presence, there is no underlying crystalline order on which any profound statements can be made.

6.2.6 Clustering

Firstly, in systems of reference spheres, we see the same trends as in Chapter 4. As a brief clarification note, these are a necessary reference since, as per our current definition of magnetic clustering, non-magnetic particles will not cluster as they cannot meet the energy criterion. For higher densities at $\lambda = 3$ there are already some false positives. Otherwise, the mix ratio of depletants serves as a form of secondary volume fraction control: clustering goes up with volume fraction and mix ratio, following the same trends as expected. Noticeably, the mixes of $\lambda = 3 : 5$ appear indistinguishable from lower volume fraction 0.5 mixes. Attempting to match these quantitatively is overzealous, since we know this clustering criterion overcounts. However, we can see that these show no additional effects as expected.

In the aspect ratio $1 : 3$ systems, shown in Figure 6.22 (top) we see that clustering does not begin properly until $\lambda = 0 : 7$ mixes. These bear an extremely strong resemblance to Figure 4.9 in Chapter 4, although with an additional dependence on the mix ratio and not just the volume fraction. Overall, we can see some stack formation for significantly high λ (orange, black), and the same peak subsiding into the slight presence of longer assemblies. We can basically conclude that for the magnetic particles, the clustering does not seem strongly affected by the presence of depletants, given sufficiently high λ. The one exception here is possibly $\lambda = 10$, as these configurations are typically not useable in the pure systems.

For aspect ratio $1 : 5$, all platelets in systems with $\lambda < 7$ show absolutely no signs of self-assembly. As shown in Figure 6.22 (bottom), in the systems with mixes including $\lambda = 7$, there are a few scattered clusters with increasing magnetic mix fraction and volume fraction, otherwise

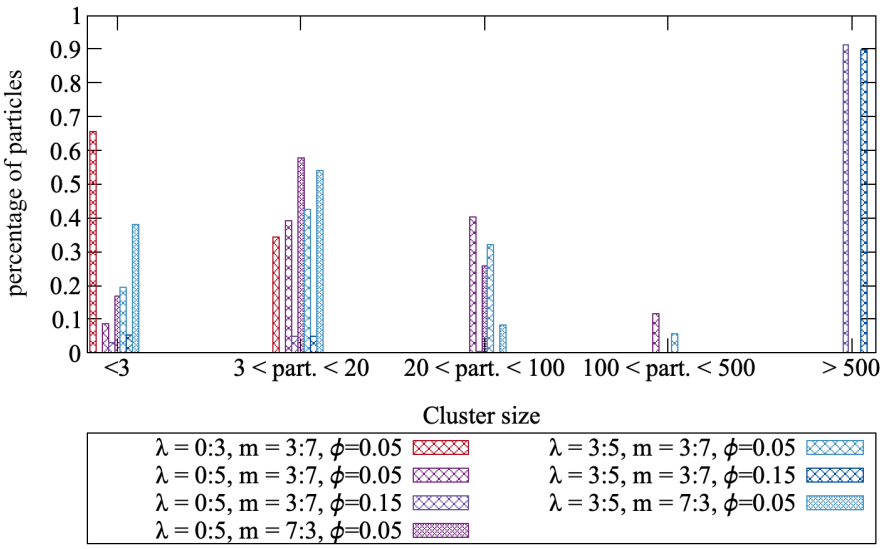

Figure 6.21: Cluster size distribution of dipolar sphere mixtures.

no assembly. The situation is similar for the equilibrated $\lambda = 10$ platelets at low volume fraction. Signficant clustering is not properly present until the purely magnetic mixtures of $\lambda = 7 : 10$, where the clustering also grows with the total volume fraction. However, the most dense, highest λ that could still be equilibrated shows significant clustering.

6.2.6.a Cluster Composition

One question at the outset of this section was the following: are there similar poisoning effects on the microstructure as found in binary mixtures of larger and smaller spheres? In this context, the poisoning would have to be related to the clustering. We can see that non-magnetic particles do not cluster, but are the less magnetic particles integrated into structure formation? Does having a weaker link hinder the further expansion of clusters? To this end, we select the clustered particles (those in an aggregate larger than two) and compute their number of bonds with other particles, as was used in Chapter 4 to characterize defects. These results are presented in Table 6.1.

We see that even in these systems that appear mostly aggregated, there is a signficant difference between the different types. Only half of the lower magnetic moment platelets are in such aggregates, while almost 90 percent are for the more magnetic particles.

Since dimers are excluded, and since we know that platelets almost exclusively form chains (up to statistical significance), we can further draw some conclusions about the average bonds for the platelet case. (Spheres form structures with many defects, therefore the numbers serve as reference, but the same reasoning does not apply). If a platelet has only one bond, it is the end of a chain. If the particle has two bonds, it represents a link in the chain. This means that if the average platelet has close to two bonds, it is more likely a link. If that number is closer to 1,

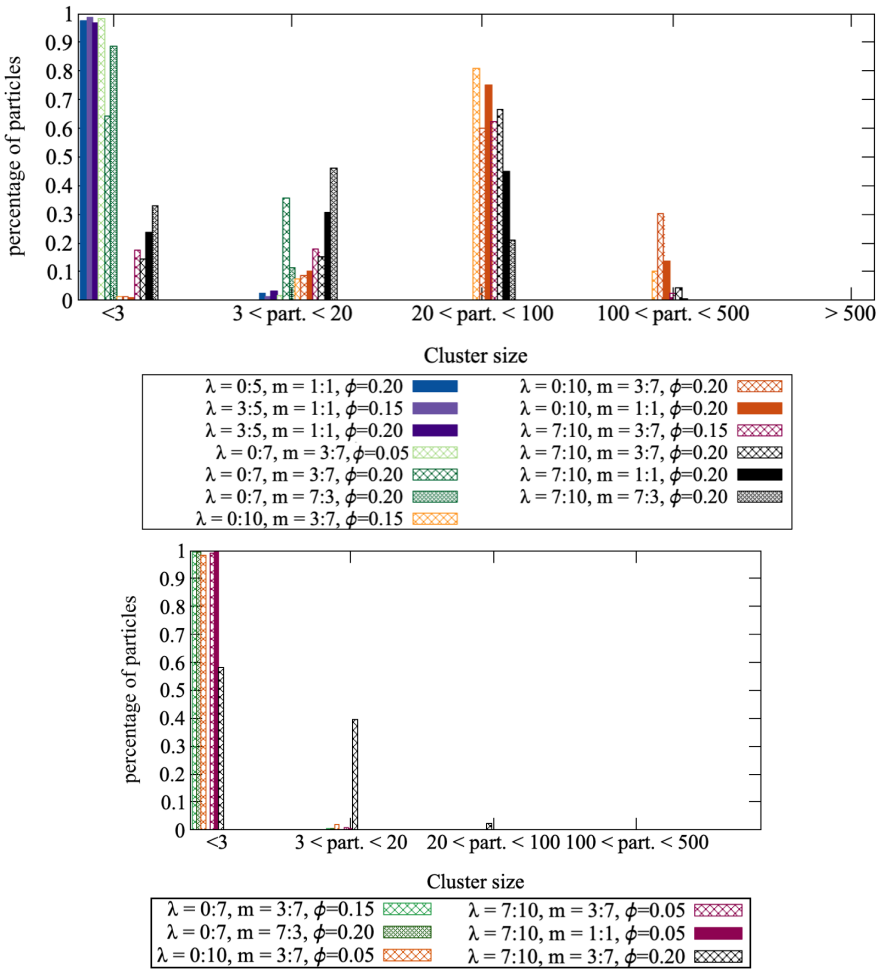

Figure 6.22: Top: Cluster size distribution for aspect ratio 1:3 platelets. Bottom: Cluster size distribution of aspect ratio 1:5 platelets. We can see little effects of clustering, up to high λ and densities.

AR	λ	mix	ϕ	p_{c_A}	p_{c_B}	$< b_A >$	$< b_B >$
1:1	$\lambda = 3:5$	3:7	$\phi = 0.05$	0.58	0.90	1.57	1.99
1:1	$\lambda = 3:5$	1:1	$\phi = 0.05$	0.55	0.88	1.58	1.99
1:1	$\lambda = 3:5$	7:3	$\phi = 0.05$	0.53	0.84	1.60	1.98
1:3	$\lambda = 7:10$	3:7	$\phi = 0.15$	0.43	0.98	1.70	1.92
1:3	$\lambda = 7:10$	3:7	$\phi = 0.20$	0.52	0.99	1.74	1.92
1:3	$\lambda = 7:10$	1:1	$\phi = 0.15$	0.43	0.97	1.64	1.89
1:3	$\lambda = 7:10$	1:1	$\phi = 0.20$	0.48	0.98	1.63	1.89
1:3	$\lambda = 7:10$	7:3	$\phi = 0.15$	0.33	0.94	1.52	1.86
1:3	$\lambda = 7:10$	7:3	$\phi = 0.20$	0.45	0.96	1.55	1.86
1:5	$\lambda = 7:10$	3:7	$\phi = 0.20$	0.12	0.59	1.38	1.65

Table 6.1: An overview of the percentage of clustered particles and average number of bonds for particles of type A (less magnetic) and type B (more magnetic)

then the platelets of this type are more likely to form the ends of chains. If the presence of more weakly magnetic particles disrupts the structures, we would expect them to predominantly form ends, while the more strongly magnetic particles should almost exclusively have two bonds. For spheres, the presence of defects will skew the statistics.

If we consider aspect ratio 1 : 3 florets, the difference between the two types is not very pronounced, with the average platelet having closer to two neighbors. This matches the idea that long chains are formed. The less magnetic particles are more likely to form an end than the more magnetic ones, but not by a wide margin. By contrast, the aspect ratio 1:5 platelets are more likely to form an end in any case, indicating shorter platelet stacks. The difference is also more significant here.

6.2.7 Phase Separation

Close consideration of some of the system's simulation snapshots leads to an interesting visual observation: when removing sections of particles, it appears as if certain snapshots have a separation between the different types of particles. This could mean that the system is undergoing a demixing or phase separation transition. For systems of dipolar ellipsoids, as will be shown in Section 6.2.8, high values of the magnetic coupling constant result in demixing as the magnetic ellipsoids separate from the nonmagnetic particles. One possible candidate system for a similar effect in platelet suspensions is shown in Figure 6.1. With all particles shown, the system appears completely mixed: if only one type is shown, there appear to be "holes" where the other type had been. But are these effects statistically significant?

A first indicator of where to look for such an effect are the radial distribution functions. Specifically, we would expect the radial distribution of particles of different types to assume lower values than those of the same types. In the radial distribution function analysis in Section 6.2.1, we clearly

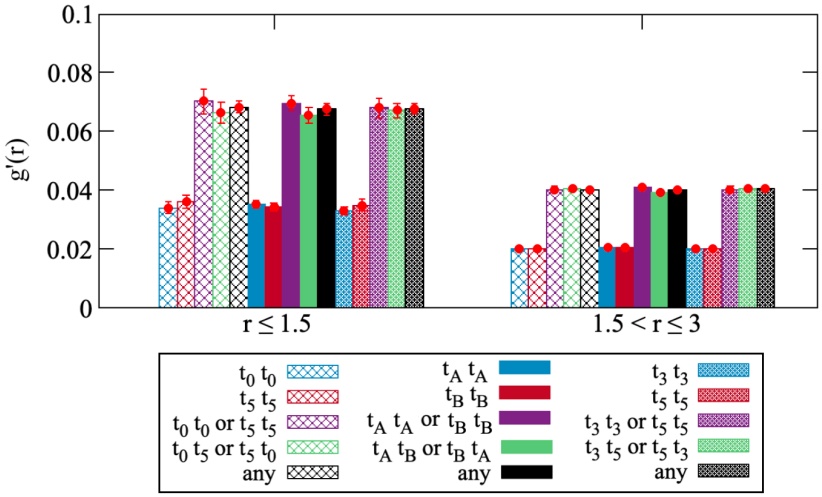

Figure 6.23: The first two values of a modified radial distribution function $g'(r)$ for a 50 : 50 mixtures of aspect ratio 1:3 platelets, with the three different systems $\lambda = 0:5$, random, $\lambda = 3:5$ indicated by different hatching styles. Blue and red bars indicate the amount of neighbors of the same type, while purple and green compare the sum of like-type neighbors to the sum of opposite-type neighbors. Error bars are shown in red. The figures shows that aside from low differences in the nearest-neighbors, particles have equal amounts of neighbors of different types.

saw that once self-assembly occurs, the magnetic platelets separate from the non-magnetic ones. At lower densities, the values of the cross-radial distribution functions lie between those for the same-particle ones, indicating a mixture. This means that the parameter range for a potential separation is intermediate values of λ. Therefore, in this section we will investigate platelet mixtures of aspect ratio 1:3, at $\lambda = 0:5$ and $\lambda = 3:5$.

Figure 6.23 revisits a variation of the radial distribution function, titled $g'(r)$, where particles of a given type are binned based on their minimal distance to particles of the same or different types, then normalized based on the bin size. This allows us to group a definition of near-neighbors and secondary neighbors. Secondly, here the distance is calculated, as in the clustering procedures, from any two simulation particle components, as opposed to the center to center radial distribution functions. This allows us to effectively consider the platelet anisotropy. The three different hatching styles indicate three different systems: firstly, the one with a 50:50 mixture of $\lambda = 0:5$ platelets at $\phi = 0.2$, secondly, a control system where particles of types A and B are placed randomly, and thirdly, a 50:50 mixture of $\lambda = 3:5$ platelets at $\phi = 0.2$. The results show no significant differences between the three systems beyond the nearest neighbors. While total like-type association seems to show a difference for the mixture of depletant and $\lambda = 5$ systems, this is unfortunately still within the range of the error bars.

While these results indicate that no significant demixing takes place, it can be argued that we have technically checked a different measure than we initially attempted to assess. Even an adjusted radial distribution function deals mainly with distances between particles, which in a

dense suspension may not be ideal to characterize the volume occupied by anisotropic particles. Our observations in the simulation snapshots lead to the conjuncture that different particle types could form small pockets. To test this, we first roughly determine particle clusters using a simplified clustering procedure with no energy interaction criterion (in order to include non-magnetic particles) and an increased central cutoff distance. For each cluster, the points representing the particle centers are assigned a Voronoi volume[192]. The objective then is to compare these systems to randomly generated configurations with no meaningful physics behind them, and see if the cluster size distribution is different.

The results of this procedure, applied to the $\lambda = 0:5$, $\lambda = 3:5$ and random control systems using a central cutoff of 1.4, are shown in Figure 6.24. Plot a) shows the number of proximity clusters of size c, titled N_c. We see that there's a straightforward exponential decay, which is identical for magnetic ($\lambda = 5$, red) and nonmagnetic ($\lambda = 0$, blue) particles. The inset shows the relative difference in cluster counts, for cluster sizes c with with $N_c > 2$, showing that these differences are very small. This includes a random configuration, shown in orange, which gives a reference for what variance to expect. The next three plots show the cluster size distribution, v_c. While we see that the two simulation results, shown in b) and d), have shapes distinct from the random configuration (c), there is no apparent meaningful distinction between the two.

The conclusion of this section is that for these instances, there does not appear to be a phase separation. In order to make a sweeping statement for a greater range of λ values, future inquiry could study this by methods such as thermodynamic integration.

6.2.8 Contrast to Ellipsoids

To expand our understanding of the role of anisotropy in binary mixes, we contrast these results with dipolar ellipsoids. While this section is extensive in the planned publication, the simulations were carried out by collaborators, which is why the results are only briefly mentioned here.

The most important difference to keep in mind is that for ellipsoids, the minimum of the dipolar interaction changes from head to tail to the antiparallel alignment[193]. This means that instead of chains of oriented particles, the ellipsoids form antiparallel pairs, which later extend into a form of twisted chains with the ends of the particles pointed out.

For $\lambda = 3$, the systems behave similar to the platelet case. The particles are visually disordered. They have slightly higher signs of some pair formation in their radial distribution function based on the nearest-neighbor peak, more for mixtures, but not enough to point to much assembly, and both the structure factor and g_r show no long-range structure or orientational ordering. There is no visual indication of demixing.

For aspect ratio 1 : 3, an increase to $\lambda = 10$ leads to the formation of lattices as shown in Figure 6.25. There can be multiple or just a few such lattices formed: they have a signature of periodic

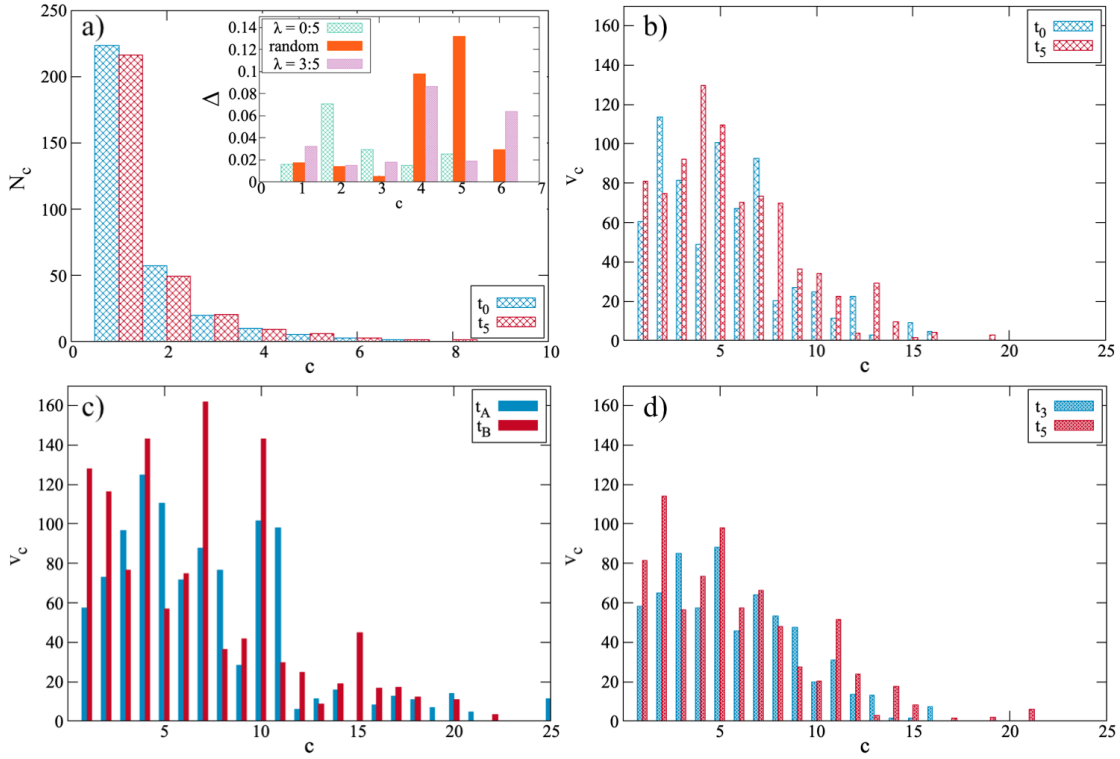

Figure 6.24: Figure a): the number N_c of platelets in proximity clusters of size c (measure including steric platelets), for $\lambda = 0:5$. We see an exponential decay: the inset shows relative differences, comparing between systems of $\lambda = 0:5$, a random control and $\lambda = 3:5$. The remaining three plots show the averaged volumes v_c of the clusters of size c (b) $\lambda = 0:5$, c) random control, d) $\lambda = 3:5$). We can see that the actual simulation results show a different distribution from the random system, but the two do not show markedly different trends.

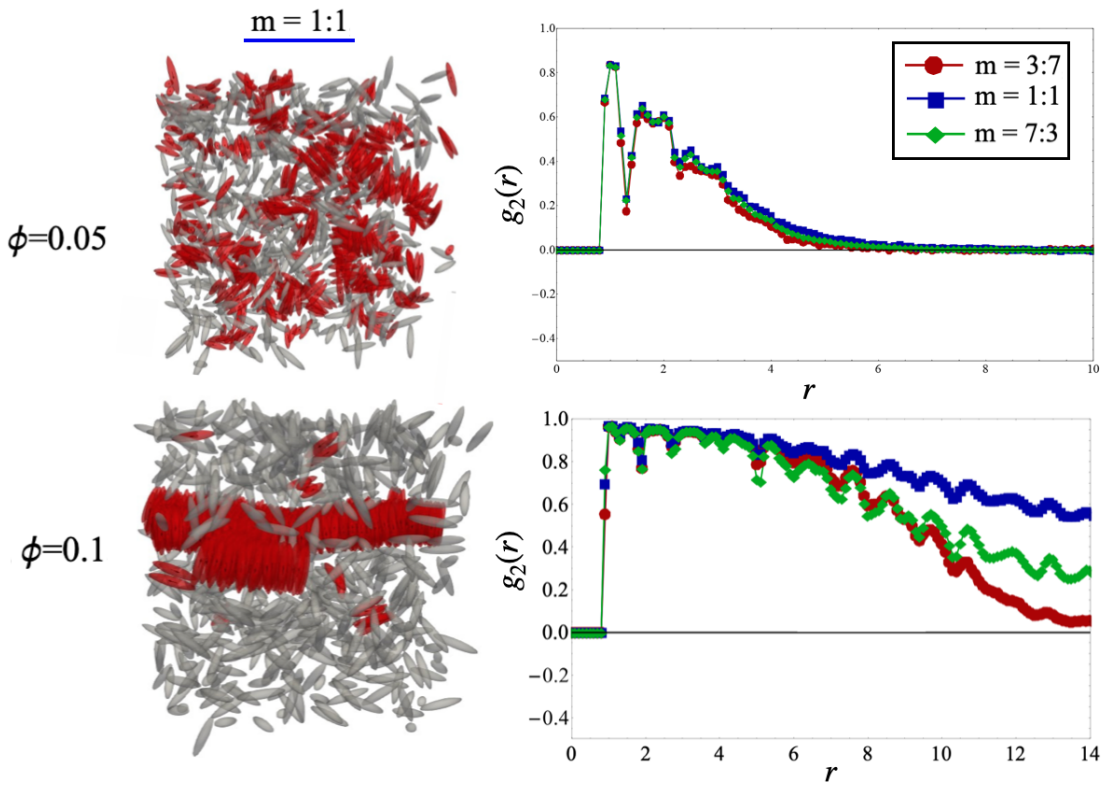

Figure 6.25: A collection of results for anisotropy 5:1 dipolar ellipsoid (dark red) and depletant (grey) mixtures at $\lambda = 10$. The height of the orientational correlations on the lower right depends on the number of large assemblages.

peaks in the radial distribution function which are mirrored in the structure factor. The signature in the $g_2(r)$ is also interesting. While obviously the self-assembled particles are highly aligned, they lack the corresponding dips between the peaks present for platelets (or assembled spheres). This comes from the lattice: instead of the two neighbors present for chained spheres or platelets, a particle in the lattice has approximately four neighbors at minimum distance and four more at the diagonal minimum of $\sqrt{2}$, or similar depending on the lattice formed. These neighbors then repeat periodically. The shape also blocks out closer range neighbors over or under the lattice.

For aspect ratio 1 : 5, the microstructure for $\lambda = 10$ depends more strongly on the volume fraction. At $\phi = 0.05$, the particles self-assemble into twisted chains with a high degree of flexibility. These microstructural motifs manifest as a few peaks in the radial distribution function and structure factor, as well as a unique $g_2(r)$ shown in Figure 6.25. At $\phi = 0.1$, there are two options: purely magnetic systems continue to form some twisted chains, and some smaller lattices depending on the volume fraction. If depletants are present, the magnetic particles form lattices. This is born out by the change in signature of the orientational order and the structure factor. This suggests that the key reason for the change from less orientationally ordered structures to these lattices is volume fraction, and this is boosted by depletants.

While the smaller aggregates show no sign of demixing, the lattices clearly do. Checking the radial distribution and structure factors of the non-magnetic particles, we do no see and signs of induced structuring. This is also clear from the renders. Regarding the initial susceptibilities, unlike platelets, the antiparallel alignment of ellipsoids makes the resulting suspensions much less susceptible. This was already shown in previous work[193].

6.3 Conclusions

This Chapter investigated the effects particle mixtures, specifically depletants and less magnetic particles. As expected, we found signs of self-assembly at lower values of the magnetic coupling constant λ for platelets and spheres. While there were some subtle indications that, in the case of platelets, there might be a separation between particle types at intermediate values of λ, these did not hold up to rigorous analysis: a further study would be needed, such as thermal integrations, that could span different coupling constant mixtures. At the limit of magnetic and non-magnetic particles, the self-assembly resulted in demixing for platelets and ellipsoids.

In the magnetic mixtures of platelets, the less magnetic particles were largely integrated into the magnetic clusters without seeming to inhibit cluster formation. They did form fewer bonds on average when aggregated, and were less likely to aggregate, but did not inhibit chain formation.

In brief, the addition of depletants below the self-assembly threshold served to promote but not alter the effects expected of higher density and concentration magnetic particles for platelets. At higher values of λ, demixing occurs. However, some of the particles having a lower magnetic moment did not seem to qualitatively affect the self-assembly in magnetic mixtures. It seems that the addition of depletants is, therefore, not likely to be a signficant cause of qualitative changes in suspension behavior.

6.4 Methods

6.4.1 Simulation protocol

As in previous chapters, the results in this section were obtained by Molecular Dynamics simulations, using versions of ESPResSo 4.1.x[121]. The simulation protocol was the same as used in Chapter 4. In brief, a Langevin thermostat, $N = 1024$ particle centers, periodic boundary conditions and both the platelet models and volume fraction calculations as previously described. In order to match the proportions used in the ellipsoid simulation data, the mix ratio of 3 : 7 was taken to mean 307 particles of type 1 and 717 particles of type 2. For the inverted ratio of 7 : 3, there were 308 particles of type 2 and 716 particles of type 1. For the mix ratio of 1 : 1, there were 512 particles of each type.

Simulations were run for aspect ratios $1:1$, $1:3$ and $1:5$, with densities of $\phi = 0.05, 0.15, 0.2$. The same time-step and warm-up protocol as in Chapter 4 were used. As in that section, there were issues with the equilibration of the high-density and high magnetic moment simulations. In some cases, the equilibration threshold needed to be moved from $10000\delta t$ to $40000\delta t$, others could not be properly equilibrated and are only mentioned as qualitative limit cases. These frequently consisted of platelets with high magnetic moments, which rapidly formed chains approaching the lengths that could result in self-interaction through the periodic boundary conditions. These were removed, regardless of the energy values.

The analysis scripts are the same as in previous Chapters, with the exception of the new phase separation criterion.

6.4.2 Phase Separation

Two new measures were introduced in the phase separation subsection. Firstly, the adapted radial distribution function $g'(r)$. The difference between this and a classical radial distribution function is the redefinition of distance to be calculated between any two platelet simulation particle centers, as introduced in Chapter 4. The normalization was carried out by via the number of particles, as well as the volume of the spherical bin shells. This is slightly inelegant as the distances matched to the same center are not technically always measured from the same center. This is effective for the cause, but suboptimal for general use.

The Voronoi volumes were computed using Freud. In principle, a Voronoi volume is a way of partitioning a larger volume into smaller ones by its proximity to a set of seeds. In this case, the seeds were taken as all the raspberry particle centers, and the volumes of all the different seeds belonging to the same cluster were added together to obtain the total volume assigned to the cluster.

7 - Phase and Particles

While the previous chapters have focused on larger, mostly collaborative projects that made sweeping statements on the suspensions as a whole, this thesis work also included more constrained lines of inquiry grouped around painting a more detailed picture of the interactions and phase behavior of the colloids. This chapter presents three such smaller projects. Firstly, an exploration of the steric simulation model colloidal platelets' isotropic to nematic transition in absence of an external field. This is interesting to observe and document for the model, but would require a more accurate and computationally efficient model for the long-ranged interactions present in the system. Therefore, the next two subsections present an alternative to the point dipole model and its implications, and an exploration of the electrostatic interactions between platelets of various sizes and distances. Although the results in this chapter are not sufficient for publication on their own, they resolve certain loose ends and provide a jumping-off point for future projects, some of which are already in progress.

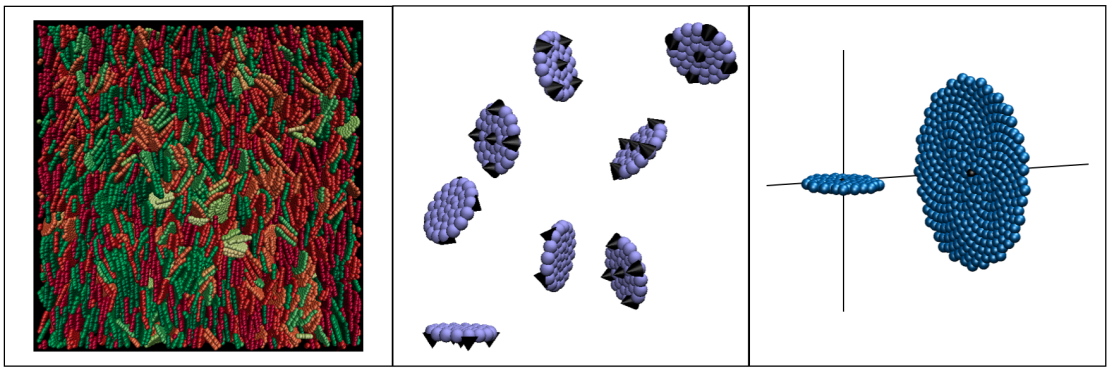

Figure 7.1: Left: Simulation render of a dense ($\phi^* = 0.55$) suspension of $N = 10000$ steric nanoplatelets, colored based on their angle to the oriented z-axis; light colored are less aligned, dark colors have a director close to parallel to the nematic axis. This was developped based on the need for symmetry breaking in a system of magnetic nematics. Center: Simulation render of platelet with a dsitrbuted dipople moment. Each black arrow denotes a magnetic interactions site. Right: A medium sized and a large platelet with charged surfaces, aligned and positioned to measure the potential of mean force at a specific distance and angle.

The material in this chapter is unpublished, but has been featured in multiple talks and poster presentations.

7.1 Phase Behavior

Although the focus of this thesis has been on the isotropic phase, the phase transition and subsequent nematic phase of magnetic platelets are appealing targets for in-depth simulation studies. In order to potentially explore these regions of the phase diagram, we first need to establish a baseline for the model and system. Research on colloidal cut-spheres has shown as the exact shape of the discotic particles used can affect the transition point and resulting structure[122]. We therefore begin by simulating aspect ratio 1:10 platelets with purely steric interactions. To match the literature, we use the reduced volume fraction $\phi^* = \phi/\phi_{cp}$, where[54]:

$$\phi_{cp} = \frac{2d}{\sqrt{3-d^{-2}}} \tag{7.1}$$

and calculate the order parameter S for increasing ϕ^*. This is shown in Figure 7.2. In this instance, the order parameter S is calculated between the nematic director axis and the particle's director. Since these are steric platelets, the symmetry under sign inversion is not a concern.

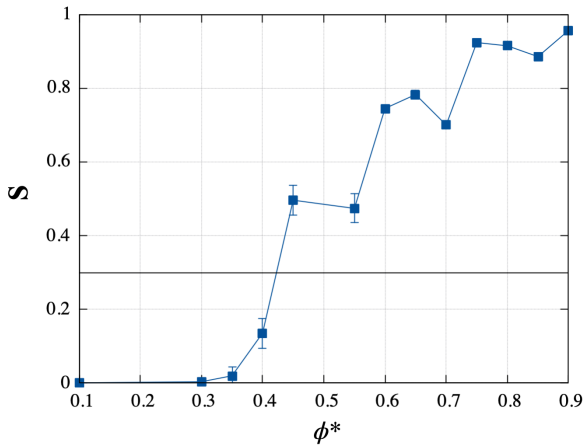

Figure 7.2: The evolution of the order parameter S with increasing normalized volume fraction ϕ^*, with the threshold value of $S = 0.3$ marked in black. We observe a belated onset of the phase transition, as well as discontinuities which we attribute to defects in the nematic order.

This plot allows us to draw several conclusions about the system. Firstly, the onset of nematic ordering at over $\phi^* = 0.4$ is markedly higher than the literature (which would lead us to expect $\phi^* = 0.3$[54]). Such effects are not uncommon between different models, but it is important to note the discrepancy when trying to make comparisons. Secondly, although the error bars are rather small, the underlying data has limitations. The basic methodology of Molecular Dynamics is not particularly well-suited to exploring phase transitions. These results are from Molecular Dynamics runs of $N = 10000$ platelets, which is a small system by liquid crystalline standards. Since for higher values of ϕ^*, the particles needed to be place on a starting grid to allow for equilibration, this could trap the system in a local energy minimum. For a full study, this would need to be carefully checked and corrected for, which should then result in a smooth curve. However, based on this example, we can explore some qualitative properties. Having taken this caveat, aside from

the basic statistical limitations, why is the order parameter so discontinuous?

The answer lies in the domain structure of the particles. As discussed in Chapter 2, there are differences between magnetic and liquid crystalline domains. For the sake for this simplified investigation, we are interested in differentiating subsets of particle which are orientationally aligned as a proxy for domain structure. Therefore, we generate a domain classification based on two rules: firstly, two particles are in the same domain if their center to center separation is lesser than one particle diameter, and if their pairwise orientational correlation parameter is greater than 0.95. Secondly, domain membership is transitive. As shown in Figure 7.3, this suffices to explore the different aligned subregions of the simulation box. On the left, we see the average number of domains n_D containing n_p particles. For $\phi^* = 0.3$, where the order parameter is still effectively nil, there are only a few pockets with ten or less aligned particles. Increasing the volume fraction initially increases n_D, which then trends towards the increase of the size of the domains (as measured by an increase in the particles in them, n_p). From $\phi^* = 0.55$ on, we also see the formation of few, large domains. This is shown in more detail by the inset. To track this evolution, the right plot shows the evolution of certain domain sizes. For simplicity, the simulation particles are classified as either not belonging to any domain (less than 10 particles), belonging to a "pre-domain" (or tactoid-like region) with $10-100$ particles, belonging to a domain of $101-1000$ particles or a "mega-domain" of 1001 or more particles. We see that as the order parameter begins to grow ($\phi^* = 0.4$), the pre-domain alignments peak. These then rapidly drop in favor of the growing domains and "mega-domains". This latter classification is not meant to represent an absolute physical number, as it is based on the number of platelets in simulation.

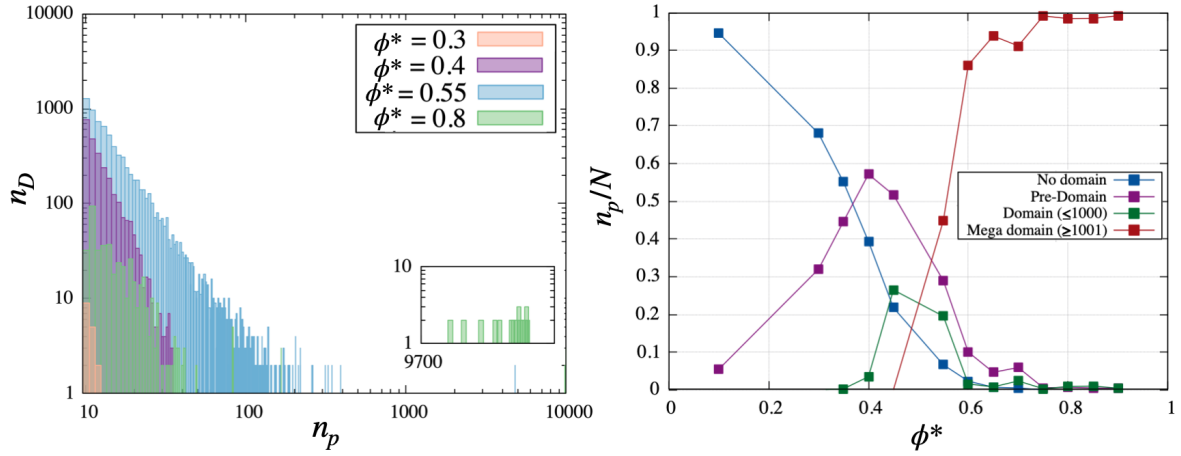

Figure 7.3: The evolution of the order parameter S with increasing normalized volume fraction ϕ^*, with the threshold value of $S = 0.3$ marked in black. We observe a belated onset of the phase transition, as well as discontinuities which we attribute to defects in the nematic order.

This phase diagram, based on domains, illustrates two interesting aspects: firstly, it indicates that it may be possible to study the domains and defect structure despite the limits on box and

particle size. For low enough ϕ^*, we can stabilize several of them. This also indicates that it would be possible to study the transition from tactoids or aligned stacks as found for dipolar platelets, and possibly shed some light on this process. To bring this section to a close, we take a brief visual look at the defects present at the coexistence of different sizes, $\phi^* = 0.55$, in Figure 7.4.

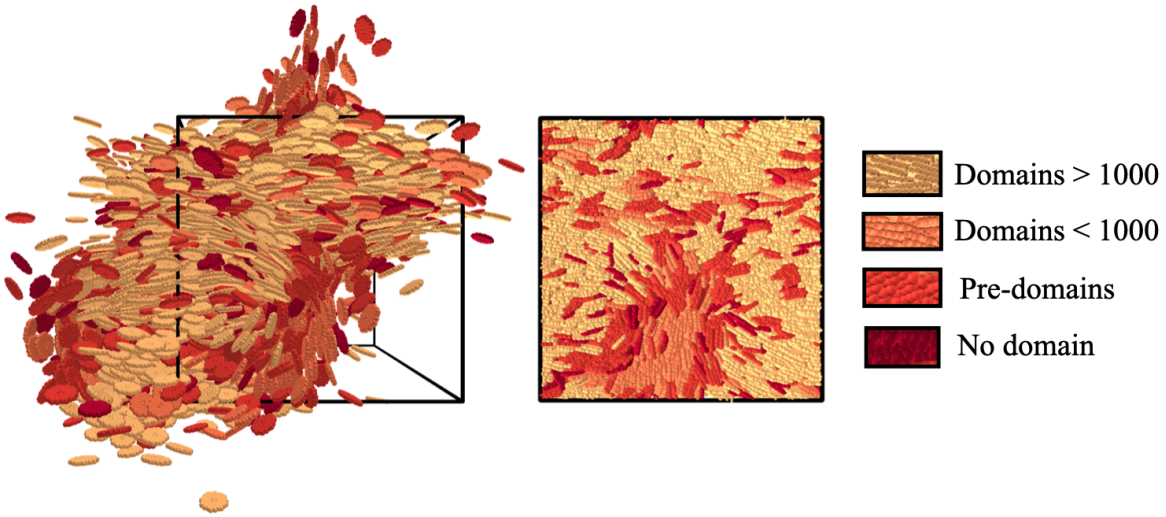

Figure 7.4: A simulation rendering at $\phi^* = 0.55$. The left render shows the unfolded coordinates, making it easier to see the director alignment of the platelet. Colors denote what scale of domain the particles are contained in, with the yellow large domain consisting of almost half the particles present.

We can see that the majority of misaligned particles are forming a boundary around a smaller domain at the bottom center. In order to classify defects properly, we would need to look at the director evolution. However, at this point there are more relevant questions. Specifically, the evolution of these domains is slow. To systematically study these phenomena with, many configurations would need to be sampled for each density to ensure accuracy. Moreover, the starting lattices would need to be varied. For some higher densities, the current starting lattice was chosen with half the box aligned in one direction, and the other stacked orthogonally. This could be artificially biasing towards domain formation.

Such situations could be resolved by the use of parallel tempering, where different copies of the system at slightly different temperatures are equilibrated, then swapped based on a probability criterion calculated from their energy difference. This should avoid the system getting stuck in local energetic minima. For this approach, there are two remaining caveats: firstly, this will not eliminate the need for a large system. Secondly, running these replicas of large systems in parallel is computationally demanding. Since the pure steric systems described here are already well-studied, any simulation to be run on this system will need at least magneto- and presumeably electrostatics, adding costly long-range interactions. These would need to be highly accurate in order to generate the proper phase transitions at the low densities seen in experiment. In Chapter 3, we observed

that, despite being not far below the nematic threshold, the electrostatics did not seem to result in long-range ordering. In Chapter 4, we saw that the point-dipole mode, while yielding promising correspondence with experiment in terms magnetic terms, results in less self-assembly than for spherical particles at the corresponding values of λ. It might not be particularly accurate for large aspect ratio platelets. For the transition studies, we would exclusively study large aspect ratio platelets by definition. In brief, in order to perform an interesting study of this region of the phase diagram that does not overlap with existing work, and that matches experiment well, new models of the particle interactions are needed. The remainder of this chapter will present some results on these interactions, as well as potential model extensions, and summarize the state of current results so that future work could successfully revisit the topic.

7.2 Distributed Dipoles

Throughout this thesis, we have maintained the point-dipole model for our colloidal particle. This has numerous reasons: for one, it must hold at long distances. Moreover, it has been effective for the study of other shape-anisotropic colloids such as cubes and ellipsoids, and also was the model of choice for studies of Gay-Berne discotic particles with electric dipoles. It also allows direct comparison to much of magnetic soft matter theory, which presumes point dipoles. However, as we noted in Section 2.1.2.a, some quadrupolar forces were present in the original (anisotropic carrier) liquid crystals, which appeared to be necessary for the stabilization of the nematic phase. Recent studies have also suggested that a model with a more distributed dipolar potential is necessary to capture the phase behavior. It can be conjectured that the phase transition requires this quadrupolar potential as opposed to a dipolar one, since the transition can be achieved in absence of the liquid crystal carrier medium. Additionally, our use of the point-dipole model could in the self-assembly studies in Chapter 4 could artificially penalize the shifted antiparallel alignment of dipoles that would otherwise be more attractive. This means it could be affecting the clustering. In this section, we investigate how best to place multiple dipoles on the platelets, and mark some outcomes.

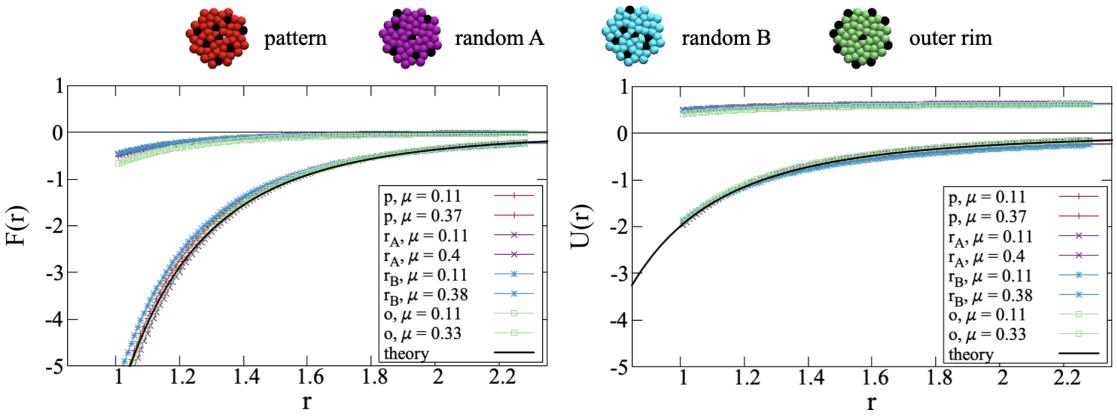

Figure 7.5: The dipolar forces and potential of mean force calculated for four different arrangements of distributed dipoles on the platelet model surface for aspect ratio 1:7 and a target interaction strength of $\lambda = 1$.

Firstly, we need to decide where to place the dipoles. Figure 7.5 shows a study of the forces (left) and the potential of mean force (right) for pairs of platelets with the dipole placements indicated above. The tests reveal that for the examples studied, the placement does not dramatically affect the overall potential. In general, we see that the overall shape of the potential is still conserved. However, splitting a dipole moment of μ between n particles via simple division results in much weaker interactions. While for the short range of these interactions, the original potential can be recaptured by increasing the dipole moment, this means there will be a mismatch at greater distances since the total magnetic moment of the platelet is greater.

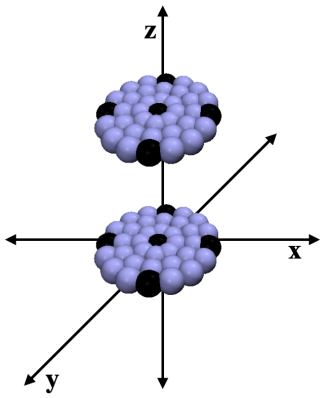

Figure 7.6: An illustration of the aspect 1:5 ratio platelets, of which the interaction potential is calculated in the text. The black spheres indicate dipole moments. Since the point dipole is placed in the center of the raspberry sphere, the radial distance of any given black sphere (except the central ones) are equal to $s = 2$ and not $s = 2.5$.

Where does this mismatch come from? Let us compare the interaction between two platelets aligned head to tail as in Figure 7.6. We will fix one platelet in the origin of the coordinate system, with the second platelets moving along the z axis. The magnetic dipole moments are parallel to the z-axis, positioned on the black spheres, and have dipole moment $\mu = \sqrt{\lambda}/n(0,0,1)$. In this example, $n = 5$ and the radial distance of the black sites $s = 2$. Given this coordinate system and particle positioning, we can simplify the generic point dipole potential to read:

$$U_{dd}(\vec{r}) = \frac{\lambda}{|\vec{r}|^3}\left(1 - \frac{3r_z^2}{|\vec{r}|^2}\right) \tag{7.2}$$

for the interaction between each pair of dipoles, where $\vec{r} = (r_x, r_y, r_z)$ is the separation between the pair of point dipoles. In the case where two point dipoles are aligned head-to-tail, the vector $\vec{r} = (0,0,1)$ and the expression reduces to $U_{dd}((0,0,1)) = -2\lambda$. Let us now contrast this with the total interaction potential energy between two platelets with the dipoles distributed as in Figure 7.6, each with a magnetic moment of $\mu = \sqrt{\lambda}/5 \cdot (0,0,1)$. For the central point dipole, the interaction is the sum of the perfectly aligned central dipole, as well as four other dipoles which have a radial distance of $s = 2$ in from the central dipole in the xy plane. This means that the sum of interactions with the central particle is

$$U_c = -2\frac{\lambda}{5} + 4 \cdot \left(\frac{\lambda}{5(2^2+1^2)^{3/2}}\left(1 - \frac{3 \cdot 1^2}{(2^2+1^2)}\right)\right) = -\frac{2\lambda}{5} + 4\frac{2\lambda}{5^{7/2}} = \frac{2\lambda}{5}\left(-1 + \frac{4}{5^{5/2}}\right) \tag{7.3}$$

To get the total interaction, we still need to consider the interaction between the four dipole moments placed on the surface U_s. In this model, by symmetry it suffices to consider one. We will again have one perfectly aligned dipole, with four remaining. Without loss of generality, we choose the leftmost dipole on the $-x$ axis. This has the separation vectors $(s,0,1), (2s,0,1), (s,s,1)$ and $(s,-s,1)$, which gives us

$$U_s = -2\frac{\lambda}{5} + \frac{2\lambda}{5^{7/2}} + \frac{\lambda}{5(4^2+1^2)^{3/2}}\left(1 - \frac{3}{(4^2+1^2)}\right) + 2\cdot\frac{\lambda}{5(2\cdot 2^2+1^2)^{3/2}}\left(1 - \frac{3}{(2\cdot 2^2+1^2)}\right) \tag{7.4}$$

$$= \frac{2\lambda}{5}\left(-1 + \frac{1}{5^{5/2}} + \frac{7}{17^{5/2}} + \frac{2}{3^4}\right) \tag{7.5}$$

Adding all of these interaction terms, the total interaction potential between these platelets is:

$$U_t = \frac{2\lambda}{5}\left(-1 + \frac{4}{5^{5/2}}\right) + 4\cdot\frac{2\lambda}{5}\left(-1 + \frac{1}{5^{5/2}} + \frac{7}{17^{5/2}} + \frac{2}{3^4}\right) \tag{7.6}$$

For example, if $\lambda = 1$, the resulting $U_t \approx -1.89$ instead of 2. While this loss is not dramatic, we see that it scales with the number and proximity of distinct dipoles used. The more pronounced effects of this process are shown by measuring the forces between particles in Figure 7.7. In these plots, the aspect ratio 1:5 and platelet model are chosen as before, but the number of dipoles is varied from a single, central point dipole to the distribution shown in Figure 7.6 to placing a dipole moment on every single raspberry sphere (37 total). In these examples, $\lambda = 5$. On the top left, which is the same force measured for aspect ratio 1:7 and $\lambda = 1$ in Figure 7.5, we see a similar decrease in attraction, which grows with the number of particles. In contrast, the side-to-side repulsion shown on the top right is much higher for the distributed model, since it has dipoles close to the edge that are in energetically disadvantageous, parallel to each-other configurations. This repulsion is decreased again for high amounts of dipoles. The bottom row explores the shifted configuration, which was mentioned as a potential facilitator of self-assembly. In this case, shifted means that one platelet is fixed, while the other is moved closer along the x-axis at height $z = \sigma = 1$. For the single central sphere, we see that the interaction is zero until $r_x = 2$, which is already significant overlap. In the distributed model, the attraction oscillates depending on the local alignment of the dipoles. This means that although there is an attraction at greater distances, there is also a slight repulsion in locations that depend on the dipole placement. If we attempt to go to the limit of every particle having a dipole moment to avoid these artificial inhomogenities, we obtain the plot on the lower right. While the values are low for this choice of λ, we see a repulsion in z-direction near the platelet edge. This means that instead of facilitating self-assembly, the repulsion of the cross-terms would presumably outweigh the additional attraction in most scenarios. If such a high number of dipoles is used, this would result in a non-dipolar interaction, at least at short-range.

While these outcomes are interesting, it is important to note that the actual magnetization of the platelets is not known in full detail. In order to construct a realistic model, some micromagnetics simulations would be needed to understand the actual magnetization of the particle, then choose

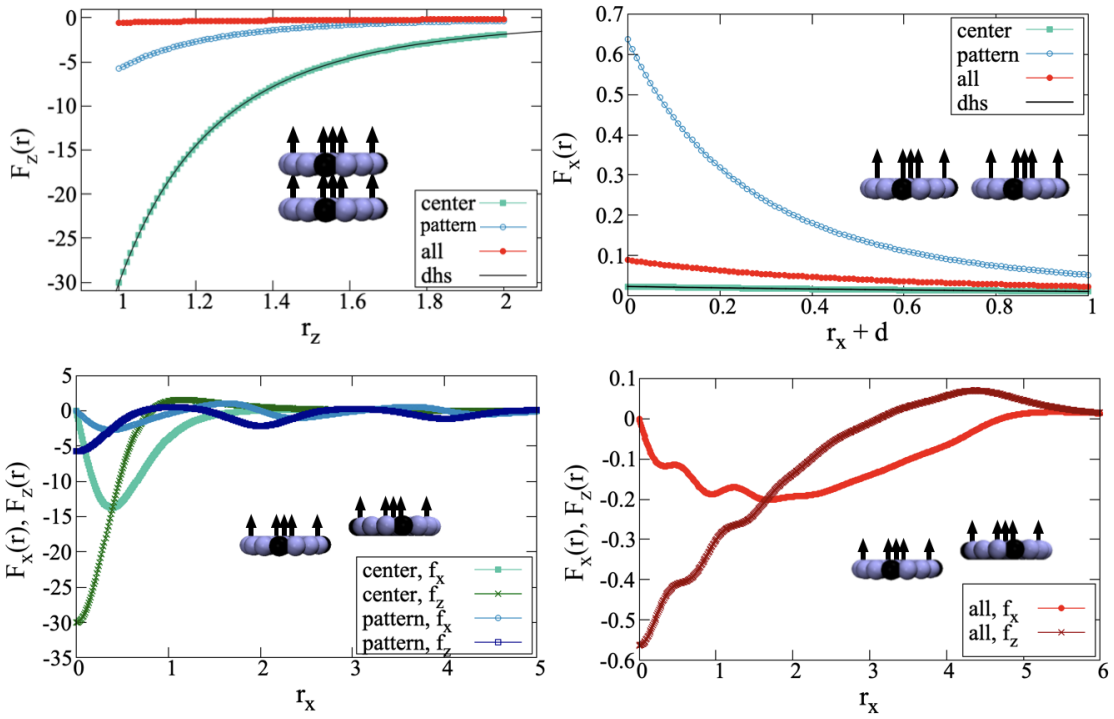

Figure 7.7: The force between two platelets, approaching each-other at different mutual orientations as indicated by the icons, where different colors indicate the different models used. Top row: two platelets with a single central (green), five distributed in a pattern (blue) or distributed on every bead (red) dipoles and a dipolar sphere (black) for reference. The left shows the face-to-face attraction, while the right shows the side-to-side repulsion. The bottom row shows the different forces on an approach from the side, with a shift in height of one platelet diameter- this means that is samples the orientations that should be close to the maximum of attraction. We see that the different models yield dramatically different attraction strengths at close range, but overall the more distributed the dipoles are, the weaker the attraction becomes.

the most suitable form of the potential. There is one promising conclusion regardless of model choice: both for central and distributed dipoles, the effective attraction and/or self-assembly are weaker than would be expected for spheres. This explains the additional stability they seem to find in experiment, despite their high magnetic moments. However, for a full picture of stability, it would be remiss not to acknowledge the electrostatic repulsion at play in the system.

7.3 Electrostatics

Without a question, the charge stabilization as mediated by DSBA surfectant is key to colloidal stability in experiment. More than that, it is a long range interaction that mediates the effective shape of the particles. From both literature (see Section 2.1.3.a) and recent experimental confirmations[134], we know that the electrostatics of the suspensions are a strong influence on the isotropic to nematic transition for these particular mesogens. In simulations of spherical particles, using an effective (larger) shape of the particle to account for this repulsion is arguably the standard approach. But in the case of very anisotropic mesogens, this means that we could be neglecting some of the anisotropy of the interparticle interactions. Theoretical and simulation studies have shown[62,68] that these interactions can be strongly isotropic over long ranges, which can significantly change the phase behavior.

In Figure 7.8, the left plot shows a simple "toy" model illustrating the balance between charge and magnetic potential. Since magnetics have already been discussed in detail, we assume alignment of the dipoles along the z-axis with $r = r_z$ as before and set $\lambda = \mu = 1$. Specifically the combination of the dipole-dipole and electrostatic Debye-Hueckel (see Section 2.2.2) for two particles with a central point dipole and central charge approaching along the line of the dipole minimum:

$$U_t(r) = \frac{-2}{r^3} + l_B q^2 \exp(-\kappa r) \tag{7.7}$$

Inspired by Chapter 3 and the reduced units therein, we set $l_B \approx 0.5$ and $\kappa = 7/26$. If we deliberately reduce the electrostatic repulsion (which would be 27) to be comparable to the magnetic moment, we get the composite curves shown in Figure 7.8. The energy barrier is smooth.

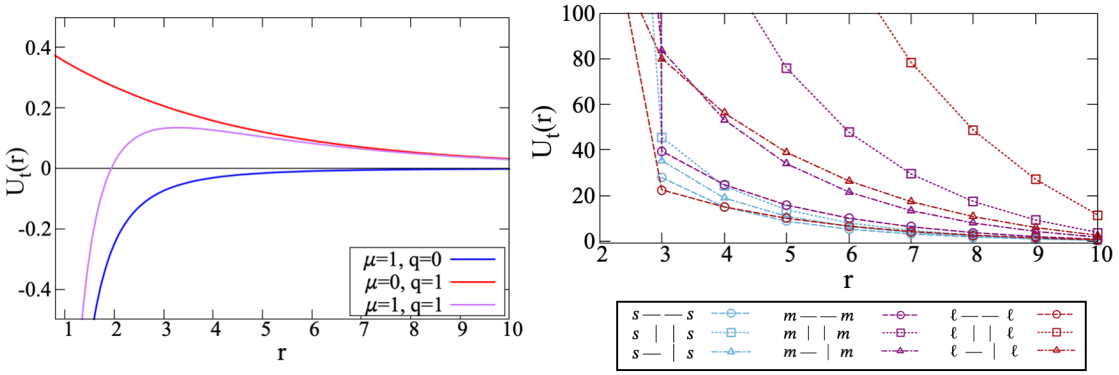

Figure 7.8: Left: Toy model of the balance between electrostatic repulsion and dipolar attraction, illustrating the superposition of these potentials in the optimal configuration for self-assembly. Right: measuring the potential for varying mutual orientations of small, medium and large platelets, we see pronounced differences in magnitude for medium and large platelets.

On the right side of Figure 7.8, we see a plot where simulations were used to calculate the potential via integration of the forces on small (aspect ratio 1:2), median (aspect ratio 1:6) and large (aspect ratio 1:16) charged discs with all parameters set as in Chapter 3. We see that this creates purely repulsive potentials, while explains the colloidal stability in those particular parameter ranges. We also see varying shape effects with the platelet size: for small platelets, all three are similar. For median and large platelets, the repulsion in the vertical to vertical is the lowest, the T configurations are equivalent and the face-to-face are extremely repulsive. Moreover, while the theoretical steric minimum is at one, many of these values already begin to diverge at by the Debye length of $1/l_b = 2$. This indicates that the polydispersity carries through to the longer range charge repulsion. The polydispersity might therefore be aiding the ordering in more than just the magnetic ways.

In order to properly understand our electrostatic situation, we turned to both analytical calculations and field measurements in simulation. However, the results proved less interesting than expected. For the simplest analytical problem, going along the axis, the solution is a trivial exercise that can be found in textbooks[194]. Other angles can be solved numerically, but are unstable near the platelet surface. Simulation models did show a difference for different charge distributions at short range, but once the proper counter-ions were added, any differences between the charge distributions were restricted to very close range, at which point in the physical system any interaction would be absolutely dominated by the magnetic dipole interactions. This means that, barring any new experimental evidence suggesting a wildly different, or wildly differently distributed charge, the actual electrostatic effects serve predominantly to ensure colloidal stability, and to induce some changes in effective shape at the short range.

8 - Conclusion

A combination of older theoretical conjectures and recent experimental breakthroughs have made a new variant of anisotropic, anisometric Magnetic Soft Matter available. Much as their predecessors of varying shapes, colloidal magnetic platelets hold investigative interest because of their potential to exhibit new magnetic properties that combine the advantages of magnetic fluids and liquid crystals. This work has explored the realities of this conjecture from a magnetic fluids perspective. Magnetic platelets, in particular, have yielded multiple surprises in experiment, from their ferromagnetic nematic phase transition to their atypical dynamic magnetic susceptibility. Part of this surprise is due to the limits of classical dipolar hard sphere theory in predicting these responses. The studies presented in this thesis tried to serve a twofold purpose: both to link to experiments, explaining the mechanisms behind their outcomes, and to go beyond the current state of synthesis to provide a theoretical foundation linking platelet shape and microstructural properties, in order to guide future synthesis.

At the outset, we sought to calibrate the simulation model to experiment. After validating the model against the microstructure of the isotropic phase, we induced a nematic phase transition by applying an external magnetic field. This illustrated the role of polydispersity, especially the role of larger magnetic platelets, in the magnetic and ordering properties of the system. However, this direct model found surprisingly low magnetic correlations between platelets, indicating that a more direct translation of the experimental properties into standard simulation models does not fully capture the intricacy of the magnetic properties observed in experiment.

This led to the next step, the pursuit of clarity on the shape and magnetic properties. Building on our understanding of the microstructure and magnetic property links in dipolar hard spheres, we sought to understand and characterize the microstructure of magnetic platelets. Beginning at intermediate concentrations and magnetic moments, we found a strong quantitative and qualitative divergence in the microstructure. A key observable for this was the self-assembly, which, due to the particle shape anisotropy, exhibits a limited set of motifs. However, these limited motifs, specifically chains, are associated with strong magnetic field responses. Below the threshold of self-assembly, the static magnetic susceptibility is well-described by dipolar sphere theories, given a certain density rescaling. However, as soon as the criteria for self-assembly are met, new theory is necessary to describe the sharply rising field response. We introduce several variations for this new theory, presenting results that also apply well to highly magnetic platelets, which links to the highly magnetic platelets studied in experiment.

One such interesting experimental outcome were the measurements of the dynamic magnetic susceptibility. Our simulations sampled the microstructural phase coexistence regions to posit an explanation for the broadening of the susceptibility peak, showing that the difference in microstructure explains two orders of magnitude of this gap, with the remaining order of magnitude attributed to the polydispersity. We also sample the response to a bias field, and observe that it

strongly favors self-assembly, which further broadens the dynamic response.

Another feature of experimental systems is that they often involve mixtures of different particle types. We investigate the influence of anisotropic depletants, as well as the effects of binary mixtures of particles with different magnetic moments on the microstructure, showing that platelets with specific choices of magnetic moments will not demix. The depletant effects do not lead to additional ordering, which lets us consider them for volume rescaling approaches. The presence of less magnetic particles also does not hinder the self-assembly, even though the less magnetic particles form fewer bonds than their more strongly interacting counterparts. These magnetic responses present a marked difference to ellipsoids, for which the self-assembly reduced the magnetic response.

In addition to these directly applicable results, this work was also focused on laying groundwork for future studies and exploring more potential contributing factors to interesting effects. We investigated options to model the combined magnetic and liquid crystalline domain structure in simulation, propose a distributed dipole model that could more accurately represent multipolar platelet interactions, and check to ensure that the electrostatics of the magnetic nanoplatelets are not affecting the ordering.

Taken as a whole, this work combines with experimental and theoretical literature to provide the foundation for our understanding of colloidal magnetic platelets. Through the lens of connecting microstructure to magnetic response, we focused on a few key properties such as the self-assembly, and explored both their attributes and influence on the system. However, this is just a selection of interesting aspects of this system which can be explored. Some tantalizing experimental results indicate that, due to the combination of field coupling and shape, magnetic fields could induce local flows in a ferromagnetic nematic system. This would be an ideal use case for more studies including hydrodynamics, which the model presented in this thesis would be well-suited to generalize to. Another natural extension is the consideration of more nuanced magnetic interaction models, for instance via the distributed dipole model presented in Chapter 7, or via complementary micromagnetics simulations to obtain a more detailed potential. Some studies on the former option have already been started. Finally, returning to the ferromagnetic nematic phase which sparked interest in this system, there are still a few open questions regarding the domain structure, especially under confinement, which would be a fascinating extension of liquid-crystalline theory. As illustrated by these examples, my hope is that this work will come to be viewed as merely the starting point for a vibrant field of colloidal magnetic platelet fluids.

Bibliography

[1] SÉBASTIEN BALIBAR ÉDOUARD BRÉZIN. “La matière molle” in: *Demain, la physique*. Odile Jacob, 2009. chap. 7

[2] P.-G. DE GENNES. *Soft Matter*, **1**, 16–, (2005).

[3] RICHARD A. L. JONES. *Soft Condensed Matter*. 2006.

[4] I CHUANG, R DURRER, N TUROK, and B YURKE. *Science*, **251**, 1336–1342, (1991).

[5] RAFFAELE MEZZENGA. *Frontiers in Soft Matter*, **1**, (2021).

[6] ANTHONY A. HYMAN, CHRISTOPH A. WEBER, and FRANK JÜLICHER. *Annual Review of Cell and Developmental Biology*, **30**, 39–58, (2014).

[7] BIN WANG, LEI ZHANG, TONG DAI, ZIRAN QIN, HUASONG LU, LONG ZHANG, and FANGFANG ZHOU. *Signal Transduction and Targeted Therapy*, **6**, 290, (2021).

[8] JASPER VAN DER GUCHT. *Frontiers in Physics*, **6**, (2018).

[9] LINDA S. HIRST. *Fundamentals of Soft Matter Science*. Second edition Taylor and Francis, 2020.

[10] RAFFAELE MEZZENGA, PETER SCHURTENBERGER, ADAM BURBIDGE, and MARTIN MICHEL. *Nature Materials*, **4**, 729–740, (2005).

[11] R. G. M. VAN DER SMAN and A. J. VAN DER GOOT. *Soft Matter*, **5**, 501–510, (2009).

[12] THOMAS A VILGIS. *Reports on Progress in Physics*, **78**, 124602, (2015).

[13] JACOB N. ISRAELACHVILI, ed. *Intermolecular and Surface Forces (Third Edition)*. San Diego: Academic Press, 2011.

[14] FRANCESCO SCIORTINO. *Rivista del nuovo cimento*, **42**, (2019).

[15] NICOLAS VOGEL, MARKUS RETSCH, CHARLES-ANDRÉ FUSTIN, ARANZAZU DEL CAMPO, and ULRICH JONAS. *Chemical Reviews*, **115** PMID: 26098223, 6265–6311, (2015).

[16] ANDONG WANG, JIANBIN HUANG, and YUN YAN. *Soft Matter*, **10**, 3362–3373, (2014).

[17] P.G. DEGENNES and J. PROST. *The Physics of Liquid Crystals*. Second Edition Oxford University Press, 1993.

[18] ISABELLA DE BELLIS, BIN NI, DANIELE MARTELLA, CAMILLA PARMEGGIANI, PATRICK KELLER, DIEDERIK S. WIERSMA, MIN-HUI LI, and SARA NOCENTINI. *Advanced Intelligent Systems*, **2**, 2000035, (2020).

[19] VIVEK SHARMA, MATIJA CRNE, JUNG OK PARK, and MOHAN SRINIVASARAO. *Science*, **325**, 449–451, (2009).

[20] GLENN H. BROWN and JEROME J. WOLKEN. *Liquid Crystals and Biological Structures*. Academic Press, Inc., 1979.

[21] JEROEN BEECKMAN, KRISTIAAN NEYTS, and PIETER J. M. VANBRABANT. *Optical Engineering*, **50**, 081202, (2011).

[22] SCOTT J. WOLTMAN, GREGORY D. JAY, and GREGORY P. CRAWFORD. *Nature Materials*, **6**, 929–938, (2007).

[23] IVAN I. SMALYUKH. *Annual Review of Condensed Matter Physics*, **9**, 207–226, (2018).

[24] R. E. ROSENSWEIG. *Ferrohydrodynamics*. Cambridge University Press, 1985.

[25] PAPELL STEPHEN "Low viscosity magnetic fluid obtained by the colloidal suspension of magnetic particles" US315096A 1963

[26] STEFAN. ODENBACH. *Ferrofluids : Magnetically Controllable Fluids and Their Applications*. Springer, 2011.

[27] LAURA ROSSI, STEFANO SACANNA, WILLIAM T. M. IRVINE, PAUL M. CHAIKIN, DAVID J. PINE, and ALBERT P. PHILIPSE. *Soft Matter*, **7**, 4139–4142, (2011).

[28] HOJIN KIM and ERIC M. FURST. *Journal of Colloid and Interface Science*, **566**, 419–426, (2020).

[29] STEFANO SACANNA, MARK KORPICS, KELVIN RODRIGUEZ, LAURA COLÓN-MELÉNDEZ, SEUNG-HYUN KIM, DAVID J. PINE, and GI-RA YI. *Nature Communications*, **4**, 1688, (2013).

[30] ZHENLI ZHANG and SHARON C. GLOTZER. *Nano Letters*, **4** PMID: 29048902, 1407–1413, (2004).

[31] A CEBERS. *Magnitnaya Gidrodinamika (in Russ.)*, **18**, 42, (1982).

[32] KAZUHIRO SANO and MASAO DOI. *J. Phys. Soc. Japan*, **52**, 2810–2815, (1983).

[33] DONGQING WEI and GN PATEY. *Phys. Rev. Lett.*, **68**, 2043, (1992).

[34] J. J. WEIS and D. LEVESQUE. *Phys. Rev. Lett.*, **71**, 2729–2732, (1993).

[35] J. J. WEIS and D. LEVESQUE. *Phys. Rev. E*, **48**, 3728–3740, (1993).

[36] B GROH and S DIETRICH. *Phys. Rev. Lett.*, **72**, 2422, (1994).

[37] B GROH and S DIETRICH. *Phys. Rev. E*, **50**, 3814, (1994).

[38] G AYTON, MJP GINGRAS, and GN PATEY. *Phys. Rev. Lett.*, **75**, 2360, (1995).

[39] B GROH and S DIETRICH. *Phys. Rev. E*, **53**, 2509, (1996).

[40] B GROH and S DIETRICH. *Phys. Rev. E*, **57**, 4535, (1998).

[41] SABINE KLAPP and FRANK FORSTMANN. *Phys. Rev. E*, **60**, 3183, (1999).

[42] H. MAMIYA, I. NAKATANI, and T. FURUBAYASHI. *Phys. Rev. Lett.*, **84**, 6106–6109, (2000).

[43] GT GAO and XIAO CHENG ZENG. *Phys. Rev. E*, **61**, R2188, (2000).

[44] ALEXEY O. IVANOV. *Phys. Rev. E*, **68**, 011503, (2003).

[45] P.-G. DE GENNES. F. BROCHARD. *Journal de Physique*, **31**, 691–708, (1970).

[46] M SHUAI, A KLITTNICK, Y SHEN, G P SMITH, M R TUCHBAND, C ZHU, R G PETSCHEK, A MERTELJ, D LISJAK, M ČOPIČ, J E MACLENNAN, M A GLASER, and N A CLARK. *Nature Communications*, **7**, 10394, (2016).

[47] JEAN-PIERRE HANSEN and IAN R. MCDONALD. *Theory of Simple Liquids (Fourth Edition)*. Fourth Edition Oxford: Academic Press, 2013. 13–59

[48] B. SMIT D. FRENKEL. *Understanding molecular simulation : from algorithms to applications*. 2nd San Diego: Academic Press, 2002.

[49] MICHAEL P. ALLEN and DOMINIC J. TILDESLEY. *Computer Simulation of Liquids*. Oxford University Press, June 2017.

[50] ROBERT PECORA REDOUANE BORSALI, ed. *Soft-Matter Characterization*. 2008.

[51] VALENTIN S. MENDELEV and ALEXEY O. IVANOV. *Phys. Rev. E*, **70**, 051502, (2004).

[52] R. E. ROSENSWEIG. *J. Mag. Magn. Mater.*, **252**, 370–374, (2002).

[53] C M CARE and D J CLEAVER. *Reports on Progress in Physics*, **68**, 2665, (2005).

[54] J. A. C. VEERMAN and D. FRENKEL. *Phys. Rev. A*, **45**, 5632–5648, (1992).

[55] D. FRENKEL and B. M. MULDER. *Mol. Phys.*, **55**, 1171, (1985).

[56] PATRICK DAVIDSON, CHRISTOPHE PENISSON, DORU CONSTANTIN, and JEAN-CHRISTOPHE P. GABRIEL. *PNAS*, 201802692, (2018).

[57] D. VAN DER BEEK, A. V. PETUKHOV, P. DAVIDSON, J. FERRÉ, J. P. JAMET, H. H. WENSINK, G. J. VROEGE, W. BRAS, and H. N.W. LEKKERKERKER. *Phys. Rev. E*, **73**, 041402, (2006).

[58] FELIX M. VAN DER KOOIJ and HENK N. W. LEKKERKERKER. *The Journal of Physical Chemistry B*, **102**, 7829–7832, (1998).

[59] H. TANAKA, J. MEUNIER, and D. BONN. *Phys. Rev. E*, **69**, 31404, (2004).

[60] DAVID VAN DER BEEK and HENK N. W. LEKKERKERKER. *Langmuir*, **20** PMID: 15379478, 8582–8586, (2004).

[61] HENK N. W. LEKKERKERKER, FELIX M. VAN DER KOOIJ, and KATERINA KASSAPIDOU. *Nature*, **406**, 868–871, (2000).

[62] SARA JABBARI-FAROUJI, JEAN-JACQUES WEIS, PATRICK DAVIDSON, PIERRE LEVITZ, and EMMANUEL TRIZAC. *Scientific Reports*, **3**, 3559, (2013).

[63] F. M. VAN DER KOOIJ, K. KASSAPIDOU, and H. N. W. LEKKERKERKER. *Nature*, **406**, 868–871, (2000).

[64] ALENKA MERTELJ and DARJA LISJAK. *Liquid Crystals Reviews*, **5**, 1–33, (2017).

[65] SIMONA OVTAR, DARJA LISJAK, and MIHA DROFENIK. *Journal of Colloid and Interface Science*, **337**, 456–463, (2009).

[66] DARJA LISJAK and MIHA DROFENIK. *Crystal Growth & Design*, **12**, 5174–5179, (2012).

[67] LARS ONSAGER. *Annals of the New York Academy of Sciences*, **51**, 627–659, (1949).

[68] R. AGRA, E. TRIZAC, and L. BOCQUET. *The European Physical Journal E*, **15**, 345–357, (2004).

[69] K. RAJ and R. MOSKOWITZ. *IEEE Transactions on Magnetics*, **16**, 358–363, (1980).

[70] YANWEN LI, PENGDONG HAN, DECAI LI, SIYU CHEN, and YUMING WANG. *Friction*, **11**, 165–186, (2023).

[71] ZHENGHAO LI and DECAI LI. *Frontiers in Materials*, **9**, (2022).

[72] RAQUEL G. D. ANDRADE, SÉRGIO R. S. VELOSO, and ELISABETE M. S. CASTANHEIRA. *International Journal of Molecular Sciences*, **21**, (2020).

[73] M. A. KHAIRUL, ELHAM DOROODCHI, REZA AZIZIAN, and BEHDAD MOGHTADERI. *Energy Convers. Manag.*, **149**, 660–674, (2017).

[74] MYEONG-LOK SEOL, SEUNG-BAE JEON, JIN-WOO HAN, and YANG-KYU CHOI. *Nano Energy*, **31**, 233–238, (2017).

[75] HYE RIM YUN, DOO JIN LEE, JAE RYOUN YOUN, and YOUNG SEOK SONG. *Nano Energy*, **11**, 171–178, (2015).

[76] A. BIBO, R. MASANA, A. KING, G. LI, and M.F. DAQAQ. *Phys. Lett. A*, **376**, 2163–2166, (2012).

[77] DIANYU WANG, SHUANG ZHENG, HE LIU, JIAYUE TANG, WEINING MIAO, HUANTING WANG, YE TIAN, HUA YANG, and LEI JIANG. *Adv. Mater.*, **31**, 1805953, (2019).

[78] RUEY-JEN YANG, HUI-HSIUNG HOU, YAO-NAN WANG, and LUNG-MING FU. *Sens. Actuators B Chem.*, **224**, 1–15, (2016).

[79] ARTEM A. ELISEEV, ANDREI A. ELISEEV, LEV A. TRUSOV, ANDREI P. CHUMAKOV, PETER BOESECKE, EVGENY O. ANOKHIN, ALEXANDER V. VASILIEV, ANASTASIA E. SLEPTSOVA, EVGENY A. GORBACHEV, VLADIMIR V. KOROLEV, and PAVEL E. KAZIN. *Appl. Phys. Lett.*, **113**, 113106, (2018).

[80] XIAOXUAN ZHANG, LINGYU SUN, YUNRU YU, and YUANJIN ZHAO. *Adv. Mater.*, **31**, 1903497, (2019).

[81] KAREL ULBRICH, KATEŘINA HOLÁ, VLADIMIR ŠUBR, ARISTIDES BAKANDRITSOS, JIŘÍ TUČEK, and RADEK ZBOŘIL. *Chem. Rev.*, **116**, 5338–5431, (2016).

[82] PETER MEDLE RUPNIK, DARJA LISJAK, MARTIN ČOPIČ, and ALENKA MERTELJ. *Liq. Cryst.*, **42**, 1684–1688, (2015).

[83] P. LANGEVIN. *J. de Phys.*, **4**, 678, (1905).

[84] P. LANGEVIN. *Ann. Chim. et Phys.*, **5**, 70, (1905).

[85] A. IVANOV, S. KANTOROVICH, E. REZNIKOV, C. HOLM, A. PSHENICHNIKOV, A., A. CHREMOS, and P. CAMP. *Phys. Rev. E*, **75**, 061405, (2007).

[86] ALEXEY O. IVANOV and OLGA B. KUZNETSOVA. *Phys. Rev. E*, **64**, 041405, (2001).

[87] PIERRE WEISS. *J. Phys. Theor. Appl.*, **6**, (1907).

[88] JOE G. DONALDSON, ELENA S. PYANZINA, and SOFIA S. KANTOROVICH. *ACS Nano*, **11** PMID: 28763187, 8153–8166, (2017).

[89] C.G. JOSLIN. *Mol. Phys.*, **47**, 771–783, (1982).

[90] M. BAUS and J.-L. COLOT. *Phys. Rev. A*, **40**, 5444–5446, (1989).

[91] A. PERERA and G. N. PATEY. *J. Chem. Phys.*, **91**, 3045–3055, (1989).

[92] J. M. CAILLOL and J. J. WEIS. *J. Chem. Phys.*, **92**, 3197–3205, (1990).

[93] G.J. ZARRAGOICOECHEA, D. LEVESQUE, and J.J. WEIS. *Mol. Phys.*, **75**, 989–998, (1992).

[94] C. VEGA and S. LAGO. *J. Chem. Phys.*, **100**, 6727–6737, (1994).

[95] K. SATOH, S. MITA, and S. KONDO. *Chem. Phys. Lett.*, **255**, 99–104, (1996).

[96] K. SATOH, S. MITA, and S. KONDO. *Liq. Cryst.*, **20**, 757–763, (1996).

[97] K. SATOH, S. MITA, and S. KONDO. *Mol. Cryst. Liq. Cryst. Sci. Tech. Mol. Cryst. Liq. Cryst.*, **300**, 143–161, (1997).

[98] B. GROH and S. DIETRICH. *Phys. Rev. E*, **55**, 2892–2901, (1997).

[99] G. AYTON, D. Q. WEI, and G. N. PATEY. *Phys. Rev. E*, **55**, 447–454, (1997).

[100] SIMON C. MCGROTHER, ALEHANDRO GIL-VILLEGAS, and GEORGE JACKSON. *Mol. Phys.*, **95**, 657–673, (1998).

[101] J. C. SHELLEY, G. N. PATEY, D. LEVESQUE, and J. J. WEIS. *Phys. Rev. E*, **59**, 3065–3070, (1999).

[102] G. RICKAYZEN. *Mol. Phys.*, **98**, 683–692, (2000).

[103] SZABOLCS VARGA, ISTVAN SZALAI, JANOS LISZI, and GEORGE JACKSON. *J. Chem. Phys.*, **116**, 9107–9119, (2002).

[104] ALEXANDR MALIJEVSKY, GEORGE JACKSON, and SZABOLCS VARGA. *J. Chem. Phys.*, **129**, 144504, 144504, (2008).

[105] J.H. SÁNCHEZ and C. RINALDI. *J. Colloid Interface Sci.*, **331**, 500–506, (2009).

[106] S. C. MCGROTHER and G. JACKSON. *Phys. Rev. Lett.*, **76**, 4183–4186, (1996).

[107] D. LEVESQUE, J. J. WEIS, and G. J. ZARRAGOICOECHEA. *Phys. Rev. E*, **47**, 496–505, (1993).

[108] E. GWOZDZ, A. BRODKA, and K. PASTERNY. *Chem. Phys. Lett.*, **267**, 557–562, (1997).

[109] A. GIL-VILLEGAS, S. C MCGROTHER, and G. JACKSON. *Chem. Phys. Lett.*, **269**, 441–447, (1997).

[110] R. BERARDI, S. ORLANDI, and C. ZANNONI. *Int. J. Mod. Phys. C*, **10**, 477–484, (1999).

[111] R. BERARDI, S. ORLANDI, and C. ZANNONI. *Phys. Chem. Chem. Phys.*, **2**, 2933–2942, (2000).

[112] T. K. BOSE and J. SAHA. *Phys. Rev. E*, **86**, 050701, (2012).

[113] S. C MCGROTHER, A. GIL-VILLEGAS, and G. JACKSON. *J. Phys.: Cond. Matter*, **8**, 9649, (1996).

[114] S. SACANNA, L. ROSSI, B. W. M. KUIPERS, and A. P. PHILIPSE. *Langmuir*, **22**, 1822–1827, (2006).

[115] MASATO NAKADE, TETSURO IKEDA, and MAKOTO OGAWA. *Journal of Materials Science*, **42**, 4815–4823, (2007).

[116] JOHN PAPIOANNOU. *Simulation Studies of Ferromagnetic Nematic Fluids*. Doctoral Thesis. University of Colorado, 2919.

[117] D. A. PETROV. *Bulletin of the Russian Academy of Sciences: Physics*, **86**, 115–119, (2022).

[118] PAUL LANGEVIN. *C. R. Acad. Sci. (Paris)*, (1908).

[119] J. D. WEEKS, D. CHANDLER, and H. C. ANDERSEN. *J. Chem. Phys.*, **54**, 5237, (1971).

[120] HELMUT VOGEL. *Mathematical Biosciences*, **44**, 179–189, (1979).

[121] FLORIAN WEIK, RUDOLF WEEBER, KAI SZUTTOR, KONRAD BREITSPRECHER, JOOST DE GRAAF, MICHAEL KURON, JONAS LANDSGESELL, HENRI MENKE, DAVID SEAN, and CHRISTIAN HOLM. *The European Physical Journal Special Topics*, **227**, 1789–1816, (2019).

[122] MATTHIEU MARECHAL, ALEJANDRO CUETOS, BRUNO MARTÍNEZ-HAYA, and MARJOLEIN DIJKSTRA. *The Journal of Chemical Physics*, **134**, 094501, (2011).

[123] J. G. GAY and B. J. BERNE. *The Journal of Chemical Physics*, **74**, 3316–3319, (1981).

[124] JUAN J. CERDÀ, V. BALLENEGGER, O. LENZ, and C. HOLM. *The Journal of Chemical Physics*, **129**, 234104, (2008).

[125] B HUKE and M LÜCKE. *Rep. Prog. Phys.*, **67**, 1731–1768, (2004).

[126] ALEX. HUBERT and RUDOLF. SCHÄFER. *Magnetic Domains The Analysis of Magnetic Microstructures*. Springer Berlin, 2014.

[127] MICHAEL KOTLARCHYK and SOW-HSIN CHEN. *The Journal of Chemical Physics*, **79**, 2461–2469, (1983).

[128] M.V. AVDEEV, V.L. AKSENOV, M. BALASOIU, V.M. GARAMUS, A. SCHREYER, GY. TŐRŐK, L. ROSTA, D. BICA, and L. VÉKÁS. *Journal of Colloid and Interface Science*, **295**, 100–107, (2006).

[129] MIKHAIL V. AVDEEV. *Journal of Molecular Liquids*, **189** Fluid phase associations, 68–73, (2014).

[130] PAUL J. STEINHARDT, DAVID R. NELSON, and MARCO RONCHETTI. *Phys. Rev. B*, **28**, 784–805, (1983).

[131] PATRICIJA HRIBAR BOŠTJANČIČ, MATIJA TOMŠIČ, ANDREJ JAMNIK, DARJA LISJAK, and ALENKA MERTELJ. *J. Phys. Chem. C*, **123**, 23272–23279, (2019).

[132] W. B. RUSSEL, D. A. SAVILLE, and W. R. SCHOWALTE. *Colloidal Dispersions*. Cambridge: Cambridge University Press, 1991.

[133] R. BERARDI, S. ORLANDI, and C. ZANNONI. *J. Chem. Soc. Faraday Trans.*, **93**, 1493–1496, (1997).

[134] PATRICIJA HRIBAR BOŠTJANČIČ, ŽIGA GREGORIN, NEREA SEBASTIÁN, NATAN OSTERMAN, DARJA LISJAK, and ALENKA MERTELJ. *Journal of Molecular Liquids*, **348**, 118038, (2022).

[135] ELENA S. PYANZINA, SOFIA S. KANTOROVICH, and CRISTIANO DE MICHELE. *The European Physical Journal E*, **38**, 81, (2015).

[136] ELENA S. MININA, ELENA S. PYANZINA, EKATERINA V. NOVAK, and SOFIA S. KANTOROVICH. *The European Physical Journal E*, **41**, 67, (2018).

[137] A.O. IVANOV, S.S. KANTOROVICH, L. ROVIGATTI, J.M. TAVARES, and F. SCIORTINO. *Journal of Magnetism and Magnetic Materials*, **383** Selected papers from the sixth Moscow International Symposium on Magnetism (MISM-2014), 272–276, (2015).

[138] J. RUSSO, J. M. TAVARES, P. I. C. TEIXEIRA, M. M. TELO DA GAMA, and F. SCIORTINO. *Phys. Rev. Lett.*, **106**, 085703, (2011).

[139] LORENZO ROVIGATTI, JOSÉ MARIA TAVARES, and FRANCESCO SCIORTINO. *Phys. Rev. Lett.*, **111**, 168302, (2013).

[140] LORENZO ROVIGATTI, SOFIA KANTOROVICH, ALEXEY O. IVANOV, JOSÉ MARIA TAVARES, and FRANCESCO SCIORTINO. *The Journal of Chemical Physics*, **139**, 134901, (2013).

[141] J. A. C. VEERMAN and D. FRENKEL. *Phys. Rev. A*, **45**, 5632–5648, (1992).

[142] WOLFGANG LECHNER and CHRISTOPH DELLAGO. *The Journal of Chemical Physics*, **129**, 114707, (2008).

[143] KIRSTIN R. PURDY, ZVONIMIR DOGIC, SETH FRADEN, ADRIAN RÜHM, LAWRENCE LURIO, and SIMON G. J. MOCHRIE. *Phys. Rev. E*, **67**, 031708, (2003).

[144] J.J. BINNEY, DOWRICK N. J., A.J. FISCHER, and M.E.J. NEWMAN. *The Theory of Critical Phenomena*. Oxford University Press, 2002.

[145] MICHAEL S. RUSANOV, VLADIMIR S. ZVEREV, and EKATERINA A. ELFIMOVA. *Phys. Rev. E*, **104**, 044604, (2021).

[146] H. NÁDASI, M. KÜSTER, A. MERTELJ, N. SEBASTIÁN, P. H. BOŠTJANČIČ, D. LISJAK, T. VIERECK, M. ROSENBERG, A. O. IVANOV, S. S. KANTOROVICH, A. EREMIN, and F. LUDWIG. *J. Mol. Liq.*, **382**, 121900, (2023).

[147] PETER C. JORDAN. *Molecular Physics*, **25**, 961–973, (1973).

[148] JESSICA F LIU, BIAN JANG, DAVID ISSADORE, and ANDREW TSOURKAS. *Wiley Interdiscip. Rev. Nanomed. Nanobiotechnol.*, **11**, 1571, (2019).

[149] GUADALUPE GABRIEL FLORES-ROJAS, FELIPE LÓPEZ-SAUCEDO, RICARDO VERA-GRAZIANO, EDUARDO MENDIZABAL, and EMILIO BUCIO. *Macromol*, **2**, 374–390, (2022).

[150] OSCAR CERVANTES, ZAIRA DEL ROCIO LOPEZ, NORBERTO CASILLAS, PETER KNAUTH, NAYELI CHECA, FRANCISCO APOLINAR CHOLICO, RODOLFO HERNANDEZ-GUTIÉRREZ, LUIS HECTOR QUINTERO, JOSE AVILA PAZ, and MARIO EDUARDO CANO. *Molecules*, **27**, 544, (2022).

[151] DIANYU WANG, SHUANG ZHENG, HE LIU, JIAYUE TANG, WEINING MIAO, HUANTING WANG, YE TIAN, HUA YANG, and LEI JIANG. *Adv. Mater.*, **31**, 1805953, (2019).

[152] M. KÜSTER, F. LUDWIG, A. EREMIN, P. H. BOŠTJANČIČ, D. LISJAK, N. SEBASTIÁN, A. MERTELJ, and H. NÁDASI. *J. Mol. Liq.*, **360**, 119484, (2022).

[153] A. O. IVANOV and P. J. CAMP. *Phys. Rev. E*, **98**, 050602(R), (2018).

[154] J. O. SINDT, P. J. CAMP, S. S. KANTOROVICH, E. A. ELFIMOVA, and A. O. IVANOV. *Phys. Rev. E*, **93**, 063117, (2016).

[155] P. J. CAMP, A. O. IVANOV, and J. O. SINDT. *Phys. Rev. E*, **103**, 062611, (2021).

[156] T. M. BATRUDINOV, YU. E. NEKHOROSHKOVA, E. I. PARAMONOV, V. S. ZVEREV, E. A. ELFIMOVA, A. O. IVANOV, and P. J. CAMP. *Phys. Rev. E*, **98**, 052602, (2018).

[157] M. ROSENBERG and S. S. KANTOROVICH. *Phys. Chem. Chem. Phys.*, **25**, 2781–2792, (2023).

[158] D. LEVESQUE and J. J. WEIS. *Phys. Rev. E*, **49**, 5131–5140, (1994).

[159] P. J. CAMP and G. N. PATEY. *Phys. Rev. E*, **62**, 5403–5408, (2000).

[160] D. J. CEBULA, S. W. CHARLES, and J. POPPLEWELL. *Colloid. Polym. Sci.*, **259**, 395–397, (1981).

[161] F. GAZEAU, E. DUBOIS, J.-C. BACRI, F. BOUÉ, A. CEBERS, and R. PERZYNSKI. *Phys. Rev. E*, **65**, 031403, (2002).

[162] G. MÉRIGUET, F. COUSIN, E. DUBOIS, F. BOUÉ, A. CEBERS, B. FARAGO, and R. PERZYNSKI. *J. Phys. Chem. B*, **110**, 4378–4386, (2006).

[163] A. WIEDENMANN, U. KEIDERLING, M. MEISSNER, D. WALLACHER, R. GÄHLER, R. P. MAY, S. PREÉVOST, M. KLOKKENBURG, B. H. ERNÉ, and J. KOHLBRECHER. *Phys. Rev. B*, **77**, 184417, (2008).

[164] J. B. HAYTER and R. PYNN. *Phys. Rev. Lett.*, **49**, 1103–1106, (1982).

[165] S. HESS, J. B. HAYTER, and R. PYNN. *Mol. Phys.*, **53**, 1527–1533, (1984).

[166] J. P. HUANG, Z. W. WANG, and C. HOLM. *Phys. Rev. E*, **71**, 061203, (2005).

[167] J. J. CERDÀ, E. ELFIMOVA, V. BALLENEGGER, E. KRUTIKOVA, A. IVANOV, and C. HOLM. *Phys. Rev. E*, **81**, 011501, (2010).

[168] E. A. ELFIMOVA, A. O. IVANOV, and P. J. CAMP. *J. Chem. Phys.*, **136**, 194502, (2012).

[169] A. O. IVANOV, V. S. ZVEREV, and S. S. KANTOROVICH. *Soft Matter*, **12**, 3507–3513, (2016).

[170] A. C. FOGARTY, A. C. JONES, and P. J. CAMP. *Phys. Chem. Chem. Phys.*, **13**, 3819–3830, (2011).

[171] A. O. IVANOV and V. S. ZVEREV. *Mathematics*, **9**, 2450, (2021).

[172] M. A. MARTSENYUK, YU. L. RAIKHER, and M. I. SHLIOMIS. *Sov. Phys. JETP*, **38**, 413–416, (1974).

[173] M. I. SHLIOMIS and YU. L. RAIKHER. *IEEE Trans. Magn.*, **16**, 237–250, (1980).

[174] CHARLES R. CANTOR and PAUL R. SCHIMMEL. *Biophysical Chemistry*. 1980.

[175] N. G. ALMARZA, E. LOMBA, C. MARTÍN, and A. GALLARDO. *The Journal of Chemical Physics*, **129**, 234504, (2008).

[176] WILLIAM R. SMITH, OSVALDO H. SCALISE, and THEODOR W. MELNYK. *Fluid Phase Equilibria*, **44**, 237–254, (1989).

[177] T.W. MELNYK and W.R. SMITH. *Chemical Physics Letters*, **28**, 213–216, (1974).

[178] ANTTI-PEKKA HYNNINEN and MARJOLEIN DIJKSTRA. *Phys. Rev. E*, **72**, 051402, (2005).

[179] M. J. BLAIR and G. N. PATEY. *Phys. Rev. E*, **57**, 5682–5686, (1998).

[180] GABRIEL M. RANGE and SABINE H. L. KLAPP. *Phys. Rev. E*, **69**, 041201, (2004).

[181] I. SZALAI and S. DIETRICH. *Molecular Physics*, **103**, 2873–2895, (2005).

[182] X. S. CHEN, M. KASCH, and F. FORSTMANN. *Phys. Rev. Lett.*, **67**, 2674–2677, (1991).

[183] ZUOWEI WANG and CHRISTIAN HOLM. *Phys. Rev. E*, **68**, 041401, (2003).

[184] AMIT GOYAL, CAROL K. HALL, and ORLIN D. VELEV. *The Journal of Chemical Physics*, **133**, 064511, (2010).

[185] AMIT GOYAL, CAROL K. HALL, and ORLIN D. VELEV. *Soft Matter*, **6**, 480–484, (2010).

[186] M. BIER, L. HARNAU, and S. DIETRICH. *Phys. Rev. E*, **69**, 021506, (2004).

[187] JONATHAN PHILLIPS and MATTHIAS SCHMIDT. *Phys. Rev. E*, **81**, 041401, (2010).

[188] JONATHAN PHILLIPS and MATTHIAS SCHMIDT. *Journal of Physics: Condensed Matter*, **23**, 194111, (2011).

[189] KATHRIN MAY, ALEXEY EREMIN, RALF STANNARIUS, BALÁZS SZABÓ, TAMÁS BÖRZSÖNYI, INGO APPEL, SILKE BEHRENS, and SUSANNE KLEIN. *Journal of Magnetism and Magnetic Materials*, **431**, 79–83, (2017).

[190] THOMAS THELEN, ADRIANA JARA, and ISAAC TORRES-DÍAZ. *Soft Matter*, **19**, 640–651, (2023).

[191] EDUARDO SANZ, CHANTAL VALERIANI, DAAN FRENKEL, and MARJOLEIN DIJKSTRA. *Phys. Rev. Lett.*, **99**, 055501, (2007).

[192] FRANZ AURENHAMMER. *ACM Comput. Surv.*, **23**, 345–405, (1991).

[193] SOFIA KANTOROVICH, ELENA PYANZINA, and FRANCESCO SCIORTINO. *Soft Matter*, **9**, 6594–6603, (2013).

[194] DAVID J. GRIFFITHS. *Introduction to Electrodynamics*. 2008.